CALPHAD: Computer Coupling of Phase Diagrams and Thermochemistry 34 (2010) 332–362

Contents lists available at ScienceDirect

CALPHAD: Computer Coupling of Phase Diagrams and Thermochemistry

journal homepage: www.elsevier.com/locate/calphad

Overview of the applications of thermodynamic databases to steelmaking processes

In-Ho Jung *

Department of Mining and Materials Engineering, McGill University, H.W. Wong Building, 3610 University Street, Montréal, Québec, H3A 2B2, Canada

ARTICLE INFO

Article history:
Received 1 February 2010
Received in revised form
25 June 2010
Accepted 27 June 2010
Available online 6 August 2010

Keywords:
Steelmaking
Thermodynamic databases
Thermochemical software
Slag/steel/inclusion/refractory/gas reactions

ABSTRACT

Computerized thermodynamic databases for solid and liquid steel, slags and solid oxide solutions, for large numbers of components, have been developed over the last three decades by critical evaluation/optimization of all available phase equilibrium and thermodynamic data. The databases contain model parameters specifically developed for molten slags, liquid and solid steel and solid oxide solutions. With user-friendly software, which accesses these databases, complex chemical reactions and phase equilibria occurring throughout the steelmaking process can be calculated over wide ranges of temperature, oxygen potential and pressure. In the present article, the thermodynamic models and databases for molten slag and liquid steel included in well-known thermochemical packages and their applications to complex steelmaking processes involving molten slag, steel, inclusions, refractories and gases are reviewed.

© 2010 Elsevier Ltd. All rights reserved.

1. Introduction

Steelmaking comprises consecutive high-temperature chemical processes to refine liquid steel and to attain a narrow chemical composition for specified steel grades. In particular, clean steels with a low level of gaseous impurities such as C, S, P, N, H and O and non-metallic inclusions can be produced by the elaborate control of the chemical reactions involving liquid steel, slags, inclusions, refractories and gases. However, the reactions are often difficult to understand due to their complexity. Usually, to understand the complex chemical phenomena and solve practical problems in pyrometallurgical processes, a large body of experimental data must be obtained at great expense. In order to reduce the time and expense required for the experiments, and to understand the chemical reactions more fully, thermodynamic calculations based on accurate thermodynamic databases have been used actively in recent years.

Thermodynamic modeling has been actively pursued together with the improvement of computational techniques and software. Based on a proper thermodynamic model for every phase of a given system, all available thermodynamic and phase equilibrium data for the system are critically evaluated simultaneously in order to obtain one self-consistent set of model equations for the Gibbs energies which best reproduce the data for all phases as functions of temperature and composition. This technique has come to be known as thermodynamic "optimization (modeling)". Where data are lacking for a multicomponent system, the models and optimized model parameters for low-order (binary and ternary) subsystems can be used to provide good estimates. In this way, the thermodynamic databases are developed. The databases are then used, along with Gibbs energy minimization software, to calculate the conditions for multicomponent equilibrium.

The selection of proper databases for a given system is a prerequisite for accurate thermodynamic calculations. The databases must be thermodynamically self-consistent; otherwise, very erroneous results can often occur. Computerized thermodynamic databases for solid and liquid steel, slag and solid oxide solutions, for large numbers of components, have been developed over the last three decades by critical evaluation/optimization of all available phase equilibrium and thermodynamic data. The well-known thermochemical software packages with large thermodynamic databases for steelmaking processes are CEQCSI [1], FactSage [2], MPE [3], MTDATA [4] and Thermo-Calc [5]. The user-friendly software makes it possible to perform versatile thermodynamic calculations within the accuracy of the experimental data even for regions of composition and temperature where no experimental data are available.

In the present review article, the thermodynamic models and databases for oxide and liquid steel in large thermochemical packages and their applications to complex steelmaking processes involving molten steel, slag, inclusions, refractories and gases will be reviewed.

* Tel.: +1 514 398 2608; fax: +1 514 398 4492.
E-mail address: in-ho.jung@mcgill.ca.

0364-5916/$ – see front matter © 2010 Elsevier Ltd. All rights reserved.
doi:10.1016/j.calphad.2010.06.003

2. Thermodynamic models

In recent years, large thermodynamic databases for multicomponent oxide and alloy systems have been developed by what has come to be known as the 'Calphad technique'. Thermodynamic and phase equilibrium data for binary and ternary subsystems are critically evaluated and thermodynamic models are chosen for each phase based on their crystal structure. The model parameters are optimized to reproduce all reliable experimental data within experimental error limits. The databases are accessed by the Gibbs energy minimization software to calculate thermodynamic properties, phase diagrams and chemical reactions for multicomponent systems. Apparently, a thermodynamic model that adequately describes the enthalpy, entropy and Gibbs energy of the solution as functions of temperature and composition is the most essential for the development of large thermodynamic database for multicomponent systems. To be useful for this purpose, a model must be sufficiently realistic to have a good predictive ability, but not be so complex as to be mathematically intractable. In the present study, thermodynamic models frequently encountered in steelmaking applications involving molten slag, solid oxide solutions and liquid Fe solution will be reviewed without delving into the mathematical details.

2.1. Molten slag (liquid oxide)

Molten silicate slags are ionic liquids with complex network structure. The silicate tetrahedra network can be gradually broken down with addition of metal oxides, MO (network modifier), as represented schematically by the reaction

$$(\dot{:}\text{Si–O–Si}\dot{:}) + \text{MO} = (\dot{:}\ \text{Si–O–}\ \text{M}^{2+}\text{–O–Si}\ \dot{:}). \quad (1)$$

This silicate network breaking reaction (depolymerization reaction) can be simulated as

$$\text{O}^0 + \text{O}^{2-} = 2\text{O}^- \quad (2)$$

where O^0, O^- and O^{2-} represent the bridged, broken and free oxygens. In the CaO–SiO_2 system, for example, the SiO_2 tetrahedra network can be gradually broken down with the addition of CaO, and the bridged oxygen bonds can be almost completely broken at the orthosilicate (Ca_2SiO_4) composition.

Toop and Samis [6] were the first to calculate the Gibbs energy and activities of oxides in binary silicate melts using the equilibrium constant of the depolymerization reaction (2). Yokokawa and Niwa [7,8] adopted the depolymerization reaction (2) and calculated the configurations of silicon atoms on the quasi-lattice in binary silicate melts. The configuration (entropy) and Gibbs energy of the melts are dependent on the strength of the depolymerization reaction (2). The activities of MO and SiO_2 were properly calculated in binary MO–SiO_2 melts. The model was also successfully extended to ternary silicate solutions such as the CaO–MnO–SiO_2, CaO–MgO–SiO_2 and CaO–FeO–SiO_2 melts with the ideal solution assumption between basic oxides. Kapoor and Frohberg [9] developed a similar model to describe the ternary CaO–FeO–SiO_2 silicate melts with the assumption of a non-ideal solution between basic oxides.

Masson et al. [10] developed a model that considers the formation of various silicate chains.

$$\text{SiO}_4^{4-} + \text{Si}_n\text{O}_{3n+1}^{2(n+1)} = \text{Si}_{n+1}\text{O}_{3n+4}^{2(n+2)-} + \text{O}^{2-}. \quad (3)$$

The amount of different silicate chains in molten silicates can be calculated from the equilibrium constants of reaction (3). Masson et al. [10] optimized the equilibrium constants of the reaction (3) for various binary silicate systems and calculated the activity of the MO. Gaskell [11] extended the concept of Masson et al. and calculated the Gibbs energy of binary silicate melts by introducing an appropriate entropy of mixing term based on the Guggenheim equation for mixing of anions in linear and branching chains.

Lin and Pelton [12] proposed an ionic model for binary MO–SiO_2 melts. The entropy of solution was calculated over the entire composition range based on the random distribution of O^{2-}, O^- and O^0 over quasi-lattice sites in binary silicate melts. The main model parameter was ΔG for reaction (2) which was described as a function of SiO_2 concentration. The value of ΔG was determined to reproduce the phase diagrams of binary silicate systems as well as thermodynamic properties of the melt. The complex silicate chain structure proposed by Masson et al. [10] could be calculated a posteriori. The model has been extended to ternary MgO–FeO–SiO_2 and CaO–NiO–SiO_2 silicate systems by Romero and Pelton [13,14].

These structure-related models for molten slags have been further developed and adopted in the presently available thermodynamic packages. The best-known models are the Associate Model, the Cell Model, the Modified Quasichemical Model and the Reciprocal Ionic Liquid Model. As the similarities and differences between these models were recently reviewed by Pelton [15], no detailed mathematical formulations of the models will be discussed in the present study.

2.1.1. The Modified Quasichemical Model

The Modified Quasichemical Model (MQM) was introduced by Pelton and Blander [16,17]. The most recent version of the model is discussed in a series of articles [18–21]. The MQM has been used for the FACT slag database of FactSage [22]. The silicate network breaking reaction (reaction (2)) can be equivalent to the following quasichemical reaction among second-nearest-neighbor pairs.

$$(\text{M–M}) + (\text{Si–Si}) = 2(\text{M–Si}) \qquad \Delta g_{\text{MSi}} \quad (4)$$

where (*i*–*j*) represent (*i*–O–*j*) pairs in molten slags. (M–M), (Si–Si) and (M–Si) are equivalent to free (O^{2-}), bridged (O^0) and broken (O^-) oxygen, respectively, in reaction (2). The short-range ordering in molten silicate is taken into account through the above quasichemical reaction. The molar Gibbs energy of the reaction Δg_{MSi} is the main model parameter, which is expanded as an empirical polynomial in composition and temperature. The configuration entropy is given by randomly distributing the pairs over imaginary pair sites. The molar Gibbs energy of the binary MO–SiO_2 solution can be expressed as

$$\begin{aligned} G^m = {} & (x_{\text{MO}} g^o_{\text{MO}} + x_{\text{SiO}_2} g^o_{\text{SiO}_2}) + (Z_{\text{M}} x_{\text{MO}} + Z_{\text{Si}} x_{\text{SiO}_2}) \\ & \times (x_{\text{MSi}} \Delta g_{\text{MSi}}/4) + RT(x_{\text{MO}} \ln x_{\text{MO}} + x_{\text{SiO}_2} \ln x_{\text{SiO}_2}) \\ & + RT \frac{(Z_{\text{M}} x_{\text{MO}} + Z_{\text{Si}} x_{\text{SiO}_2})}{2} \left(x_{\text{MM}} \ln \frac{x_{\text{MM}}}{Y^2_{\text{MO}}} \right. \\ & \left. + x_{\text{SiSi}} \ln \frac{x_{\text{SiSi}}}{Y^2_{\text{SiO}_2}} + x_{\text{MSi}} \ln \frac{x_{\text{MSi}}}{2 Y_{\text{MO}} Y_{\text{SiO}_2}} \right) \end{aligned} \quad (5)$$

where x_{MM}, x_{SiSi} and x_{MSi} are the pair fractions, Z_{M} and Z_{Si} are the second-nearest-neighbor coordination numbers of M and Si ($Z_{\text{Si}}/Z_{\text{M}}$ is the valency ratio of Si and M cations), and Y_{MO} and Y_{SiO_2} are weighted mole fractions defined as $Y_{\text{SiO}_2} = (1 - Y_{\text{MO}}) = Z_{\text{Si}} x_{\text{SiO}_2}/(Z_{\text{M}} x_{\text{MO}} + Z_{\text{Si}} x_{\text{SiO}_2})$. The values of pair fractions at equilibrium at any overall composition x_{SiO_2} are determined by setting $\partial G/\partial x_{\text{MSi}} = 0$. This results in an equilibrium constant for reaction (4):

$$x^2_{\text{MSi}}/(x_{\text{MM}} x_{\text{SiSi}}) = 4 \exp(-\Delta g_{\text{MSi}}/RT). \quad (6)$$

Due to the coordination numbers Z_{M} and Z_{Si}, the maximum second-nearest-neighbor ordering of the M–Si can occur at $x_{\text{SiO}_2} = Z_{\text{M}}/(Z_{\text{M}} + Z_{\text{Si}})$. For example, the maximum ordering for the CaO–SiO_2 slag occurs at the Ca_2SiO_4 composition. The very

negative Δg_{CaSi} results in $x_{CaSi} \approx 1$ near $x_{SiO_2} = 1/3$, and virtually all Ca atoms have Si atoms as second-nearest neighbors and vice versa; that is, the calculated structure of the melt is equivalent to Ca_2^{2+} SiO_4^{4-}. Although the relative value of coordination numbers of M^{2+} and Si^{4+} in the silicate melts is $Z_M/Z_{Si} = 1/2$, which reflects the silicate network structure, the actual values of Z_M (1.3774) and Z_{Si} (2.7548) used in the model are not exactly reflecting the network structure. Thus, the coordination number in the MQM is to some extent arbitrary.

The thermodynamic properties of ternary solutions can be calculated using a proper interpolation technique from binary model parameters, Δg_{MSi}. Depending on the chemistry of the given ternary system, different kinds of interpolation technique can be applied [23]. For example, the thermodynamic properties of the CaO–MgO–SiO_2 solution [24] can be well calculated using the Toop-like interpolation technique with SiO_2 as an asymmetric component. In the case of the CaO–Al_2O_3–SiO_2 aluminosilicate system, either the Kohler-type or the Toop-type interpolation technique can be used (in fact, the MQM uses the Toop-type interpolation technique for ternary aluminosilicate melts with SiO_2 as an asymmetric component [25]). The Kohler type of interpolation technique is used for ternary solutions such as CaO–MgO–FeO [26]. Because the MQM permits a flexible choice of interpolation techniques for any given ternary systems, high predictive ability can be obtained in the multicomponent systems. Many binary, ternary and multicomponent slags [24–52] have been successfully modeled with the MQM.

Recently, the two-sublattice MQM [20,21] has been developed with quadruplet approximation. The previously optimized model parameters for oxide melts can be easily included in the two-sublattice MQM without losing any accuracy. The two-sublattice model has been successfully applied to molten slag containing sulfur [53] and fluorine [54]. This model has been widely used for molten salts containing different cations and anions.

2.1.2. The Cell Model

The Cell Model originally introduced by Kapoor and Frohberg [9] has been further developed by Gaye and Welfringer [55] for the IRSID slag database [55–59]. The model treats the melt as a mixture of cells such as (A–O–B), where A and B are cations in the melt. For example, M–O–M, M–O–Si and Si–O–Si cells can be considered in the MO–SiO_2 system, which are equivalent to free (O^{2-}), broken (O^-) and bridged (O^0) oxygen, respectively. In a similar way to the MQM, the network breaking reaction can be represented by the following cell formation reaction:

$$(\text{M–O–M}) + (\text{Si–O–Si}) = 2(\text{M–O–Si})$$
$$\Delta G = 2W_{\text{Si–M}}. \quad (7)$$

The model parameters are the cell formation energy $W_{Si–M}$ and the cell interaction energy $E_{Si–M}$, which are expressed as functions of temperature and composition.

Although it is not specified in the Cell Model, the Gibbs energy of a ternary solution is calculated from the binary parameters using the Toop-like interpolation technique with the most acidic component as an asymmetric component, which is similar to the MQM. Although the configuration entropy term of the Cell Model is somewhat different from that of the MQM, the basic concepts of both models are identical.

The Cell Model can satisfactorily reproduce the phase diagram and the constituent activity for ternary MO–NO–SiO_2 silicate melts, where M and N are divalent cations (Ca, Mg, Fe, Mn, Pb, etc.). However, for aluminosilicate melts such as the CaO–Al_2O_3–SiO_2 slag, neither the phase diagram nor the constituent activities were well predicted from the binary model parameters. Gaye and Welfinger [55] mentioned a poor agreement between experimental data and calculations in the high-SiO_2 region (above 50% of SiO_2) when approaching the Al_2O_3–SiO_2 binary corner of the CaO–Al_2O_3–SiO_2 system. In order to accurately reproduce the activity of SiO_2 and the phase diagram for common steelmaking slag compositions, the Al_2O_3–SiO_2 binary system was compromised. This difficulty with aluminosilicate slags seems to be due to the limited number of binary model parameters (maximum two binary parameters for each cell formation and cell interaction energy) and no adjustable ternary parameters. Zhang et al. [60] introduced more flexible polynomial functions for the cell formation energies as well as ternary model parameters. In this way, a more accurate phase diagram and more accurate activities of the components could be obtained in ternary aluminosilicate melts. For example, for the ternary CaO–Al_2O_3–SiO_2 system, two ternary parameters, $W_{Si–Ca–Al}$ and $W_{Si–Al–Ca}$, were introduced to modify the cell formation energy of $W_{Si–Ca}$ and $W_{Si–Al}$ as follows:

$$w_{i-j} = w_{i-j}^{(0)} + w_{i-j}^{(1)} x_i + w_{i-j}^{(2)} x_i^2 + \sum_k w_{i-j-k} \frac{x_k}{(1-x_i)}. \quad (8)$$

This modification is similar to the ternary parameters used in the MQM for the CaO–Al_2O_3–SiO_2 slag [25]. In order to overcome the shortcoming of the Cell Model, the General Central Atom (GCA) Model [61–63] is currently used for the IRSID (CEQCSI) slag database [59]. The GCA Model can readily treat two-sublattice (cationic and anionic sublattices) silicate melts containing non-oxygen anions such as S^{2-}. The previous parameters of the Cell Model can be used in the framework of the GCA model without losing any accuracy. In addition, more sophisticated and flexible interaction parameter terms can be introduced in the GCA Model to overcome the difficulty of the original Cell Model. For example, the GCA Model has satisfactorily reproduced the phase diagrams and activities of components in the CaO–Al_2O_3–SiO_2 [61] and MnO–Al_2O_3–SiO_2–MnS systems [63].

2.1.3. The Associate Model

The Associate Model has been used for oxide melt database of MTDATA [64]. The choice of the associate species composition is to some extent arbitrary. Even though liquid associate species can be usually selected from the congruent melting crystalline phases, they are fictive without considering the melt structure. For example, the thermodynamic properties of the binary CaO–SiO_2 system have been described by considering associate species, Ca_2SiO_4 and $CaSiO_3$, as well as end-member species, CaO and SiO_2 [65]. For the binary Al_2O_3–SiO_2 melt, an associate species $Al_4Si_3O_{12}$ has been considered. No associate species has been considered for the binary CaO–Al_2O_3 melt. In the ternary CaO–Al_2O_3–SiO_2 melt, ternary associate species $CaAl_2Si_2O_8$ of anorthite composition can be added [66,67]. For example, the following association reaction can be considered for the binary MO–SiO_2 system.

$$x\text{MO} + \text{SiO}_2 = \text{M}_x\text{SiO}_{2+x} : \ \Delta g^o_{x\text{M–Si}}. \quad (9)$$

Then the Gibbs energy of the binary solution can be expressed as

$$G^m = \sum_{i=species} x_i g_i^o + RT \sum_{i=species} x_i \ln x_i + \sum_{i,j} x_i x_j \sum_{v\geq 0} L_{ij}^v (x_i - x_j)^v \quad (10)$$

where g_i^o and x_i are the Gibbs energy and the mole fraction of species i, respectively. The Gibbs energy of multicomponent systems can be expressed with the same formula. The main model parameters of the Associate Model are the formation energies of the associate species in reaction (9). The configuration entropy of solution is calculated by assuming a random distribution of the species in solution. The Gibbs energy of solution can be adjusted

by the introduction of interaction parameters between the species, L_{ij}. The amount of various species in the melt can be varied with temperature and composition, which is mainly determined by the formation energy of species and can be slightly adjusted by the excess interaction energy between the species.

Although the Associate Model may introduce a wrong configurational entropy in dilute solutions [18], the thermodynamic properties of binary oxide melts can be easily reproduced. The ternary and multicomponent systems can be relatively well managed with additional associate species and interaction parameters. Even quaternary associate species can be introduced, if necessary. Recently, Besmann et al. [68,69] and Yazhenskikh et al. [70,71] have built up the databases for the $CaO–Na_2O–Al_2O_3–B_2O_3–SiO_2$ and $Na_2O–K_2O–Al_2O_3–SiO_2$ systems, respectively.

2.1.4. The Reciprocal Ionic Liquid Model

The Reciprocal Ionic Liquid Model (RILM) was developed by Hillert et al. [72] and used as a standard model for the oxide melt database in Thermo-Calc [73]. This model supposes two sublattices in liquid oxide. For example, in the CaO–MgO–SiO_2 system [74], the liquid structure is formulated as

$$(Ca^{2+}, Mg^{2+})_P(SiO_4^{4-}, O^{2-}, SiO_2^0)_Q \tag{11}$$

where P and Q indicate the number of sites on each sublattice, which can vary with composition in order to maintain electron neutrality.

$$P = 4y_{SiO_4^{4-}} + y_{O^{2-}} \tag{12}$$

$$Q = 2y_{Ca^{2+}} + 2y_{Mg^{2+}} = 2 \tag{13}$$

where y is the site fraction of a species on a particular sublattice. The Gibbs energy of the ternary CaO–MgO–SiO_2 solution for one mole of formula unit is given by

$$\begin{aligned} G^m = {} & y_{Ca^{2+}}y_{SiO_4^{4-}}G_{(Ca^{2+})_4(SiO_4^{4-})_2} + y_{Mg^{2+}}y_{SiO_4^{4-}}G_{(Mg^{2+})_4(SiO_4^{4-})_2} \\ & + y_{Ca^{2+}}y_{O^{2-}}G_{(Ca^{2+})_2(O^{2-})_2} + y_{Mg^{2+}}y_{O^{2-}}G_{(Mg^{2+})_2(O^{2-})_2} \\ & + Qy_{SiO_2^0}G_{SiO_2^0} + PRT(y_{Ca^{2+}}\ln y_{Ca^{2+}} + y_{Mg^{2+}}\ln y_{Mg^{2+}}) \\ & + QRT(y_{SiO_4^{4-}}\ln y_{SiO_4^{4-}} + y_{O^{2-}}\ln y_{O^{2-}} + y_{SiO_2^0}\ln y_{SiO_2^0}) + G^E \end{aligned} \tag{14}$$

where $G_{(Ca^{2+})_4(SiO_4^{4-})_2}$ of the imaginary liquid $Ca_4Si_2O_8$ species is the main model parameter, $G_{(Ca^{2+})_2(O^{2-})_2}$ and $G_{SiO_2^0}$ are the Gibbs energies of liquid 2CaO and SiO_2, respectively, and G^E is the excess Gibbs energy of interaction between the species on the same sublattice, expanded as the Redlich–Kister polynomial of the site fraction. The amount of species in the anionic sublattice (SiO_4^{4-}, O^{2-} and SiO_2^0) is mainly determined by $G_{(M^{2+})_4(SiO_4^{4-})_2}$. The thermodynamic description of the RILM for the binary MO–SiO_2 solution is identical to that of the Associate Model considering only M_2SiO_4 associate species. Many binary and ternary oxide solutions have been optimized [74–83] using the RILM.

2.2. Oxide solid solutions

The Compound Energy Formalism (CEF) [84] has been used to describe complex and extensive oxide solid solutions such as spinel, melilite, pyroxene and olivine. In order to accurately describe the Gibbs energy of an oxide solution over a wide temperature range, the entropy of solution should be properly described based on its crystal structure. One of the most complex oxide solid solutions encountered in steelmaking is the spinel solution.

For example, the spinel solution of the Fe–Mg–Al–Cr–O system, encompassing Fe_3O_4, $FeAl_2O_4$, $FeCr_2O_4$, $MgFe_2O_4$, $MgAl_2O_4$, $MgCr_2O_4$ and Cr_3O_4, is of great importance for refractories in steelmaking. This solution can be modeled based on its crystallographic information:

$$[Fe^{2+}, Fe^{3+}, Mg^{2+}, Al^{3+}, Cr^{2+}, Cr^{3+}]^T \times [Fe^{2+}, Fe^{3+}, Mg^{2+}, Al^{3+}, Cr^{3+}, Va]_2^O O_4 \tag{15}$$

where T and O represent tetrahedral and octahedral sublattices in the spinel structure. Vacancies (Va) in octahedral sublattices are also taken into account. The Gibbs energy of the spinel solution can be expressed as follows, using the CEF:

$$G^m = \sum_i \sum_j Y_i^T Y_j^O G_{ij}^o - TS_C + G^E \tag{16}$$

where Y_i^T and Y_j^O represent the site fractions of constituents i and j on the tetrahedral and the octahedral sublattices, G_{ij}^o is the Gibbs energy of an end-member $[i]^T[j]_2^O O_4$, S_C is the configurational entropy:

$$S_C = -R\left(\sum_i Y_i^T \ln Y_i^T + 2\sum_j Y_j^O \ln Y_j^O\right) \tag{17}$$

and G^E is the excess Gibbs energy:

$$G^E = \sum_i \sum_j \sum_k Y_i^T Y_j^T Y_k^O L_{ij;k} + \sum_i \sum_j \sum_k Y_k^T Y_i^O Y_j^O M_{k;ij} \tag{18}$$

where $L_{ij;k}$ and $M_{k;ij}$ are the interaction energies between cations i and j on one sublattice when the other sublattice is occupied by k. The interaction energies, $L_{ij;k}$ and $M_{k;ij}$, can be internally set in the model as follows:

$$L_{ij} = L_{ij:k} = L_{ij:s} = \cdots. \tag{19}$$

$$M_{ij} = M_{k:ij} = M_{s:ij} = \cdots. \tag{20}$$

That is, the interaction between i and j in a sublattice is assumed to be the same regardless of the cations on the other sublattice.

There are 36 Gibbs energies of end-members to be determined in Eq. (16). Once the Gibbs energies of the end-members are well determined, the Gibbs energy function of the solution can be further modified using the interaction parameters. However, as the experimental data are mostly insufficient to determine the Gibbs energies of all end-members, certain logical and physically meaningful assumptions should be applied to fix the Gibbs energies properly.

For example, the spinel solution of the Mg–Fe–Al–O system encompasses $MgAl_2O_4$, $FeAl_2O_4$, Fe_3O_4 and $MgFe_2O_4$ stoichiometric spinels. Fig. 1 shows the schematic diagram of the thermodynamic model for the Mg–Fe–Al–O system [85]. For the sake of simplicity, vacancies are not considered. 16 Gibbs energies of end-members should be determined to describe the entire spinel solution. Each stoichiometric spinel solution has four end-members. Thermodynamic and crystallographic data (cation distribution between tetrahedral and octahedral sublattices) can be used to determine the Gibbs energies of four end-members. Sometimes, more than one set of end-member Gibbs energies can be obtained to describe a stoichiometric spinel solution or two adjacent stoichiometric spinel solutions due to the lack of experimental data to fix the Gibbs energies of all end-members simultaneously. As can be seen in Fig. 1, because the stoichiometric spinel solutions are connected to each other by a common end-member, the Mg–Fe–Al–O spinel solution composed of four stoichiometric spinels can form a closed-loop solution structure. This closed-loop structure can effectively constrain the Gibbs energies of end-members. The end-member Gibbs energies can also be properly estimated based on physically meaningful assumptions. For example, the reciprocal parameters, Δ_{ij} ($= G_{ii} + G_{jj} - G_{ij} - G_{ji}$), can be assumed to be about 40 kJ/mol, based on the extensive study on the 2–3 spinels by O'Neil

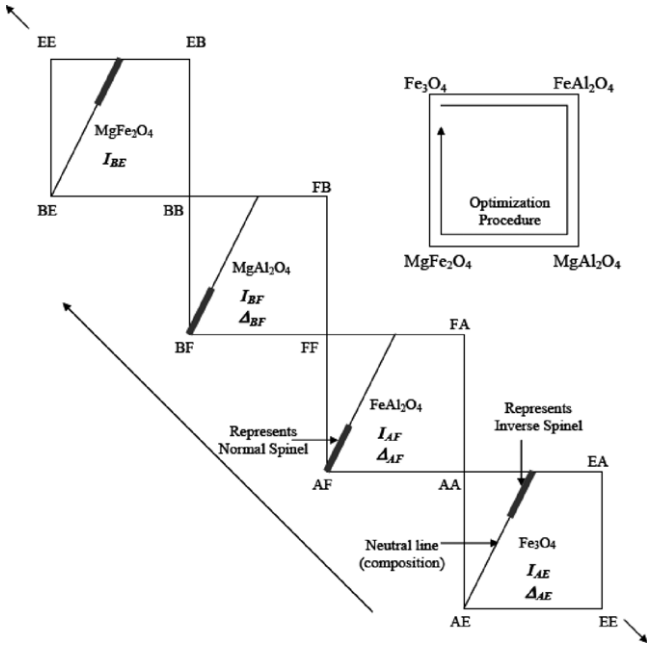

Fig. 1. Schematic diagram for the structure of the thermodynamic model of the Fe–Al–Mg–O spinel solution. E, A, F and B represent Fe^{3+}, Fe^{2+}, Al^{3+} and Mg^{2+} cations in the (Fe^{2+}, Fe^{3+}, Mg^{2+}, Al^{3+}) [Fe^{2+}, Fe^{3+}, Mg^{2+}, Al^{3+}]$_2O_4$ spinel solution [85].

and Navrotsky [86]. In addition, the magnetic properties of the spinel oxide solution should be taken into account. The spinel solutions in binary, ternary and multicomponent oxide systems have been modeled [26–32,82,87–89] using this approach.

Similarly, other extensive oxide solid solutions such as olivine, pyroxene, melilite and so on have been modeled based on their crystallographic data as well as thermodynamic properties and phase diagrams. Without proper considerations of the cation distribution, accurate entropy and Gibbs energy functions of the extensive solid solution can hardly be described.

2.3. Liquid steel

During the ironmaking and steelmaking processes, the thermodynamic behaviors of dilute elements such as C, O, and other metallic elements are very important. There are several models that are specially suited for handling the thermochemistry of dilute solutions.

The deoxidation reaction (Fe–M–O system) is one of the most important chemical reactions occurring in molten steel. For example, the standard Gibbs energy of M_xO_y oxide formation from pure M and O_2 is very well known:

$$xM + y/2O_2 = M_xO_y : \Delta G^o_{M_xO_y}. \tag{21}$$

Using the Gibbs energy change from the Raoultian to the Henrian standard state, the oxidation reaction involving $\underline{M}$ and $\underline{O}$ dissolved in liquid Fe can be written as

$$M = \underline{M} \qquad \Delta G^o = RT \ln \gamma^o_{\underline{M}} \tag{22}$$

$$1/2O_2(g) = \underline{O} \qquad \Delta G^o = RT \ln \gamma^o_{\underline{O}} \tag{23}$$

$$x\underline{M} + y\underline{O} = M_xO_y(s)$$

$$\Delta G^o = \Delta G^o_{M_xO_y} - RT(x \ln \gamma^o_M + y \ln \gamma^o_{\underline{O}}) \tag{24}$$

where γ^o_i is the Henrian activity coefficient of element i. Then the equilibrium constant of reaction (24) is

$$K_{=}a_{M_xO_y}/(f_{\underline{M}}x_M)^x(f_{\underline{O}}x_O)^y \tag{25}$$

where x_i is the mole fraction of element i, $f_{\underline{i}}$ is the activity coefficient of element i relative to the infinite dilution (Henrian) standard state, and $a_{M_xO_y}$ is the activity of M_xO_y.

The Gibbs energy of the ternary Fe–M–O solution dissolving a dilute amount of $\underline{M}$ and $\underline{O}$ can be described as

$$\begin{aligned} G^m = {} & (x_{Fe}g^o_{Fe} + x_M g^o_{\underline{M}} + x_O g^o_{\underline{O}}) \\ & + RT(x_{Fe} \ln x_{Fe} + x_M \ln x_M + x_O \ln x_O) \\ & + RT(x_{Fe} \ln f_{\underline{Fe}} + x_M \ln f_{\underline{M}} + x_O \ln f_{\underline{O}}) \end{aligned} \tag{26}$$

where $g^o_{\underline{i}} (= g^o_i + RT \ln \gamma^o_i)$ is the standard Gibbs energy of element i in the infinite dilution (Henrian) standard state.

2.3.1. Wagner Interaction Parameter Formalism

The Wagner Interaction Parameter Formalism (WIPF) [90] has been widely used for dilute solutions. This simple formalism can describe the activities of dilute elements as a function of solute compositions. For example, the activity coefficients of $\underline{M}$ and $\underline{O}$ in Eqs. (25) and (26) can be expressed as

$$\begin{aligned} \ln f_{\underline{M}} = {} & \varepsilon_{MM}x_M + \varepsilon_{MMM}x_M^2 + \varepsilon_{MO}x_O \\ & + \varepsilon_{MOO}x_O^2 + \varepsilon_{MMO}x_M x_O + \cdots \end{aligned} \tag{27}$$

$$\begin{aligned} \ln f_{\underline{O}} = {} & \varepsilon_{OO}x_O + \varepsilon_{OOO}x_O^2 + \varepsilon_{OM}x_M \\ & + \varepsilon_{OMM}x_M^2 + \varepsilon_{OOM}x_O x_M + \cdots \end{aligned} \tag{28}$$

where ε_{ij} and ε_{ijk} are the so-called first-order and second-order interaction parameters. (ε_{ij} and ε_{ijk} are identical to the conventional notations ε^j_i and ρ^{jk}_i, respectively.) The interaction parameter can be expressed as a function of temperature, $\varepsilon = a + b/T$. The WIPF assumes that $f_{\underline{Fe}} = 1$, and $\varepsilon_{ij} = \varepsilon_{ji}$. Other interaction parameters may be included in the expansion to account for interactions with other alloying elements. The activity given in Eqs. (22)–(28) can be expressed as a function of the wt% of dilute elements with respective to the 1 wt% standard state. Since the WIPF is practical and easy for describing a dilute solution, it has been widely applied to the interpretation of chemical reactions occurring in the steelmaking process. The best-known assessments of the Henrian activity coefficients and interaction parameters for dilute liquid Fe solution are those of Sigworth and Elliot [91] and the JSPS [92].

Unfortunately, the WIPF is thermodynamically sound only in infinite dilution. As pointed out by Pelton and Bale [93], the WIPF cannot satisfy the Gibbs–Duhem equation and other thermodynamic constraints except for infinite dilute solution. Thus, the WIPF cannot directly be used in a thermodynamic software package.

2.3.2. Unified Interaction Parameter Formalism

The Unified Interaction Parameter Formalism (UIPF) is a modified Wagner Interaction Parameter Formalism. In order to overcome the shortcoming of the WIPF and to be consistent with the Gibbs–Duhem equation and other thermodynamic relationships, Pelton and Bale [93–95] modified the activity coefficient forms of the Wagner formalism for the Fe–*i*–*j*–*k* ... solution as follows, and called the formula the UIPF:

$$\ln f_{\underline{i}} = \sum_{j=1}^{N} \varepsilon_{ij}x_j + \sum_{j,k=1}^{N} \varepsilon_{ijk}x_j x_k + \ln f_{Fe} \tag{29}$$

$$\ln f_{Fe} = -\frac{1}{2}\sum_{j,k=1}^{N} \varepsilon_{jk}x_j x_k - \frac{2}{3}\sum_{j,k,l=1}^{N} \varepsilon_{jkl}x_j x_k x_l. \tag{30}$$

This modification does not increase the number of model parameters. The parameters ε_{ij} and ε_{ijk} of the UIPF can be calculated from

conventional interaction parameters from compilations [91,92] using the following standard formalisms [94]:

$$\varepsilon_{ij} = \varepsilon_{ji} = \varepsilon_i^j = \varepsilon_j^i \tag{31}$$

$$\varepsilon_{ijk} = \varepsilon_{ikj} = \varepsilon_{jik} = \varepsilon_{jki} = \varepsilon_{kij} = \varepsilon_{kji} \tag{32}$$

$$2\varepsilon_{ijj} = 2\rho_i^j + \varepsilon_j^j = \rho_j^{ij} + \varepsilon_i^j \tag{33}$$

$$2\varepsilon_{ijk} = \rho_i^{jk} + \varepsilon_j^k = \rho_j^{ik} + \varepsilon_i^k = \rho_k^{ij} + \varepsilon_i^j \tag{34}$$

where ε_i^j and ρ_i^{ij} represent the first-order and second-order interaction parameters in the WIPF, respectively. The UIPF is no longer limited to dilute solutions. It can be used to describe the complete range of binary, ternary and multicomponent systems. Lee [96] used the UIPF to describe the thermodynamic properties of the entire ternary Mn–Fe–C liquid solution. Li and Morris [97] also applied the UIPF for the Mn–Fe–C–Si system. The UIPF can be converted to a normal polynomial Gibbs energy expression [98]. For example, it can be converted to the Bragg–Williams Redlich–Kister polynomial model and vice versa.

The UIPF has been used for the dilute liquid Fe solution databases of FactSage [2], CEQCSI [1] and MTDATA [4].

2.3.3. Modified regular solution model

Hillert [99] demonstrated that Darken's quadratic formalism [100] can be transformed to a regular solution model with modification of the standard states of dilute elements:

$$G^m = x_{\mathrm{Fe}} g^o_{\mathrm{Fe}} + \sum_{i=solute} x_i(g_i^o + \mathrm{M}_i) + RT\big(x_{\mathrm{Fe}} \ln x_{\mathrm{Fe}} + \sum_{i=solute} x_i \ln x_i\big) + \frac{1}{2}\sum_{i,j=\mathrm{Fe},solute} x_i x_j L_{ij} \tag{35}$$

where all $L_{ii} = 0$ and $L_{ij} = L_{ji}$. M_i, which is related to the change of standard states from Raoultian to Henrian solution, and the regular solution parameters, L_{ij}, can be determined from conventional interaction parameters:

$$(\mathrm{M}_i + L_{\mathrm{Fe}\,i})/RT = \ln \gamma_i^o \tag{36}$$

$$(L_{ij} - L_{\mathrm{Fe}\,i} - L_{\mathrm{Fe}\,j})/RT = \varepsilon_i^j \tag{37}$$

$$-2L_{\mathrm{Fe}\,i}/RT = \varepsilon_i^i \tag{38}$$

$$L_{ij}/RT = \varepsilon_i^j - (\varepsilon_i^i + \varepsilon_j^j)/2. \tag{39}$$

The dilute liquid Fe solution database in Thermo-Calc has been developed using the modified regular solution model. Since the second order interaction parameters are not well counted in the model, the reassessment of the previously compiled interaction parameters seemed to be required in many cases.

Recently, Miki and Hino [101–103] used the Redlich–Kister polynomial equation with a quadratic function of the excess parameters:

$$G^m = \sum x_i g_i^o + RT\sum x_i \ln x_i + \sum x_i x_j(\Omega_{ij}^0 + \Omega_{ij}^1(x_i - x_j)) \tag{40}$$

where i and j correspond to Fe and solute elements. Instead of using the Henrian standard state, the Raoultian standard state is used for all solute elements. Since it is hard to define the Gibbs energy of pure liquid (Raoultian liquid state) for gaseous elements such as O_2. H_2 and N_2, the dissolved gaseous elements at 1 atm pressure of pure gases were selected as the standard state. In this way, the Gibbs energy of the liquid solution can be described. For example, the deoxidation equilibrium of the entire Fe–Ni–Al system [102] was described by this approach.

2.3.4. Associate Model for deoxidation

In order to describe the deoxidation equilibria of liquid Fe solution, it is usually necessary for the cross-interaction parameters $\varepsilon_{\mathrm{M}}^{\mathrm{O}}$, $\rho_{\mathrm{M}}^{\mathrm{O}}$, $\rho_{\mathrm{O}}^{\mathrm{M}}$, $\rho_{\mathrm{M}}^{\mathrm{M,O}}$ and $\rho_{\mathrm{O}}^{\mathrm{O,M}}$ to be very negative in order to account for the very strong attractive interactions between dissolved $\underline{\mathrm{M}}$ and $\underline{\mathrm{O}}$ atoms. Furthermore, in order to reproduce the measured data over a range of temperature, the interaction parameters must generally have a strong empirical temperature dependence, usually expressed as $\varepsilon = a + b/T$ (and $\rho = c + d/T$). By using many empirical parameters, the interaction parameter formula reproduces the measured deoxidation equilibria over a limited range of temperature and composition. However, the resultant equations extrapolate very poorly outside this range. In the case of very strong deoxidants such as Ca, Mg and Ba, the interaction parameter formalism has been found to be incapable of providing a satisfactory description of the deoxidation equilibria even over the temperature and composition ranges of the measured data.

The failure of the WIPF for very strong deoxidation systems results essentially from a wrong assumption of the behavior of solute atoms in liquid Fe. Intrinsically, the WIPF assumes that all solute elements in liquid Fe are distributed randomly and separately regardless of the interaction between solutes. However, physically, it can be easily presumed that the behavior of a strong deoxidation element is no longer independent of oxygen, and vice versa. Thus, when there is strong negative interaction between $\underline{\mathrm{M}}$ and $\underline{\mathrm{O}}$, the configurational entropy of liquid Fe solution is easily overestimated by the WIPF. In order to overcome this problem of the WIPF, Jung et al. [104] considered the associate formation in liquid steel to resolve this strong deoxidation phenomenon. For example, for a ternary liquid solution Fe–M–O, where Fe is the solvent and M is a metal solute, the solution is assumed to contain dissolved unassociated $\underline{\mathrm{M}}$ and $\underline{\mathrm{O}}$ atoms as well as dissolved molecules (associates) $\underline{\mathrm{M}*\mathrm{O}}$ and, in some systems at the highest concentrations of M, a small amount of $\underline{\mathrm{M}_2*\mathrm{O}}$ associates. The equilibria among the dissolved associates and the dissolved unassociated $\underline{\mathrm{M}}$ and $\underline{\mathrm{O}}$ atoms are represented by

$$\underline{\mathrm{M}} + \underline{\mathrm{O}} = \underline{\mathrm{M}*\mathrm{O}} \qquad \Delta g^o_{\underline{\mathrm{M}*\mathrm{O}}} \tag{41}$$

$$2\underline{\mathrm{M}} + \underline{\mathrm{O}} = \underline{\mathrm{M}_2*\mathrm{O}} \qquad \Delta g^o_{\underline{\mathrm{M}_2*\mathrm{O}}}. \tag{42}$$

The total amounts of M and O in solution are $n_{\mathrm{M}} = n_{\underline{\mathrm{M}}} + n_{\underline{\mathrm{M}*\mathrm{O}}} + 2n_{\underline{\mathrm{M}_2*\mathrm{O}}}$ and n_{O} ($n_{\mathrm{O}} = n_{\underline{\mathrm{O}}} + n_{\underline{\mathrm{M}*\mathrm{O}}} + n_{\underline{\mathrm{M}_2*\mathrm{O}}}$). The Gibbs energies of the associate formation, $\Delta g^o_{\underline{\mathrm{M}*\mathrm{O}}}$ and $\Delta g^o_{\underline{\mathrm{M}_2*\mathrm{O}}}$, are model parameters, instead of very negative interaction parameters ($\varepsilon_{\mathrm{M}}^{\mathrm{O}}$, $\rho_{\mathrm{M}}^{\mathrm{O}}$, $\rho_{\mathrm{O}}^{\mathrm{M}}$, $\rho_{\mathrm{M}}^{\mathrm{M,O}}$ and $\rho_{\mathrm{O}}^{\mathrm{O,M}}$), which can be obtained by evaluation/optimization of available data (deoxidation equilibria) for the Fe–M–O systems. Temperature-independent (i.e. constant) values of $\Delta g^o_{\underline{\mathrm{M}*\mathrm{O}}}$ and $\Delta g^o_{\underline{\mathrm{M}_2*\mathrm{O}}}$ were found to be sufficient, which indicates that the configurational entropy of the systems is well described by the Associate Model. No further interaction parameters such as $\rho_{\mathrm{O}}^{\mathrm{M,N}}$ are necessary to reproduce the deoxidation behavior of quaternary and higher-order Fe–M–N–$\cdots$–O systems. As showed by Jung et al. [104], the observed Ca deoxidation curve (Fe–Ca–O system), which is impossible to explain using the classical WIPF, can be easily reproduced with the Associate Model with only one temperature-independent model parameter. Similar results were found for the deoxidation equilibria by Mg, Ba, etc. Moreover, the Associate Model can explain other deoxidation phenomena by less strong deoxidant such as Al, Ti, Cr, V, Mn, Si, B, C, Ce, Nb and Zr. The FTmisc–FeLq database of FactSage for liquid Fe solution is formulated using the UIPF with the embedded Associate Model for the associate formations in Fe–M–O systems. That is, all the model parameters of the liquid Fe database are formulated using the UIPF, except for the cross-interaction terms of M–O that are replaced by the associate formation energies. The same model can be used for the desulfurization equilibria for Fe–M–S solution [105].

3. Thermodynamic packages and databases

3.1. CEQCSI

CEQCSI (Chemical Equilibrium Calculation for the Steel Industry) [58,59] is non-commercial software which was originally developed at IRSID, France, and has been developed continuously in ArcelorMittal Maizières, France, for their internal usage.

(a) The molten slag database covering the SiO_2–TiO_2–Ti_2O_3–CrO–Cr_2O_3–Al_2O_3–FeO–Fe_2O_3–MgO–MnO–CaO system is modeled based on the Cell Model [55]. The molten slag can also contain 10%–20% CaF_2 and a few % of sulfur. Recently, the Cell Model has been extended [57] to the oxysulfide SiO_2–Al_2O_3–FeO–Fe_2O_3–MgO–MnO–CaO–S systems. Recently, the GCA model [61–63], which is an advanced formalism of the Cell Model, has been tested in order to describe the Gibbs energy of a molten slag more accurately. A limited number of oxide solid solution phases such as pyroxene, spinel, melilite and halite were modeled in CEQCSI and most solid oxides are still treated as pure stoichiometric phases.

(b) The UIPF [93–95] is used for the liquid Fe solution with assessed interaction parameters. The database for liquid and solid steel phases based on the random-mixing Bragg–Williams Redlich–Kister model can also be employed in the calculations for high-alloyed steels. Recently, a new steel database has been developed using the GCA Model [61,63] for new steel grades which often have high alloying element contents as well as highly segregated phases. For example, the liquid Fe–Mn–P system was described [63] by the GCA Model.

(c) A kinetic model [63,106–108] to simulate the nucleation and growth of solid oxide and oxysulfide particles during the solidification of molten steels is also available.

3.2. FactSage

FactSage [22] is commercially available software which was introduced in 2001 as the fusion of the F*A*C*T/FACT-Win (Thermfact, Canada) and ChemSage (GTT-Technology, Germany) thermochemical packages. This software can perform complex equilibrium calculations with up to 32 elements, 40 non-ideal solution phases and over 1500 stoichiometric compounds simultaneously.

(a) The FACT oxide solution database (FToxid) contains consistently assessed and critically evaluated thermodynamic data for the molten slag phase, numerous extensive ceramic solid solution phases and all available stoichiometric compounds containing SiO_2–CaO–MgO–Al_2O_3–FeO–Fe_2O_3–MnO–TiO_2–Ti_2O_3–CrO–Cr_2O_3–ZrO_2–NiO–CoO–Na_2O–K_2O–B_2O_3–Cu_2O–As_2O_3–GeO_2–PbO–SnO–ZnO. The core Al_2O_3–CaO–FeO–Fe_2O_3–MgO–SiO_2 system has been fully optimized from 25 °C to above the liquidus temperatures at all compositions and oxygen partial pressures. Components such as B_2O_3, K_2O, Na_2O, CoO, CrO, Cr_2O_3, Cu_2O, MnO, NiO, PbO, SnO, TiO_2, Ti_2O_3, ZnO and ZrO_2 were added to this core six-component system and the relevant subsystems were optimized over the composition ranges important for industrial applications. The molten slag phase is described using the Modified Quasichemical Model (MQM) [16–21]. The dilute solubilities of gaseous species such as F, S, SO_4, PO_4, H_2O, OH, C, CO_3, CN, Cl, and I are also modeled using the Blander–Reddy Model [109–112]. Recently, the composition of S in molten oxide slag has been extended up to pure sulfide using the new two-sublattice MQM [53]. The same approach has been applied to other gaseous species such as F [54]. The extensive solid solutions such as spinel, olivine, melilite, monoxide, perovskite and wollastonite are modeled in the framework of the Compound Energy Formalism [84], taking into account the crystal structure of each solution. Over 50 solid oxide solutions are available in the FToxid database.

(b) The liquid Fe solution (FTmisc–FeLq) database was developed using the UIPF [93–95] with the well-known interaction parameters recommended by the JSPS [92]. This database covers 30 dilute elements in liquid Fe solution (Fe–Ag–Al–B–C–Ca–Ce–Co–Cr–Cu–H–La–Mg–Mn–Mo–N–Nb–Ni–O–P–Pb–Pd–S–Si–Sn–Ta–Ti–U–V–W–Zr). The deoxidation behaviors of Fe–M–O (M = Ca, Mg, Ba, Al, Ti, Cr, V, Mn, Si, B, C, Ce, Nb, Zr, …) systems are described by the Associate Model [104] in order to more accurately describe the deoxidation phenomena in liquid steel and to have high predictive ability for the deoxidation in multicomponent systems. FactSage also provides a dedicated steel database (FSStel) which is an updated version of the SGTE solution database [113] and is similar to the TCFE database in ThermoCalc.

(c) A viscosity database [114–116] for multicomponent molten slags containing SiO_2–CaO–MgO–Na_2O–K_2O–Al_2O_3–FeO–Fe_2O_3–MnO–NiO–CoO–PbO–ZnO–TiO_2–Ti_2O_3–B_2O_3–CaF_2 is available.

3.3. MPE

The MPE (Multicomponent Phase Equilibria) package [117,118] is a commercially available thermodynamic package which has been developed by the CSIRO, Australia. The package has been developed for applications related to ferrous and non-ferrous pyrometallurgical processes.

(a) The MPE oxide database contains consistently accessed binary and ternary thermodynamic parameters for molten slags, extensive solid solutions and stoichiometric solids containing SiO_2–P_2O_5–TiO_2–Ti_2O_3–Al_2O_3–Cr_2O_3–Fe_2O_3–FeO–CaO–MgO–CrO–NiO–MnO. The thermodynamic properties of molten slag are described by the Cell Model [55] like CEQCSI [1], although the MPE database has been developed separately. Extensive solid solutions such as halite, spinel, corundum, olivine, melilite, pyroxene and pseudo-brookite are also available to describe the oxide phase diagram accurately. The limited solubility of S in the molten slag can be also calculated. Recently, the database for molten slags of the SiO_2–Al_2O_3–Fe_2O_3–FeO–MnO–MgO–CaO–Na_2O–K_2O system has been developed based on the GCA (General Central Atom) Model in collaboration with CEQCSI group [62].

(b) The liquid Fe solution database covering Fe–Al–C–Ca–Cr–H–Mg–Mn–N–Ni–P–O–S–Si–Ti is available in the MPE package. The liquid database is modelled based on the random-mixing Bragg–Williams Redlich–Kister model, and the database is accurate for dilute concentrations of all elements except Mn, Ni and C, which can be accurately modelled up to a high concentration range.

(c) A viscosity database [119–121] for multicomponent slags containing SiO_2–CaO–MgO–Al_2O_3–FeO–Fe_2O_3–MnO–NiO–CoO–PbO–ZnO–TiO_2–Ti_2O_3–Cu_2O is available.

3.4. MTDATA

MTDATA [64] is a commercially available thermodynamic package which has been developed by the National Physical Laboratory (NPL), UK. The software can perform complex equilibrium calculations with up to 30 different components and 500 phases simultaneously.

(a) The oxide database (NPLOX) in MTDATA includes liquid oxide, solid solutions and stoichiometric compounds within the K_2O–Na_2O–CaO–MgO–FeO–Fe_2O_3–Al_2O_3–SiO_2–Cu_2O–S system with additions of B_2O_3, CaF_2, CoO, CrO, Cr_2O_3, Li_2O, Nb_2O_5, NiO, MnO, P_2O_5, PbO, V_2O_5, ZnO and ZrO_2. Dilute solutions of OH^-, SO_4^{4-} and CO_3^{2-} are also modeled for selected liquid oxide systems. The Associate Model is used for the liquid oxide phase,

and the extensive solid solutions such as spinel, olivine, melilite, monoxide, perovskite and wollastonite are modeled in the framework of the Compound Energy Formalism [84].

(b) The dilute liquid Fe solution database (FEDILSOL) contains 26 elements in liquid Fe (Fe–Ag–Al–B–C–Ca–Co–Cr–Cu–H–Mg–Mn–Mo–N–Nb–Ni–O–P–Pb–S–Si–Sn–Ti–U–V–W–Zr), which are described by the UIPF [93–95] with accessed interaction parameters. The TCFE liquid and solid steel database developed by the Thermo-Calc group can also be used for high-alloyed steel calculations.

(c) Calculations of volume [122] and density changes in the $CaO–MgO–FeO–Fe_2O_3–Al_2O_3–SiO_2$ system are possible.

3.5. Thermo-Calc

Thermo-Calc [73] is a commercially available software package which has been developed by KTH and Thermo-Calc software, Sweden. Multicomponent phase equilibria containing up to 40 different components can be calculated.

(a) Three metallurgical oxide databases are provided by Thermo-Calc. A former IRSID oxide database [55] based on the Cell Model (SLAG2) contains molten slag and solid phases of the $Al_2O_3–CaO–CrO–Cr_2O_3–FeO–Fe_2O_3–MgO–MnO–Na_2O–SiO_2$ system with limited solubilities of S, P, and F [56]. But the recent updates by the CEQCSI group are not included in the SLAG2 database. A subset of MTDATA's NPLOX oxide database (NOX2), which covers molten slag and solid phases in the $Al_2O_3–CaO–FeO–Fe_2O_3–MgO–SiO_2$ system, is also available. Thermo-Calc's own oxide database (ION3) based on the RILM [72] covers the $SiO_2–CaO–Al_2O_3–MgO–FeO–Fe_2O_3$ system with a minor amount of CrO, Cr_2O_3, MnO, Mn_2O_3, etc.

(b) The dilute liquid Fe solution database contains 26 dilute components in liquid Fe (Fe–Ag–Al–B–C–Ca–Co–Cr–Cu–H–Mg–Mn–Mo–N–Nb–Ni–O–P–Pb–S–Si–Sn–Ti–U–V–W–Zr), which are described by the regular solution model with modified interaction parameters from Sigworth and Elliot [91] and re-assessed parameters by Hillert [99]. The well-known TCFE steel database containing Al–B–C–Ca–Co–Cr–Cu–Fe–H–Mg–Mn–Mo–N–Nb–Ni–O–P–S–Si–Ti–V–W can also be used for high-alloyed steel calculations.

(c) The Dictra program [73] can perform solidification simulations for alloys with defined cooling rates as well as the solid-state diffusion simulations for steels.

4. Overview of steelmaking processes and chemistry

4.1. Steelmaking process

Fig. 2 shows an overview of the ironmaking and steelmaking processes. Liquid iron, called pig iron, is produced from the Blast Furnace (BF) where iron ores are reduced by coals (cokes) and injected air. During the reduction process, the gangue forms a molten oxide phase called slag. In order to enhance the slagging in the BF, $CaCO_3$ is also added. Molten iron tapped from the BF contains a high level of impurities (3–5C, 0.2–0.3Mn, 0.2–1.5Si, 0.06–0.12P, 0.02 S in wt%). The pig iron is then transferred to the Basic Oxygen Furnace (BOF) using a so-called torpedo car. The dephosphorization and desulfurization processes are frequently carried out in the torpedo car during the transfer to the BOF in order to reduce the burden for the BOF and secondary steelmaking processes. This is called the hot-metal pre-treatment. The main role of the BOF process is the reduction of carbon (decarburization) and phosphorus (dephosphorization) contained in molten iron by blowing oxygen. After the BOF process, liquid steel containing $C < 0.05$ wt% is tapped in a ladle. Since liquid steel after the BOF treatment still contains a high amount of oxygen (>0.05 wt%) and other impurities such as C, S, P and H, a secondary steelmaking process (also called a ladle refining process) is necessary to produce clean steels. Various unit equipments are used in the secondary refining process to remove impurities. For example, oxygen can be reduced by adding deoxidants such as Al, Mn and Si directly into the molten steel. Gaseous elements such as C and H can be further reduced in a vacuum degasser (RH). P and S can be further removed through chemical reactions with the top slag covering the molten steel. The liquid steel temperature can be increased and the chemical composition of the molten steel can be homogenized in a Ladle Furnace (LF). After the refining process, the steel chemistry can be adjusted by the addition of alloying elements to meet various steel grades. The molten steel is finally transferred to a tundish for casting in forms of slab, billet or broom. In the continuous casting process, oxyfluoride mould flux is normally used as a lubricant between the steel and the water-cooled Cu mould. When molten steel is produced from an Electric Arc Furnace (EAF) using steel scraps, it is directly moved to the secondary refining process. In the case of stainless steel production, primary stainless steel is generally produced from an EAF. It is further refined to mainly reduce C and P using special degasser equipments such as an Argon Oxygen Degasser (AOD) and a Vacuum Oxygen Degasser (VOD).

4.2. Overview of chemistry

Obviously, the most important phases and chemical constituents involved in the steelmaking process are Fe-rich metallic phases, oxide, oxysulfide and oxyfluoride phases. The important chemical systems for each steelmaking process can be listed as follows.

(1) Molten slag for refining process
   (a) $CaO–FeO–Fe_2O_3–SiO_2–MgO–P_2O_5$ system: BOF process
   (b) $CaO–MgO–Al_2O_3–SiO_2–FeO–Fe_2O_3$ system: ladle refining process
   (c) $CaO–MgO–SiO_2–CaF_2$ system: stainless steel refining
   (d) $CaO–CrO–Cr_2O_3–MgO–SiO_2$ system: AOD and VOD process for stainless steel
   (e) $CaO–MgO–SiO_2–MnO–CrO–Cr_2O_3$ system: high Mn stainless steel.

(2) Mould flux for casting process
   (a) $CaO–MgO–Al_2O_3–SiO_2–Na_2O–Li_2O–F$ system: conventional process
   (b) $CaO–MgO–Al_2O_3–SiO_2–Na_2O–Li_2O–B_2O_3$ system: new candidate.

(3) Non-metallic inclusions
   (a) $CaO–Al_2O_3–MgO–CaS$: conventional low carbon steels
   (b) $MnO–SiO_2–Al_2O_3–CaO–MnS$: wire steels and free-cutting steels
   (c) $MnO–SiO_2–Ti_2O_3–TiO_2–Al_2O_3$: high strength steels
   (d) $Al_2O_3–Ti_2O_3–TiO_2$: Interstitial-Free (IF) steels
   (e) Ti–Nb–C–N: High-Strength Low-Alloy (HSLA) steels containing Ti and Nb.

(4) Refractories
   (a) MgO–C: BOF and RH vessel refractories, ladle slag line
   (b) $MgO–Al_2O_3$: ladle castable
   (c) $MgO–Cr_2O_3–FeO–Fe_2O_3–Al_2O_3$: VOD and AOD refractories
   (d) $Al_2O_3–ZrO_2–SiO_2–C$: nozzle refractories and tundish plugs.

The following are important slag and solid oxide phases which can be encountered in a steelmaking process.

(a) Slag (molten oxide): $SiO_2–CaO–MgO–Al_2O_3–FeO–Fe_2O_3–MnO–TiO_2–Ti_2O_3–CrO–Cr_2O_3–Na_2O–Li_2O–B_2O_3$ with minor gas solubilities of S, P, F, H, C and N.

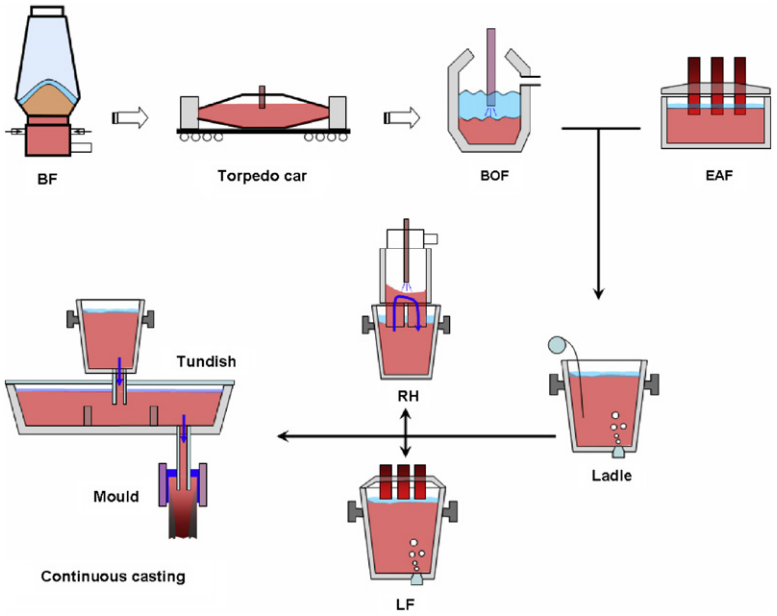

Fig. 2. Overview of ironmaking and steelmaking processes.

(b) Monoxide (halite): CaO–MgO–FeO–MnO with limited solubilities of Al_2O_3 and Fe_2O_3, which encompasses well-known lime (CaO), periclase (MgO) and wustite (FeO). A solid miscibility gap exists between CaO and MgO rich monoxides.

(c) α- and α'-Ca_2SiO_4: $(Ca, Mg, Fe, Mn)_2SiO_4$, which is a Ca_2SiO_4-rich phase.

(d) Olivine: (Mg, Fe, Ca, Mn) [Mg, Fe, Ca, Mn]SiO_4, which covers forsterite (Mg_2SiO_4) fayalite (Fe_2SiO_4), γ-Ca_2SiO_4, monticellite CaMg SiO_4, tephroite Mn_2SiO_4.

(e) Corundum: $(Al, Cr, Fe)_2O_3$, which is a solution of Al_2O_3, Cr_2O_3 and Fe_2O_3. Solid miscibility gaps exist between the constituents below about 1100 °C.

(f) Spinel: $(Mg, Fe^{2+}, Cr^{2+}, Mn^{2+}, Al^{3+}, Fe^{3+})[Mg, Fe^{2+}, Cr^{2+}, Al^{3+}, Fe^{3+}, Cr^{3+}, Mn^{3+}, Va]_2O_4$, which is an extensive solid solution containing $MgAl_2O_4$, $MgCr_2O_4$, $MgFe_2O_4$, $FeCr_2O_4$, Fe_3O_4, $FeAl_2O_4$, Cr_3O_4, $MnAl_2O_4$, $MnCr_2O_4$, $MnFe_2O_4$, etc.

(g) Mullite: non-stoichiometric $3Al_2O_3.2SiO_2$ phase.

(h) Wollastonite: $(Ca, Mg, Mn)SiO_3$, which is a $CaSiO_3$ rich phase stable below 1300 °C. Pseudo-wollastonite is stoichiometric $CaSiO_3$ stable below 1550 °C.

(i) Melilite: $Ca_2[Mg, Fe^{2+}, Fe^{3+}, Al](Fe^{3+}, Al, Si)_2O_7$. Akermanite $Ca_2MgSi_2O_7$ and gehlenite $Ca_2Al_2SiO_7$ form the melilite solid solution stable below 1590 °C.

(j) Pyroxene: (Mg, Ca, Fe)[Mg, Fe]Si_2O_6, which is a $MgSiO_3$ rich phase stable below 1560 °C. proto-, ortho-, low-clino-pyroxene exist. Clino-pyroxene is a $CaMg_2SiO_6$ rich phase, which is stable below 1390 °C. Small amounts of Fe_2O_3 and Al_2O_3 can be dissolved into pyroxene solutions.

(k) Pseudo-brookite: $(Fe, Mg, Mn, Ti^{3+})[Ti^{3+}, Ti^{4+}]_2O_5$, which is a solution of Ti_3O_5, $MnTi_2O_5$, $MgTi_2O_5$ and $FeTi_2O_5$.

(l) Ilmenite: $(Fe, Mg, Mn, Ti^{3+})[Ti^{3+}, Ti^{4+}]O_3$, which is a solution of Ti_2O_3, $MnTiO_3$, $MgTiO_3$ and $FeTiO_3$.

(m) Rhodonite: $(Mn, Ca)SiO_3$, which is a $MnSiO_3$ rich solid stable below 1300 °C.

(n) (Ti, Nb)(C, N): solid precipitates form during or after solidification of steels. FCC solution of TiC, TiN, NbC and NbN with miscibility gaps.

(o) Various stoichiometric compounds, including SiO_2, $xCaO \cdot yAl_2O_3$, anorthite $CaAl_2Si_2O_8$, CaS, CaF_2, cuspidine $Ca_4Si_2F_2O_7$.

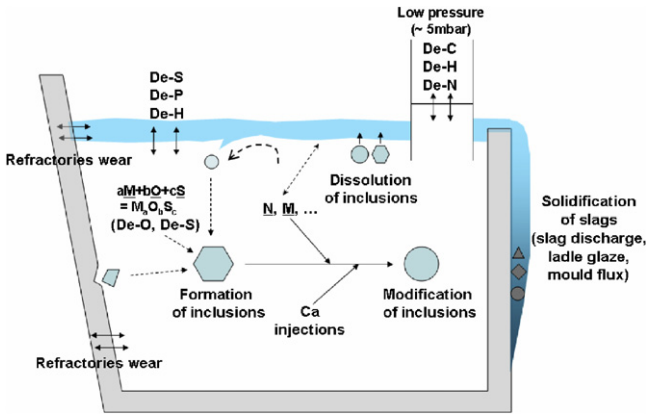

Fig. 3. Schematic diagram for major chemical reactions occurring in the steelmaking process.

5. Applications

Fig. 3 shows a schematic diagram of the main chemical reactions occurring in the steelmaking process: (1) liquid iron/inclusion, (2) liquid iron/slag, (3) slag/refractories, (4) slag/inclusion, and (5) liquid iron/refractories.

Figs. 4–7 show the phase diagrams and liquidus projections of various ternary and quaternary oxide systems of importance in the steelmaking process calculated with CEQCSI [1], FactSage [2], MPE [3], MTDATA [4] and Thermo-Calc [5].

5.1. Inclusion engineering

Inclusion control is the key to the production of clean or ultra-clean steel. Inclusions appear in steel at various stages of its production and cause serious problems such as nozzle clogging, crack initiation sites, degradation of surface quality and so on. Inclusions can be classified into two types: endogenous and exogenous. Endogenous inclusions are mainly formed during deoxidation, while exogenous inclusions are caused by slag entrapment, ladle glaze, erosion of refractories and steel reoxidation. In addition, inclusion precipitation can occur upon cooling and solidification of steel owing to the change in solubility of dilute elements with temperature. Although non-metallic inclusions can move to the steel

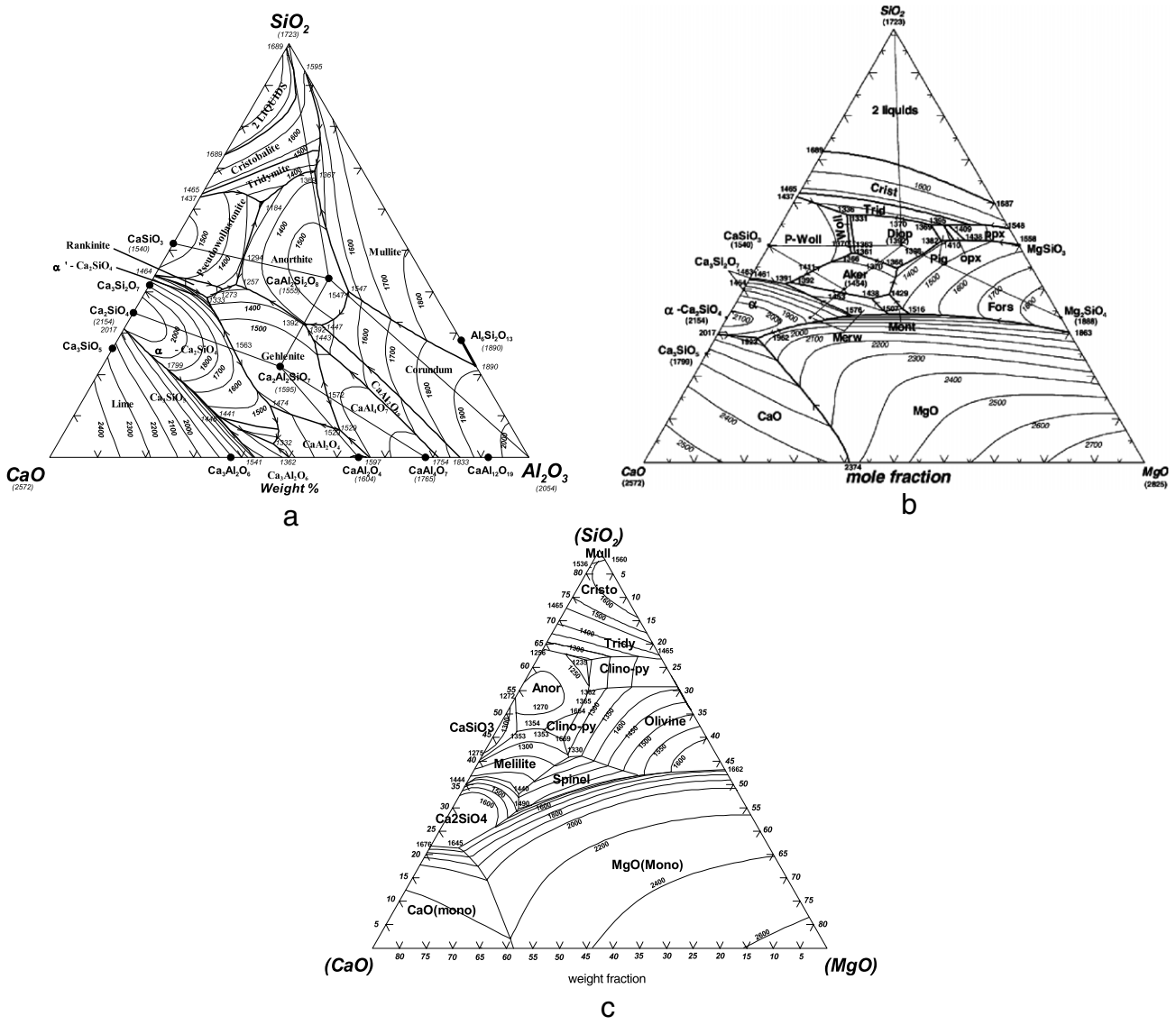

Fig. 4. Phase diagrams of (a) the CaO–Al_2O_3–SiO_2 [25], (b) the CaO–MgO–SiO_2 [24] and (c) the CaO–MgO–SiO_2–15 wt%Al_2O_3 [85] systems, calculated with FactSage [2].

surface where they are captured by top slag, the removal of inclusions is very limited during the process due to the short process time and the continuous circulation of liquid steel in the ladle. Since the presence of inclusions cannot be avoided, it is essential to modify their composition to render them less harmful in modern steelmaking processes. In some cases, composition-controlled inclusions can even be beneficial to steel properties.

Thermodynamically, the inclusion composition is very sensitive to the concentrations of even dilute elements in steel. Moreover, since the inclusions are composed of complex oxides, sulfides and/or nitrides, accurate thermodynamic databases for both steel and inclusions are essential to perform complex thermodynamic calculations. In order to find out which inclusion phases is stably formed at a given molten steel composition, so-called inclusion diagrams (inclusion stability diagrams) have been widely used for inclusion engineering [123] in steelmaking.

5.1.1. Mn/Si deoxidation

Although Al is one of the most common deoxidants widely used in the steelmaking process, undeformable Al_2O_3 inclusions are generated during Al deoxidation, which may provide crack initiation sites during the deformation of steel. In order to avoid the harmful Al_2O_3 inclusions, Mn/Si complex deoxidation, which results in the formation of inclusions of low melting temperature, is indispensable for the production of many high-value steels such as tire-cord steel, high-strength steel, and invar steel. The main goal of Mn/Si deoxidation is to obtain fully or partially liquid oxide inclusions even below 1200 °C. In actual steelmaking processes, Mn/Si deoxidation usually produces liquid MnO–Al_2O_3–SiO_2 inclusions as the deoxidation products. The inclusion chemistry is closely related to that of molten steel. The MnO–Al_2O_3–SiO_2 inclusions can gradually change to CaO–MnO–Al_2O_3–SiO_2 inclusions by indirect reaction with top slag containing CaO.

Fig. 8 shows the calculated liquidus projection of the MnO–Al_2O_3–SiO_2 system [44]. In order to obtain liquid oxide below 1200 °C, the concentrations of Mn, Si and Al in molten steel should be tightly controlled. Fig. 9(a) shows the variation of the MnO–Al_2O_3–SiO_2 inclusion composition with Mn/Si ratio in molten steel along with experimental data [124]. In addition, the concentrations of Al and O in equilibrium with the oxide inclusion are calculated in Fig. 9(b). In order to obtain liquid MnO–Al_2O_3–SiO_2 inclusions at 1200 °C, the Mn/Si ratio and the Al concentration should be controlled tightly: 2< (wt% Mn/ wt% Si) <10 and 0.1< wt ppm Al <0.5. In actual steelmaking practice,

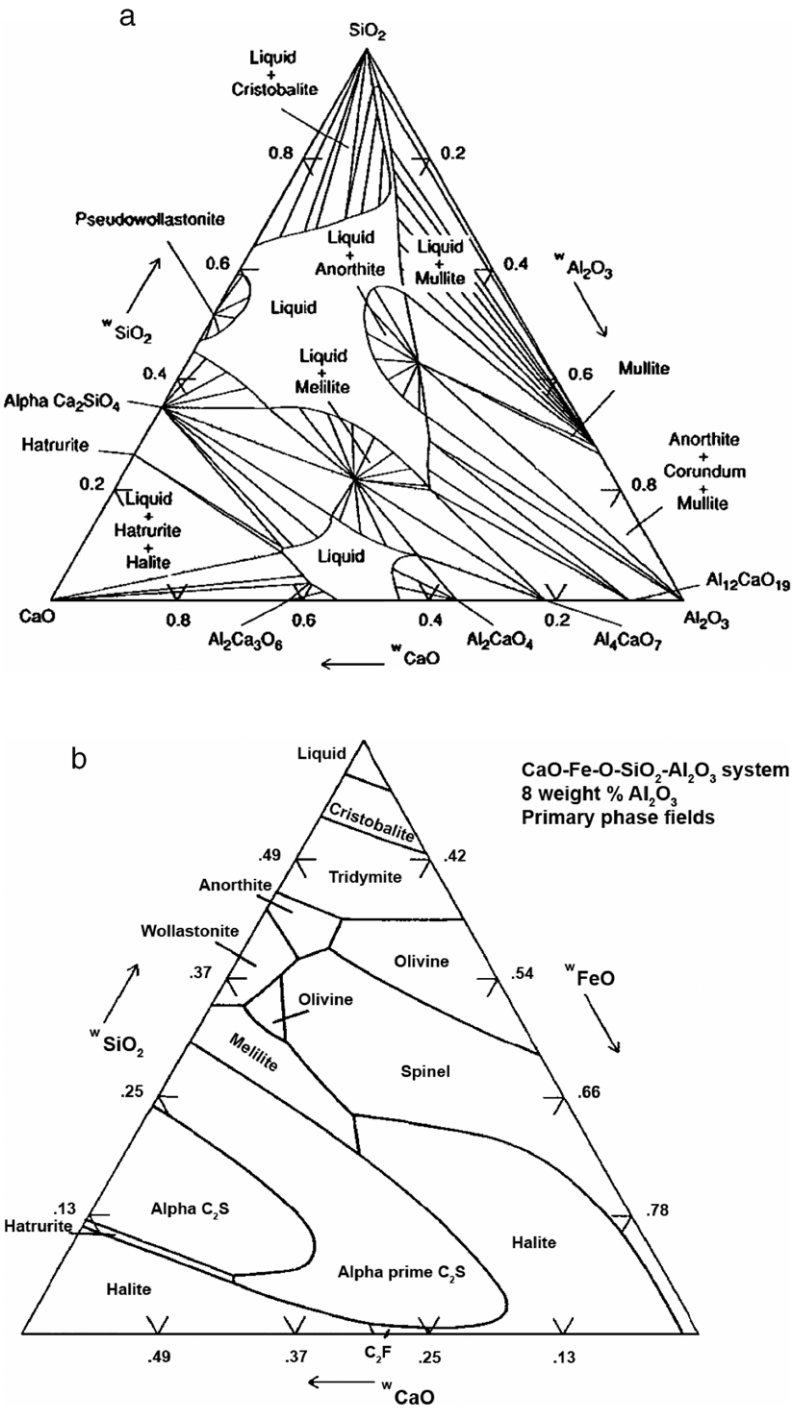

Fig. 5. Phase diagrams of (a) the CaO–Al_2O_3–SiO_2 [66] at 1500 °C and (b) the CaO–FeO–SiO_2 8 wt%Al_2O_3 [67] systems, calculated with MTDATA [4].

2.0 < Mn/Si < 3.0 is used in the deoxidation process. However, the Al content is hard to control within this range to obtain fully liquid oxide inclusions.

After deoxidation, the chemistry of the non-metallic inclusions can be indirectly modified by top slag chemistry via molten steel. The chemistry of the top slag can influence the chemistry of the molten steel, which can in turn alter the inclusion chemistry. In reality, the Al content in molten steel after Mn/Si deoxidation can be controlled by the top slag. Fig. 10 shows the chemical equilibrium between top slag and MnO–Al_2O_3–SiO_2 inclusions via molten steel. The top slag saturated with Ca_2SiO_4 and containing 15 wt% Al_2O_3 can provide about 3–5 wt ppm Al in molten steel at 1550 °C, which can subsequently produce liquid MnO–Al_2O_3–SiO_2 inclusions saturated with Al_2O_3 [125]. The chemistry of the ladle slag is therefore very important for control of the inclusion composition.

The inclusion chemistry can be further modified during the ladle furnace treatment. Fig. 11 shows the calculated compositional trajectory of the MnO–Al_2O_3–SiO_2 inclusions produced by the Mn/Si deoxidation process by indirect reaction with a top slag composed of 55CaO–15Al_2O_3–SiO_2 (in wt%) [126]. As can be seen in the diagram, the evolution of the inclusion composition in the course of the treatment can lead to a further decrease of their melting temperature.

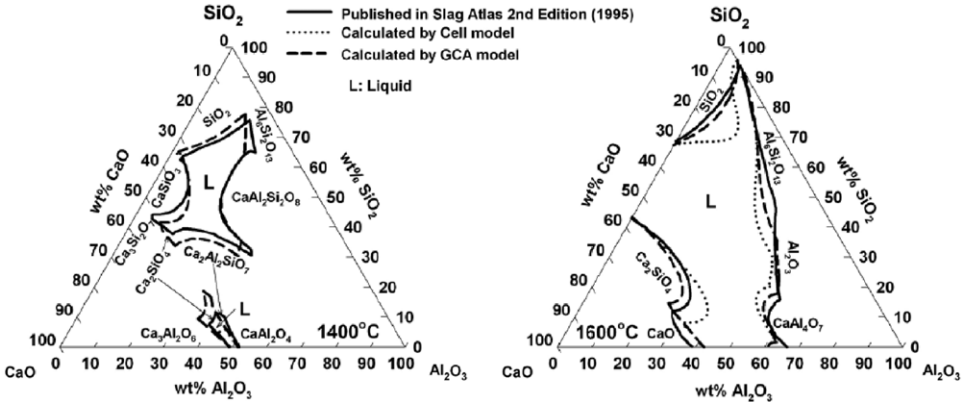

Fig. 6. Phase diagrams of the $CaO–Al_2O_3–SiO_2$ [62] system calculated with CEQCSI [2] and MPE [3].

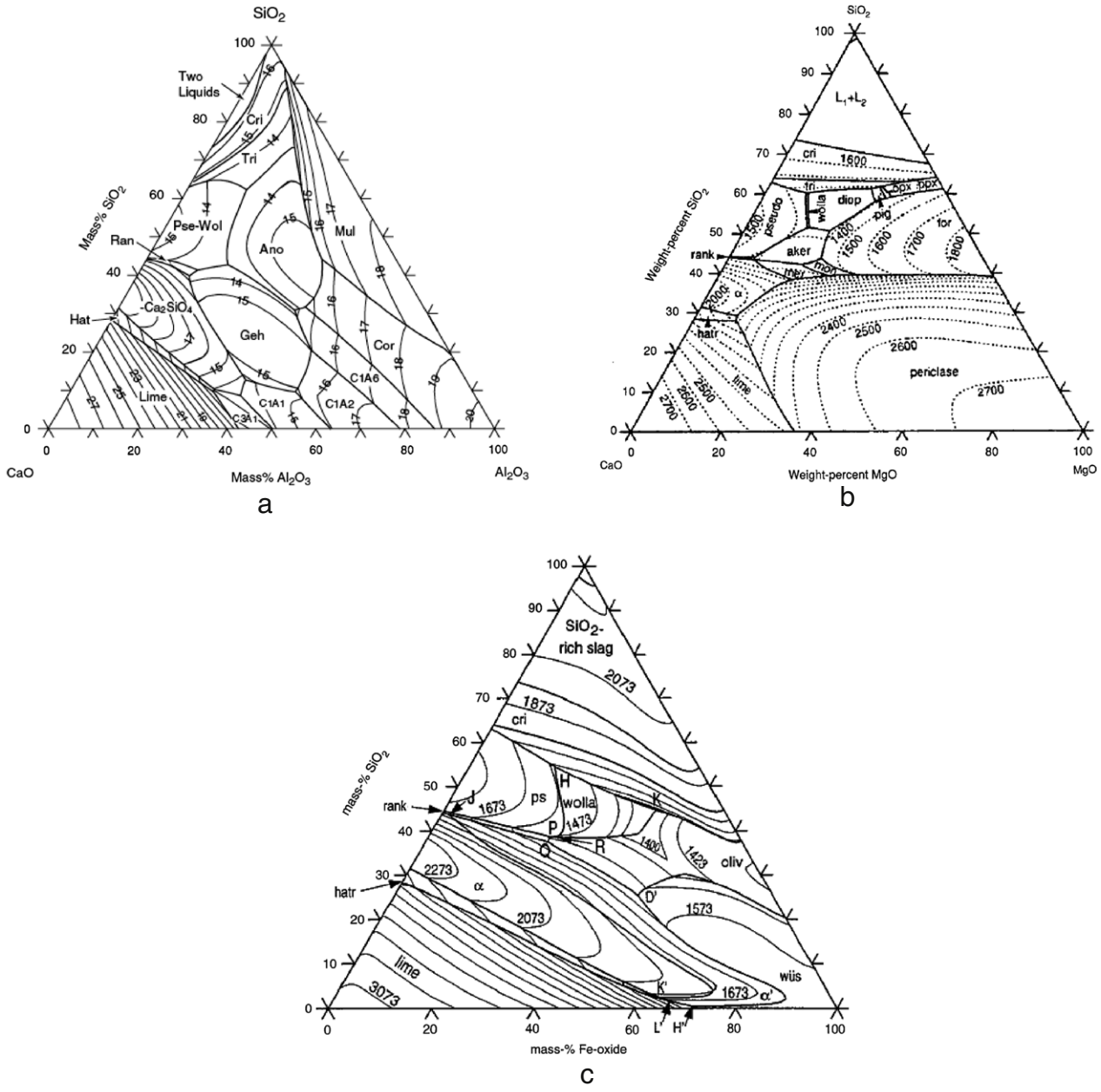

Fig. 7. Phase diagrams of (a) the $CaO–Al_2O_3–SiO_2$ [75] (temperature in °C), (b) the $CaO–MgO–SiO_2$ [74] (temperature in °C), and (c) the $CaO–FeO–SiO_2$ in Fe-saturation [77] (temperature in K), calculated with Thermo-Calc [5].

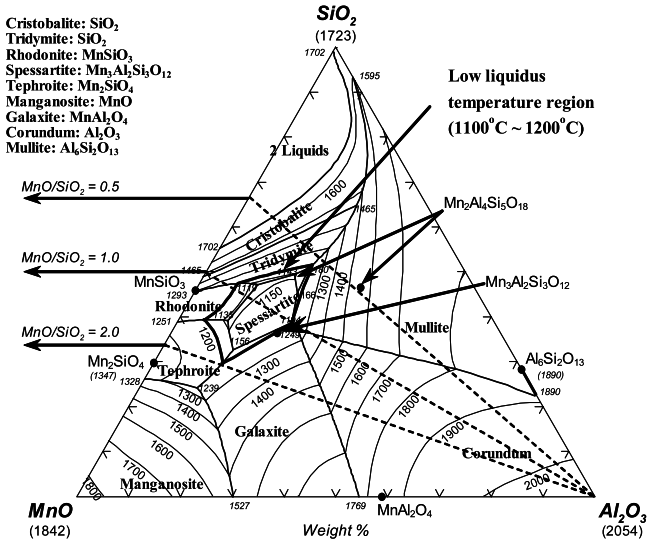

Fig. 8. Calculated liquidus surface of the MnO–SiO_2–Al_2O_3 system [44]. Temperature in °C.

5.1.2. Formation of oxysulfide inclusions

Free-cutting steels frequently contain high amounts of sulfur in order to distribute a large amount of oxysulfide precipitates, which can limit the machining chip length and form protective films on machining tools when steels are machined. Recently, accurate thermodynamic databases for various oxysulfide systems have become available both in CEQCSI and FactSage. For example, the liquidus projection and iso-thermal section of the MnO–SiO_2–MnS oxysulfide system of importance for free-cutting steels are calculated [53,125] in Fig. 12.

The formation of oxide, oxysulfide and sulfide inclusions in free-cutting steel Fe–0.07C–1.35Mn–0.014Si–0.35S–0.006O (in wt%) and the distributions of oxygen and sulfur between different inclusion types during the steel solidification are calculated in Fig. 13. The machinablity of free-cutting steels can be changed with the variation of inclusion type and relative amount of the inclusions, which can be well calculated using thermodynamic databases.

5.1.3. Inclusion diagram of Al/Ti deoxidation

A high probability of nozzle clogging events has been reported during the production of IF (Interstitial Free) steels containing a relatively high amount of Ti. The clog is formed by the accumulation of Al–Ti–O (Al_2O_3–TiO_2–Ti_2O_3) inclusions. Many experimental and thermodynamic studies [130–135] have been performed to understand the transitions of Al_2O_3 oxide inclusions, the reoxidation of IF steels, and the inclusion diagram of the Fe–Al–Ti–O system.

Fig. 14 shows the predicted phase diagram of the Al_2O_3–TiO_2–Ti_2O_3 system [134] at 1600 °C from the FactSage thermodynamic database. No comprehensive phase diagram study has been performed under steelmaking conditions. According to the predicted diagram, a liquid phase can exist at 1600 °C under low oxygen partial pressure ($P_{O2} \sim 10^{-13}$). The inclusion diagrams for Al/Ti complex deoxidation [130,134] are calculated in Fig. 15 using thermodynamic databases from, respectively, CEQCSI and FactSage. Although the calculation results are slightly different (for example, the well-known Ti_3O_5 was not taken into account in the CEQCSI calculation), the existence of a liquid oxide phase is predicted in both calculated diagrams. Usually, deoxidation of IF steels by Al addition is performed first, followed by Ti alloying (Ti = 0.07–0.2 wt% and Al = 0.03–0.05 wt%). According to the thermodynamic calculations in Fig. 15, the inclusions in IF steel should be composed of solid Al_2O_3. However, liquid and solid Al–Ti–O inclusions can be observed in the tundish, as a result of steel reoxidation by tundish slag. Liquid steel reoxidation can be caused by the reduction of less stable oxide components in slag such as SiO_2 and FeO by Al in molten steel [133,134]. As a result, the Al content in molten steel is locally decreased and may become sufficiently low for the formation of Al–Ti–O inclusions, as can be seen in Fig. 15. These Al–Ti–O inclusions can be readily attached to the submerged entry nozzle (SEN) wall, resulting in the nozzle clogging phenomenon.

5.1.4. Acicular ferrite formation

Although non-metallic inclusions are in general detrimental to the mechanical properties of steels, certain non-metallic inclusions can serve as nucleation sites for acicular ferrite formation, resulting in a significant improvement of the mechanical properties of steels. Various non-metallic inclusions including MnO–TiO_2, MnO–SiO_2–MnS, TiO_2–TiN and VN are known to promote acicular ferrite formation. Recently, Sarma et al. [136] reviewed the influence of non-metallic inclusions on acicular ferrite formation.

Many thermodynamic calculations [137–146] have been performed to describe the evolution of non-metallic inclusions with steel grades and temperature. Fig. 16 shows the changes in chemistry and morphology of non-metallic inclusions with the addition of various alloying elements in steels [140]. For example, the evolution of the inclusion chemistry with Ti content in Fe–0.1C–1.5Mn–0.1Si–0.01O–0.007S steel is calculated [140] in Fig. 17. According to the calculations using FactSage, the portion of liquid phase among the inclusions decreases with increasing Ti content. In the case of Ti = 104 and 122 ppm, the fraction of liquid inclusions becomes less than 20 mass% at 1200 °C. During the cooling process, the ilmenite phase becomes dominant with increasing Ti content. When Ti = 34 and 61 ppm, MnS precipitates can form from liquid inclusions after steel solidification. In contrast, when Ti = 104 and 122 ppm, MnS precipitation takes place during steel solidification. The calculation results were in agreement with the morphology of the observed inclusions in Fig. 16. That is, in the case of MnS precipitation from liquid inclusions, MnS was embedded in oxide inclusions; meanwhile, when MnS precipitation occurred during steel solidification, MnS wrapped oxide inclusions. The evolutions of non-metallic inclusion chemistry with varying Mg [138] and Al [139] contents in steel were also well explained by thermodynamic calculations.

Byun et al. [144] performed thermodynamic calculations using Thermo-Calc [73] with the SGTE database [113] to investigate the evolution of MnO–SiO_2 inclusions with increasing Ti concentration in Fe–0.08C–1.7Mn–0.2Si–0.004O–0.001N at 1477 °C. As can be seen in Fig. 18(a), the predictions revealed that $MnSiO_3$ inclusions gradually change to Mn_2TiO_4, $MnTiO_3$ and Ti_2O_3 with increasing Ti content, which was consistent with experimental observations. Similarly, Shim et al. [142] calculated the evolution of inclusions in Fe–0.14C–1.84Mn–0.18Si–0.011Ti–0.003O–0.001N steel with decreasing temperature (Fig. 18(b)). They found that a Mn-depleted zone (MDZ) forms around Ti_2O_3 ilmenite particles due to the absorption of Mn into ilmenite to form ilmenite solution Ti_2O_3–$MnTiO_3$. The presence of an MDZ near inclusions is considered to facilitate the austenite to ferrite transformation with acicular ferrite structure.

Kang and Lee [141] performed thermodynamic calculations to analyze the MDZ formation around Ti oxides in the temperature range between 1000 and 1500 °C as shown in Fig. 19. According to the calculations, the solubility of Mn in Ti_2O_3 ilmenite becomes maximized at 1175 °C, resulting in the largest MDZ formation. Based on the thermodynamic analysis, they suggested an optimal thermal process to maximize intergranular ferrite (IGF) development associated with MDZs.

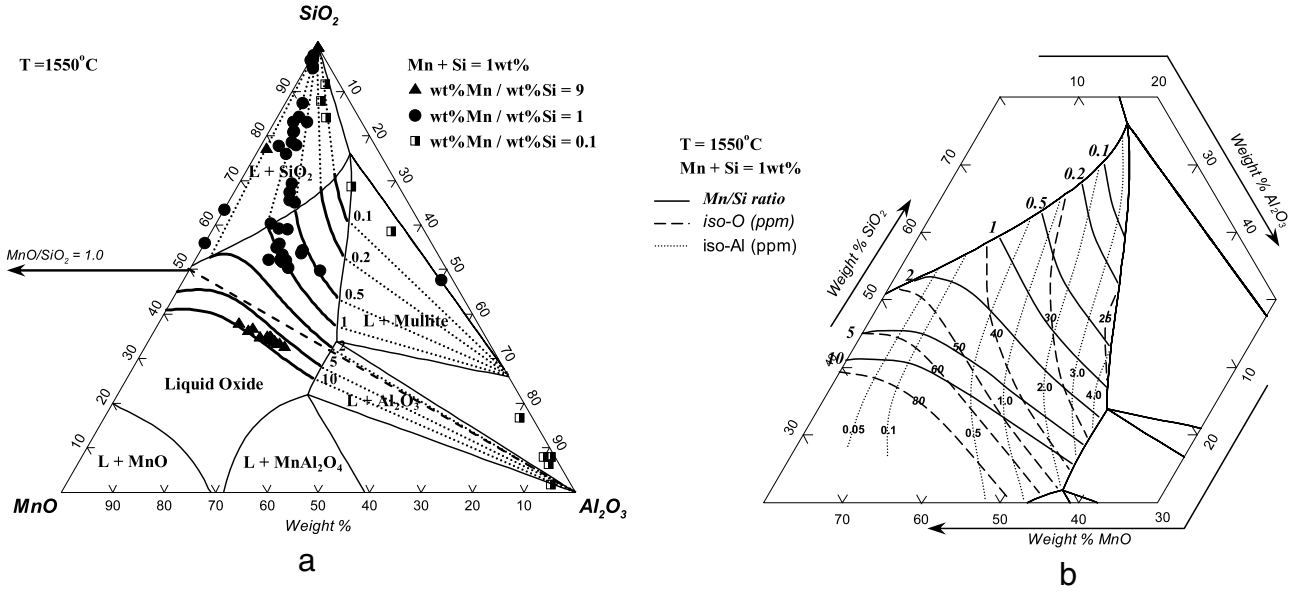

Fig. 9. Computed $MnO–Al_2O_3–SiO_2$ inclusion composition in equilibration with Mn/Si deoxidized steels at 1550 °C [44,124]. The lines with values indicate the composition of Mn/Si deoxidized steel. (a) Calculated inclusion composition in comparison with experimental data, and (b) calculated Mn/Si ratio, iso-oxygen and iso-aluminum in steels.

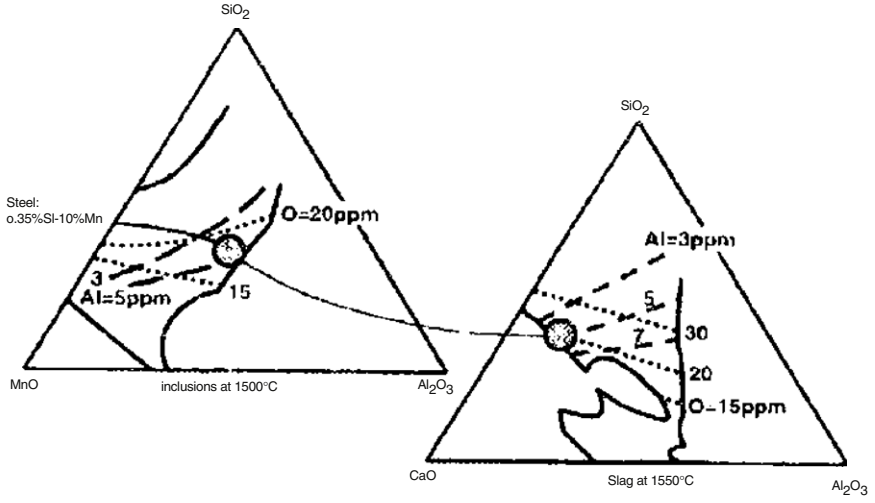

Fig. 10. The calculated isothermal sections of the phase diagram at $CaO–SiO_2–Al_2O_3$ at 1550 °C and $MnO–Al_2O_3–SiO_2$ at 1500 °C [125]. The dotted lines represent the Al and O in steel in equilibrium with the slag and inclusions. The circles indicated in both diagrams present the liquid $MnO–Al_2O_3–SiO_2$ inclusion composition produced by the $CaO–SiO_2–Al_2O_3$ top slag.

5.1.5. Ca treatment for Al-deoxidized steels

Although Al deoxidation is one of the most efficient deoxidation techniques in steelmaking, it produces a large amount of Al_2O_3 inclusions. In particular, dendritic Al_2O_3 inclusions can be easily deposited on ceramic nozzles, causing nozzle clogging. In order to minimize nozzle clogging, Ca treatment is widely used in secondary steelmaking. The addition of Ca in form of CaSi or CaFe wire can transform solid Al_2O_3 into liquid $CaO–Al_2O_3$ inclusions even below 1550 °C, resulting in less inclusion accumulation on the nozzles. In practice, the inclusion chemistry can be more complex due to the presence of sulfur in molten steel, which can form liquid $CaO–Al_2O_3–CaS$ and solid CaS.

Fig. 20 shows the predicted evolution of the chemical species at equilibrium after CaSi wire injection into 100 tons of liquid steel (Fe–0.003S–0.05Al in mass%) with suspended Al_2O_3 inclusions. In the calculations, no losses of CaSi (for example, through volatilization of Ca and through reactions with refractories) are assumed. The amount of suspended Al_2O_3 inclusions is set to be 100 mass ppm. As the CaSi wire is injected, solid Al_2O_3 is gradually converted to solid $CaAl_{12}O_{19}$and $CaAl_4O_7$. Thereafter, liquid oxide inclusions, composed of $CaO–Al_2O_3$ with a small amount of CaS, are formed. As the amount of CaSi increases further, solid CaS and solid CaO inclusions begin to precipitate and eventually become predominant. As can be seen in Fig. 20, CaS might form before CaO. Clearly, a higher initial [S] content in liquid steel will result in the precipitation of CaS at an earlier stage. If the [S] content is high enough, CaS might form even before liquid $CaO–Al_2O_3$. With the aid of such a diagram, the proper amount of CaSi to be injected in order to form liquid inclusions without forming harmful solid oxide or CaS inclusions can be calculated as a function of the initial [Al] and [S] contents, and the amount of suspended Al_2O_3 inclusions. Injection of CaSi is also useful to lower the S content in steel.

During the Ca treatment in the plant, non-equilibrium processes [147] rather than a gradual change of the Al_2O_3 inclusion composition as depicted in Fig. 20 are taking place. That is, when CaSi or CaFe wire is injected in Al-deoxidized molten steel in the ladle, liquid steel is locally enriched in Ca where Ca is injected. In the

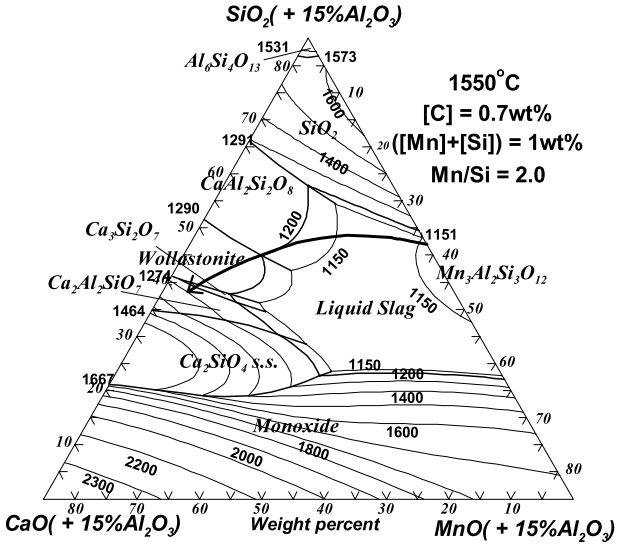

Fig. 11. Calculated change of composition of inclusions formed during Mn/Si deoxidation (as shown by arrows) when the Mn/Si ratio equals 2.0 for tire-cord steel ([C] = 0.7 wt%) by reaction with CaO-containing top slag at 1550 °C (top slag composition: 55CaO–15Al_2O_3–30SiO_2 in wt%). Predicted liquidus isotherms (T in °C) are also plotted [126].

Ca-enriched melt, Ca can react simultaneously with Al_2O_3 and S to form a mixture of solid xCaO–$y$$Al_2O_3$ oxides and CaS. When molten steel becomes homogeneous, the inclusion composition moves to equilibrium. Thus, inclusions with non-equilibrium composition (CaS + solid xCaO–$y$$Al_2O_3$) are produced in the early stage of the Ca treatment in the ladle. Their composition evolves to equilibrium (liquid CaO–Al_2O_3) later in the tundish.

Fig. 21 shows the evolution of the liquid inclusions obtained by the Ca treatment during steel solidification [148]. The liquid inclusions can be transformed back to CA_2, CA_3, CA_6 and Al_2O_3 with decreasing temperature. According to the calculations, the final inclusions after steel solidification can also depend on the [S] content in the molten steel, which was confirmed by the experimental measurement.

5.1.6. Kinetics of inclusion precipitation

A kinetic model of precipitation [59,106–108] combining thermodynamic data from CEQCSI and a nucleation/growth model of precipitates in the interdendritic liquid during steel solidification has been developed. Nucleation and growth of precipitates were considered simultaneously in the calculations. To calculate particle growth, a mixed controlled growth model combining solute transport and interfacial kinetics at the precipitate/liquid steel interface was considered. As an example, Fig. 22 shows the predicted TiN precipitation behavior during steel solidification in comparison with experimental results obtained from directional solidification experiments. The steel composition was Fe–0.002Mn–0.315Si–0.069Al–0.691Cr–0.092Ti–0.0016O–0.044 (or 0.0025)S–0.012N–0.40C (in wt%) and the cooling rate was 0.37 K/s [106]. Both TiN and MnS–FeS precipitates were observed during the experiments. As can be seen in Fig. 22, precipitation can occur below the equilibrium temperature by about 70 °C due to kinetic limitations arising from nucleation and growth phenomena. The precipitation of TiN was found to be retarded with increasing sulfur content. This was explained by the effect of sulfur on the interfacial energy between TiN and steel, influencing both the nucleation and the interfacial kinetics. The observed size distribution of TiN precipitates was also in satisfactory agreement with model calculations.

5.2. Slag/metal reactions

Molten slag in the steelmaking process plays many important roles such as liquid steel refining, dissolution of non-metallic inclusions, and prevention of liquid steel oxidation by air. In particular, the refining capacity of molten slag becomes more important for producing clean steels. For example, desulfurization and dephosphorization of molten steels during secondary steelmaking process are highly dependent on the chemistry of top slags.

The equilibrium reaction of sulfur between molten slag and steel can be expressed as

$$(O^{2-})_{slag} + [\underline{S}]_{steel} = (S^{2-})_{slag} + [\underline{O}]_{steel}. \quad (43)$$

The higher the distribution of sulfur, $L_S = (wt\%S^{2-})/[wt\%S]$, the lower the S content that can be achieved in molten steels. A more standardized representation of the refining capacity of molten slag can be defined as the following reaction:

$$O^{2-} + 1/2S_2(gas) = S^{2-} + 1/2O_2(gas). \quad (44)$$

Then the sulfide capacity in molten slag is expressed as

$$C_{S^{2-}} = (wt\%S^{2-})\frac{P_{O_2}^{1/2}}{P_{S_2}^{1/2}} = K_{S^{2-}}\frac{a_{O^{2-}}}{f_{S^{2-}}} \quad (45)$$

where $K_{S^{2-}}$ and $f_{S^{2-}}$ are the equilibrium constant of reaction (44) and the activity coefficient of S^{2-} in the molten slag, respectively. A slag with a higher sulfide capacity has a higher refining power to remove sulfur from molten steels. A semi-empirical model using optical basicity [149] has been used to describe the sulfide capacity in slag. This semi-empirical basicity model is satisfactory for the CaO–MgO–Al_2O_3–SiO_2 system. As pointed out by Lehmann and Gaye [57], however, it can lead to errors up to two or three orders of magnitude for FeO-bearing and MnO-bearing slags, due to the nonlinear behavior of FeO and MnO activities in the CaO–SiO_2 and MgO–SiO_2 slags.

The thermodynamic databases in CEQCSI and FactSage can reproduce the experimental data of the sulfide capacity in the CaO–MgO–SiO_2–Al_2O_3–FeO–Fe_2O_3–MnO–TiO_2–Ti_2O_3 system within experimental error limits [53,57,109]. Fig. 23 shows the sulfur distribution between CaO–SiO_2–Al_2O_3 slag and molten steel at 1600 °C. The calculated sulfur distributions, $L_S = (wt\%S)_{slag}/[wt\%S]_{steel}$, from CEQCSI [150] and FactSage [151] are quite similar to each other. The sulfide capacities of the CaO–SiO_2 slag calculated with FactSage [53] and MTDATA [67] are also presented in Fig. 24 along with experimental data [152–158].

The phosphorus distribution, $L_P = (wt\%P)_{slag}/[wt\%P]_{steel}$, between liquid iron and CaO-saturated CaO–Fe_tO–P_2O_5 slag at various temperatures is shown in Fig. 25. Experimental data from Nagabayashi et al. [159] at 1550, 1600 and 1650 °C are compared with calculations using the molten slag and FeLq databases of FactSage. The phosphorus distribution decreases with temperature and exhibits a maximum as the Fe_tO content in the slag increases. This can be explained by a combined effect of Fe_tO and CaO during the dephosphorization process. As can be seen from Fig. 25, the calculations explain the experimental data well.

Gaseous species such as water, nitrogen and carbon show complex dissolution behaviors in molten slags. Gaseous species can be dissolved into molten slags in replacement of both free oxygen ions in the basic slag region and bridged and broken oxygen ions in the acid slag region. The complex dissolution mechanisms of gaseous species have been explained using the hybrid model [111,112], which is an integration of the Blander–Reddy Capacity Model [109] and the Modified Quasichemical Model [17]. For example, water vapor can dissolve in molten slags in form of hydroxyl ions or hydroxyl radicals, depending on the slag basicity. Calculated hydroxyl capacities,

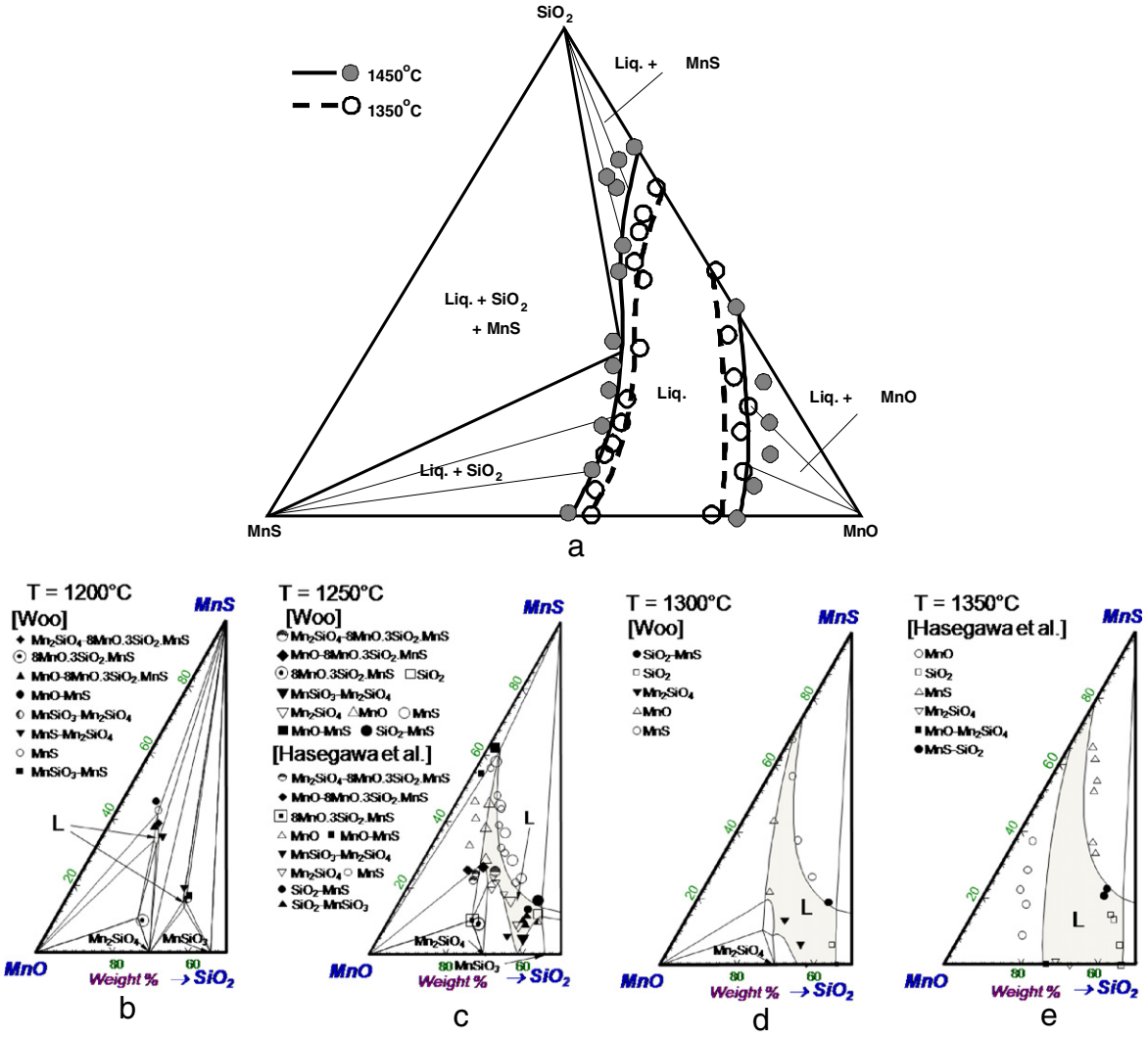

Fig. 12. The calculated phase diagrams of the MnO–SiO_2–MnS oxysulfide system in comparison with experimental data [127,128]. (a) Calculated from CEQCSI [129] and (b)–(d) calculated from the FactSage–FToxid database [53].

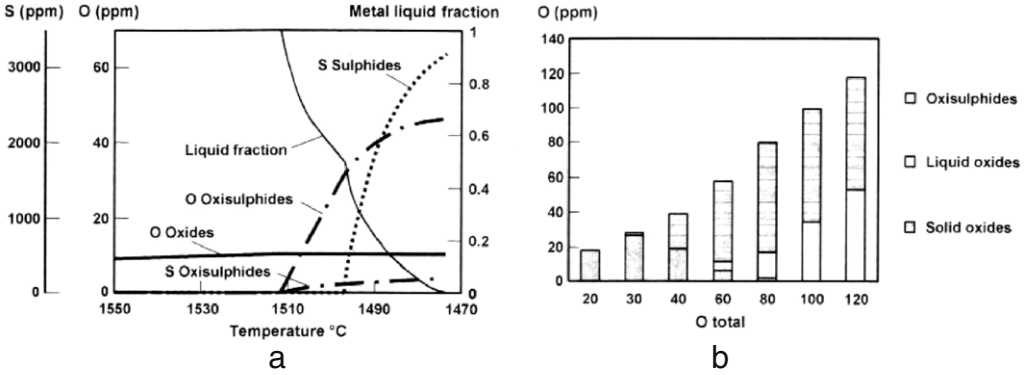

Fig. 13. The distributions of oxygen and sulfur between different inclusion types during solidification of free-cutting steels [129] calculated using CEQCSI. (a) Sequence of equilibrium precipitates in steel Fe–0.07C–1.35Mn–0.014Si–0.35S–0.006O (in wt%) and (b) calculated distribution of oxygen among oxides and oxysulfide inclusions in solidified steels as a function of total oxygen content in steels.

$C_{OH^-} = (wt\%H_2O)_{slag}/(P_{H2O})^{1/2}$ in CaO–SiO_2, MgO–SiO_2 and CaO–MgO–SiO_2 slags are shown in Fig. 26 with experimental data [160, 161]. The solubility minima of water in molten slags are well calculated by the hybrid model. The hydroxyl capacity in the CaO–Al_2O_3–SiO_2–10%MgO slag at 1600 °C is predicted in Fig. 27. The solubilities of water in the CaO–MgO–FeO–Al_2O_3–SiO_2 slags and those of nitrogen and carbon in various slags were modeled by Jung [112].

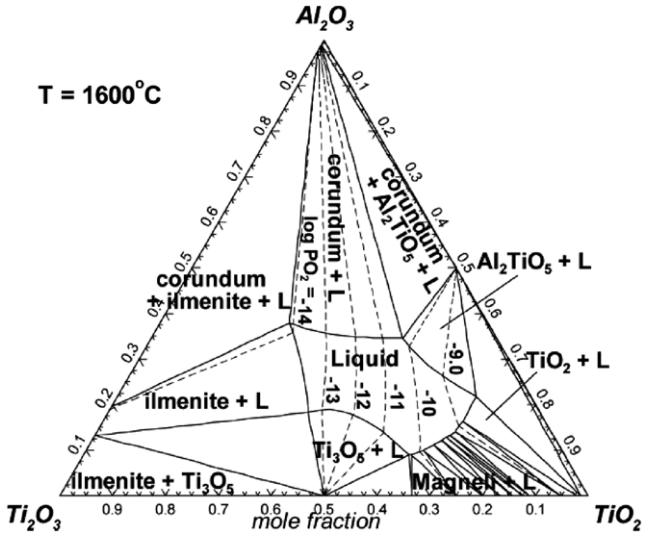

Fig. 14. Predicted phase diagram of the Al_2O_3–TiO_2–Ti_2O_3 system at 1600 °C with oxygen partial pressure isobars (bar) [134].

5.3. Refractories/slag reactions

All furnaces, vessels and nozzles used in contact with liquid Fe and molten slag are all lined with refractories. Refractories must have sufficient thermal and chemical stabilities to withstand attack by liquid Fe, molten slag and even gases. In addition, refractories intended for iron and steel production must have a high resistance to thermal shock caused by abrupt changes in temperature.

5.3.1. Thermal stability of refractories

MgO–C refractories are widely used during primary steelmaking in both basic oxygen and electric arc furnaces owing to their excellent resistance against thermal shock and slag attack, and their low cost. As the wetting behavior between C and molten slag is low, C contained in the refractory can effectively protect it from chemical attack by molten slag. However, the oxidation of C can deteriorate the physico-chemical properties of the refractories. In order to retard C oxidation, so-called antioxidants are added to refractories. In addition to the prediction of the antioxidant behavior at high temperatures, thermodynamic calculations can assist in the selection of proper antioxidants for carbon-containing refractories. Zhang et al. [162] conducted thermodynamic calculations to predict the chemical reactions at high temperatures between MgO–C refractories containing various antioxidants such as Al, Si and B_4C and the atmosphere. Fig. 28 shows the calculated phase changes of a MgO–C brick containing 5 wt% Al or Si at 1500 °C with air/refractory (A/R) ratio. As the refractories react with the atmosphere, various solid oxides, carbides and nitrides and gaseous phases were predicted to form or vanish, which was in good agreement with observed microstructures. Chan et al. [163,164] calculated the thermal behavior of the Al_2O_3–SiO_2–SiC–C bond refractories containing Al, Si, Si_3N_4, BN, B_2O_3 or B_4C under reducing condition and also the chemical reactions between refractories and molten slag. The thermodynamic calculations were in good agreement with experimental results on refractories/slag reactions.

The thermal stabilities of various high alumina-spinel-type and magnesia-chromite-type refractories were calculated by Cho and Jung [165] for application to the lining at the RH bottom vessel. Part of the results are presented in Fig. 29. As seen in the figure, certain commercially available refractories are thermally unstable at about 1650–1700 °C and, therefore, cannot be candidates for high-temperature applications in RH or VOD vessels. In certain cases, a very small amount of CaO and SiO_2 can induce partial melting of refractories even below 1600 °C. In addition, a significant change in the refractory phases with temperature may result in large volume variations, which can subsequently cause thermal stresses in refractories and refractory wear.

5.3.2. Slag/refractories reactions

In order to understand the complex chemical reactions between molten slags and refractories, phase diagram information is indispensable [166–168]. However, phase diagrams for specific 'molten slag–refractory' systems are unavailable in many cases. Thermodynamic database can be used to calculate any phase diagram sections within the accuracy of the database. FactSage and MTDATA have been frequently used for this purpose [169–183].

The complex chemical reactions between magnesia-chromite refractories and CaO–SiO_2–Al_2O_3 slags in the VOD stainless steelmaking process were calculated by Jung et al. [169]. According to the calculation results, magnesia-chromite spinel refractories with overall composition 58MgO–6.5Al_2O_3–21Cr_2O_3–13.5FeO (in wt%) consist of periclase and spinel phases at 1650 °C under reducing conditions (in contact with liquid steel): 73wt% periclase (composition: 72.8MgO–0.6Al_2O_3–9.1Cr_2O_3–17.5FeO in wt%) and 27wt% spinel (composition: 21.5MgO–22.5Al_2O_3–53.4Cr_2O_3–2.6FeO in wt%). Fig. 30 shows a thermodynamic simulation of the refractory corrosion by a 50CaO–40SiO_2–10Al_2O_3 (in wt%) slag at 1650 °C. In the calculations, x grams of slag and $(1 - x)$ grams of refractory were assumed to be completely equilibrated in order to simulate corrosion with slag penetration into the refractory. That is, the calculation assumes that the diffusion rates of all oxide elements in molten slag are the same and that the amount of penetrated slag varies linearly with the depth of penetration. The resultant equilibrium amounts of all phases and their compositions are plotted versus x in Fig. 30. The periclase phase is more severely corroded compared to the spinel phase. Various silicate phases such as Ca_2SiO_4, merwinite and monticellite (olivine) observed in reacted refractories can form during cooling of the penetrated slag. When the refractory and slag compositions are changed, different corrosion reactions can be calculated.

A similar approach was used by Goto et al. [170] to simulate the corrosion of MgO–$MgAl_2O_4$ spinel refractory bricks by calcium aluminosilicate slags at about 1450 °C. The mineralogy of refractories revealed the formation of secondary spinel, monticellite and merwinite phases with the slag penetration depth, which was well explained by thermodynamic calculations using the FACT oxide database [22]. The corrosion of high-alumina refractories by ladle slag was calculated and compared with experimental microstructures by Melcher et al. [171]. In order to understand the degradation of MgO refractories by CaO–SiO_2–MgO–Al_2O_3–FeO slags, Nightingale et al. [172] calculated the phase diagram of the MgO–molten slag system using MTDATA [64]. The degradation mechanism was well explained by the calculated phase diagram. Reiter et al. [173] performed thermochemical calculations for various refractories with EAF slags at controlled oxygen partial pressure to prescreen the suitable refractories for the EAF process. Park [174] and Kaiser et al. [175] also conducted thermodynamic calculations to understand the degradation of a zirconia ceramic nozzle by mould flux.

Van Ende et al. [178] performed an experimental study on the degradation of MgO–C refractories by CaO–SiO_2–MgO–MnO–Al_2O_3–Cr_2O_3 stainless steel slags at 1600 °C and compared the experimental results with thermodynamic calculations performed with FactSage. According to the experimental results, the refractory degradation was highly dependent on the basicity and MnO content of the slag. As can be seen in Fig. 31, the thermodynamic calculations using FactSage [22] can predict the final slag

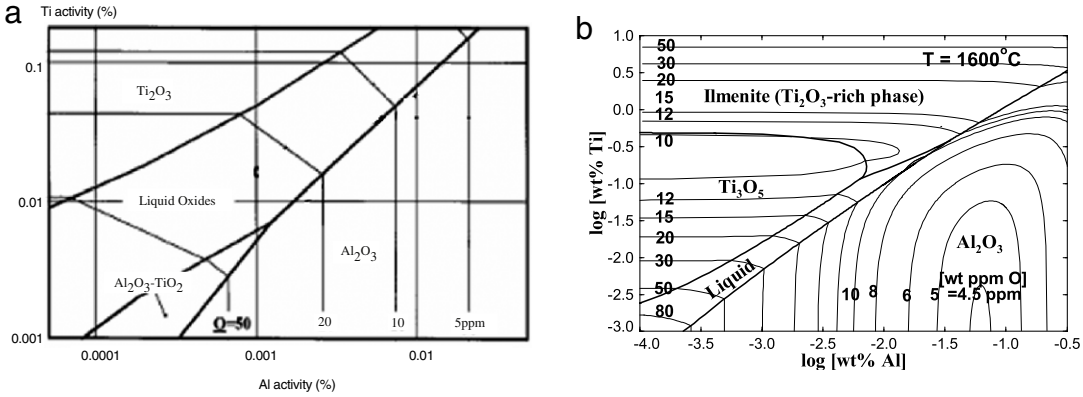

Fig. 15. Inclusion diagram of the Fe–Al–Ti–O system at 1600 °C, calculated using CEQCSI [130] and the FactSage–FToxid/FTmisc database [134]. Axes indicate the amounts of Ti and Al dissolved in the liquid steel. Stable inclusion phases are labeled, and iso-oxygen content lines in the liquid Fe are also plotted.

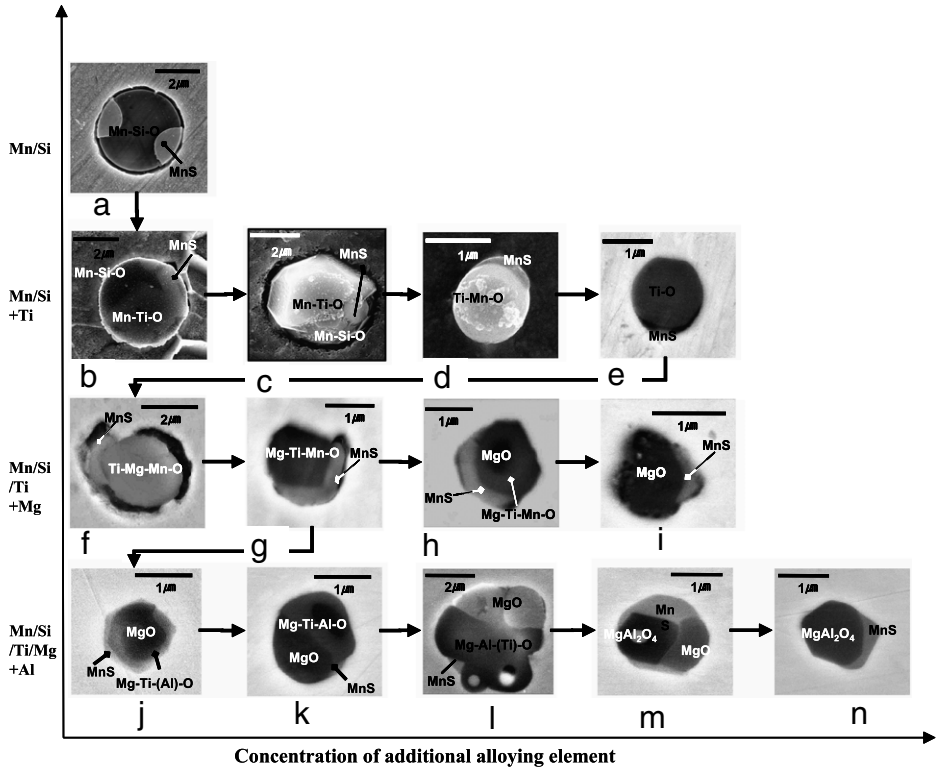

Fig. 16. Change of morphology and chemistry of typical inclusions found in Fe–C–Mn–Si–O–S–N (in wt%) steel with additions of Ti, Mg, and Al [137–146].

compositions well and assist in the interpretation of the degradation mechanisms.

Beskow et al. [179–181] and Son et al. [182] investigated the so-called ladle glaze, which is a solidified slag film formed on ladle refractories during the discharge of the steel in ladle. They reported that liquid slags can react with ladle refractories even within 2 min, resulting in the degradation of the refractory linings and eventually the contamination of molten steel with non-metallic inclusions. The chemical reactions between ladle refractories (MgO–C and high-alumina magnesia) and top slags can be readily understood using thermodynamic calculations.

Fox et al. [183] performed Confocal Scanning Laser Microscope (CSLM) experiments to observe the dissolution behavior of ZrO_2, Al_2O_3, MgO and $MgAl_2O_4$ particles in fluoride-free mould flux ($CaO–SiO_2–Na_2O–MgO–Al_2O_3–B_2O_3$). As can be seen in Fig. 32, they computed the phase diagram of the 'ZrO_2–mould flux' system using MTDATA in order to understand the dissolution mechanism of ZrO_2. The calculation result shows that ZrO_2, a common submerged entry nozzle (SEN) material, can directly dissolve into the mould flux at 1500 °C without producing any protective layer, which was confirmed by CSLM experiments. This means that ZrO_2 is not the optimum SEN material for the fluoride-free mould flux from the chemical corrosion viewpoint.

5.4. Slag/inclusion reactions

As the density of non-metallic inclusions is less than that of molten steel, inclusions move naturally in molten steel towards the top slag. However, if the inclusions are not captured or dissolved quickly enough by the molten slag, they can bounce back into the molten steel. Although phase diagram information is crucial for studying the dissolution of non-metallic inclusions in molten slag, the exact phase diagram sections for 'inclusion–slag' systems are frequently unavailable. FactSage and MTDATA have been used for the phase diagram calculations. Recently, the CSLM technique has

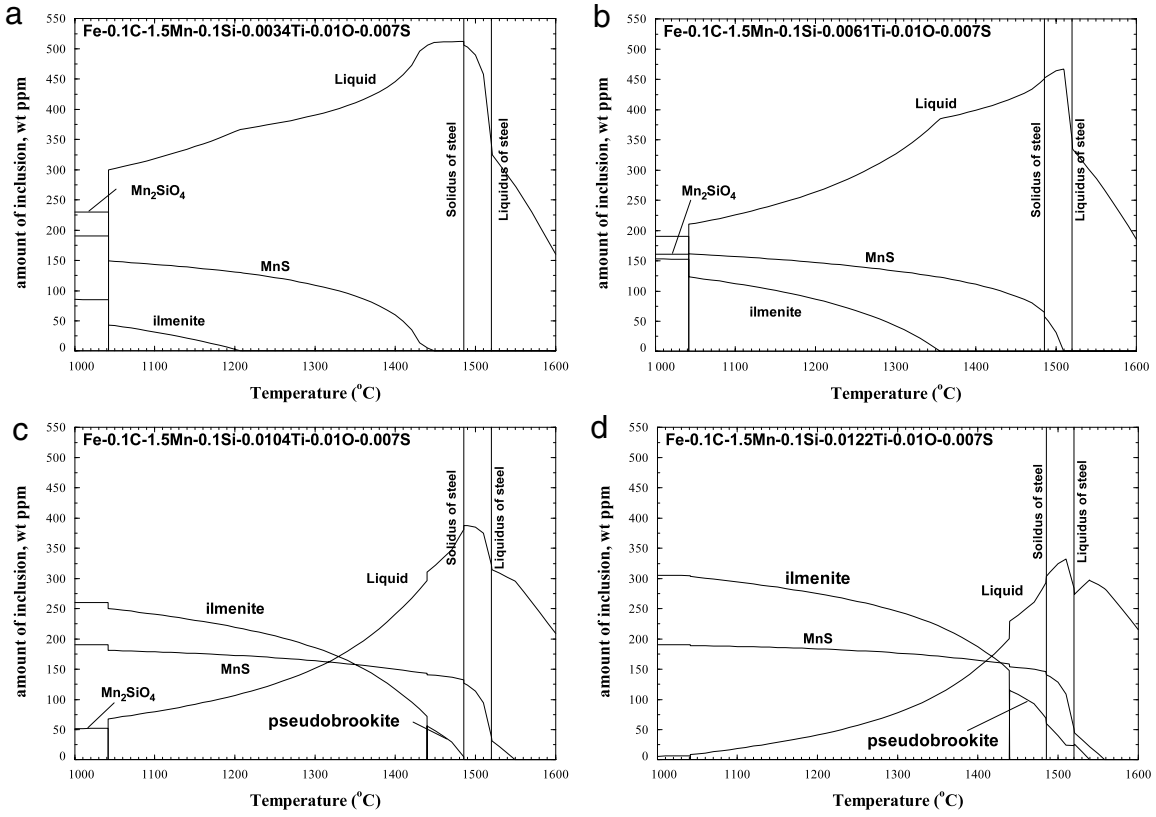

Fig. 17. Evolution of inclusions in Fe–0.1C–1.5Mn–0.1Si–0.01O–0.007S (in wt%) steel with addition of Ti during solidification, calculated from thermodynamic databases [140]. (a) 34 ppm Ti, (b) 61 ppm Ti, (c) 104 ppm Ti and (d) 122 ppm Ti.

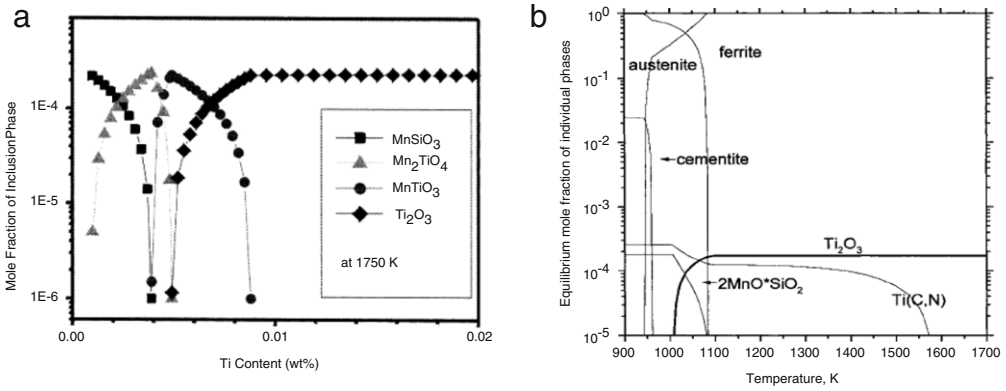

Fig. 18. The evolution of oxide inclusions in high-strength steels [142,144]. Evolutions of inclusions (a) with increasing Ti content in Fe–0.08C–1.7Mn–0.2Si–0.004O–0.001N (in wt%) at 1477 °C, and (b) with temperature in Fe–0.14C–1.84Mn–0.18Si–0.011Ti–0.003O–0.001N (in wt%) steel.

been used for the *in situ* observation of inclusion dissolution into molten slag.

Park et al. [184] performed inclusion dissolution experiments employing the CSLM technique and they explained the mechanism of MgO dissolution into molten $CaO–Al_2O_3–SiO_2$ slags using the phase diagram. They calculated the quaternary phase diagram section of $(CaO)_{0.525}(SiO_2)_{0.475}–Al_2O_3–MgO$ at 1550 °C, which represents the dissolution of MgO into various ternary $CaO–Al_2O_3–SiO_2$ slags with fixed CaO/SiO_2 basicity. The scanned compositional trajectories from molten $CaO–Al_2O_3–SiO_2$ slags to MgO inclusion are plotted in the calculated phase diagram in Fig. 33. The monotonous dissolution of MgO into M21 and M22 slags and the formation of an abnormal $MgAl_2O_4$ ring-like structure around MgO in M23 and M24 slags can be simply explained based on the computed phase diagram. A similar thermodynamic calculation approach has been used by several researchers [185–187] to understand the dissolution of non-metallic inclusions into molten slags.

5.5. Solidification behavior of molten slag and mould flux

BF, BOF and secondary steelmaking slags can be recycled to produce cements, road-construction materials and even steelmaking slag after proper treatments. In order to be suitable for recycling, the solidified slag products must have certain mechanical, physical and chemical properties, which are directly related to the slag mineralogy. The mineralogy of solid slags is determined by the chemistry and the solidification process of slags.

Durinck et al. [188] performed solidification experiments of $CaO–MgO–SiO_2$ slags and compared the results with Scheil solidification calculations. As can be seen in Fig. 34, the observed mineralogy of the solidified slags is quite different from that calculated by

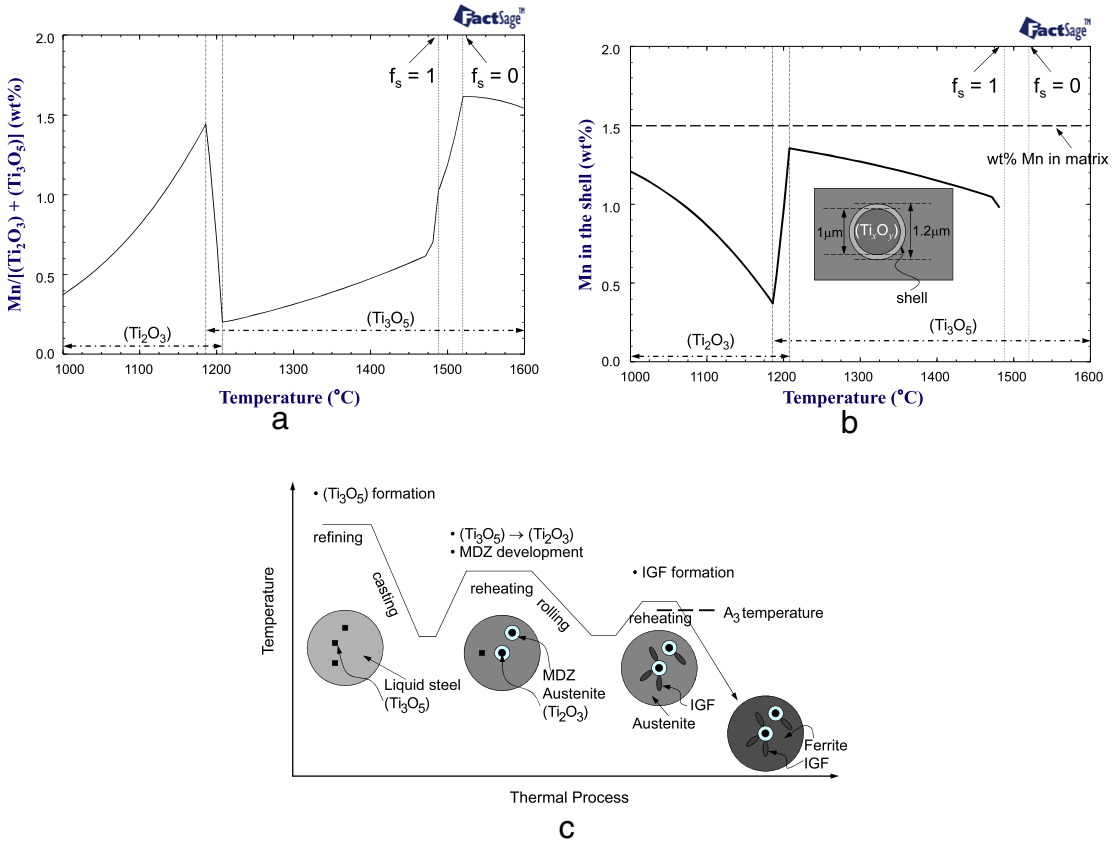

Fig. 19. Calculated Mn concentrations (a) in TiO_x inclusions and (b) in a shell around the TiO_x inclusion in equilibrium with Fe–0.1C–1.5Mn–0.1Si–0.007S–0.005O–0.015Ti (in wt%), and (c) proposed optimum thermal process in order to maximize IGF development associated with MDZs [141].

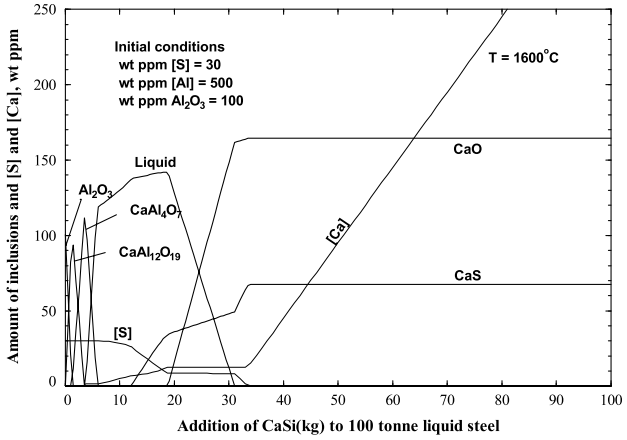

Fig. 20. Modification of Al_2O_3 inclusions and variation of total dissolved [Ca] and [S] contents in steel with CaSi (molar ratio Ca/Si = 1) injection into 100 tons of Al deoxidized liquid steel containing sulfur at 1600 °C [123]. Initial steel contains [S] = 30 ppm, [Al] = 500 ppm and Al_2O_3 = 100 ppm.

a traditional equilibrium model but reasonably close to the Scheil solidification calculation results, which shows that the Scheil solidification model is more suitable for predicting the solidification behaviors of molten slags. The same approach has been used to explain the solidification behavior of $CaO–SiO_2–MgO–Al_2O_3–CaF_2$ slags [189] and $CaO–SiO_2–CrO_x$ slags with controlled oxygen partial pressure [190].

The solidification behavior of mould flux is very important in the continuous casting of steel. The mould flux has two important functions, lubrication and heat transfer control between the water-cooled Cu mould and steel, which are mainly determined by the chemistry and the solidification behavior of the mould flux. The chemistry and phase diagrams of mould flux systems containing a considerable amount of fluorides are still seldom investigated due to the complexity of the system and the difficulty to perform experiments. Thermodynamic modeling of mould flux containing fluorides, Na_2O and Li_2O is quite challenging. Recently, Jung [54] presented a preliminary thermodynamic model of the $CaO–Al_2O_3–SiO_2–MgO–F$ system using the two-sublattice Modified Quasichemical Model for the liquid phase. The database can be used for mould flux systems containing more than 50 mole % of fluorides. Fig. 35 shows the predicted phase diagrams for the $CaO–SiO_2–CaF_2$ system with 10 wt% Al_2O_3 at 1200 and 1400 °C. As seen in the figures, a large liquid region is predicted with the addition of CaF_2, even at 1200 °C. The calculated solidification behavior of the $30CaO–10Al_2O_3–40SiO_2–20CaF_2$ (in wt%) flux is presented in Fig. 36. According to the calculations, cuspidine ($Ca_4Si_2Fe_2O_7$) is the primary phase and more than 50 wt% of liquid phase exists even at 1100 °C. The final solidification can occur below 1000 °C.

5.6. Process modeling coupled with computational fluid dynamics (CFD) models

With the progress of thermodynamic databases and the availability of faster and more powerful computing system, coupling fluid flow simulations and thermodynamic databases is becoming more frequent. Commercial computational thermodynamic software packages such as FactSage, MTDATA and Thermo-Calc provide a special module that can be adopted by computational fluid dynamics (CFD) or numerical simulation codes to calculate thermodynamic equilibration in conjunction with numerical calculations.

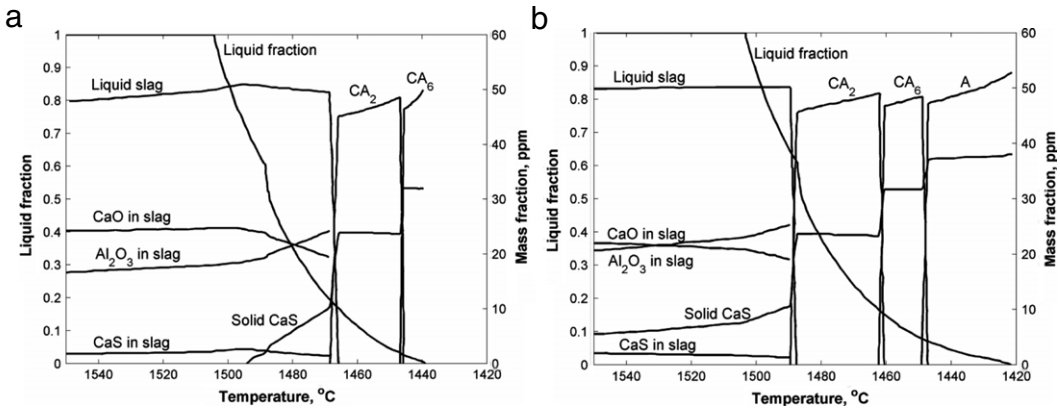

Fig. 21. Evolution of Ca treated inclusion during solidification of steels containing (a) O = 20 mass ppm and S = 50 mass ppm, and (b) O = 20 mass ppm and S = 250 mass ppm. [148].

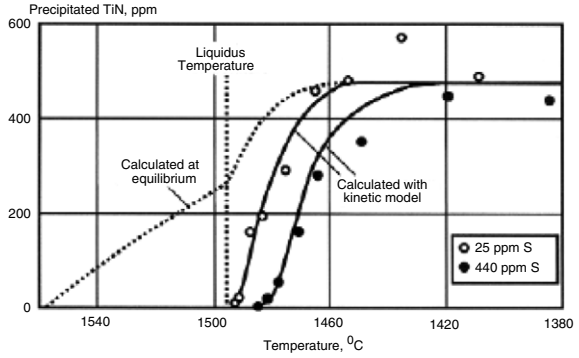

Fig. 22. Effect of sulfur content on the precipitation of TiN during the steel solidification, calculated using both equilibrium precipitation and the kinetic model developed by the CEQCSI group [106].

Simonnet et al. [191] performed RH process simulations by coupling the Fluent CFD code and CEQCSI. They simulated the circulation of molten steel in the RH vessel and ladle, and the influence of Al addition on steel cleanliness. Hydrodynamic computations for liquid steel during the RH process were performed with Fluent, in order to determine the temperature distribution in the vessel. At each time step, the transport of all dissolved chemical elements and of all non-metallic inclusions in liquid steel was also computed. CEQCSI computes the equilibrium state for each cell used in the CFD model. This calculation gave the evolution of the dissolved element concentrations in liquid steel and the evolution of the inclusion composition and population. Fig. 37 shows the calculated [Al] and [O] contents and the amount of solid Al_2O_3 inclusions with RH operation time. In the calculations, 178 kg of Al metal was injected during 10 s into 300 tons of molten steel containing 0.2Mn–0.02Si–0.03O. Recently, Gardin et al. [192] continued the calculations to investigate the distributions of Al, O and Al_2O_3 in the RH bottom vessel and ladle during the RH process. The recent advances in the coupled model development by the CEQCSI group can be found elsewhere [59].

Jonsson et al. [193] and Andersson et al. [194] performed simulations combining CFD modeling with thermodynamic calculations for molten steel during Ar bubbling in the ladle. As seen in Fig. 38, the evolution of the sulfur distribution between the molten steel and the top slag was calculated with bottom Ar gas stirring time. The calculated sulfur concentrations in molten steel are compared with plant data in Fig. 38(c). Hassall et al. [195] combined CFD and thermodynamic modeling to investigate the inclusion formation mechanism during tapping, alloy addition, and Ar stirring in the ladle. Recently, Ersson et al. [196] coupled the CFD model with thermodynamic calculations based on Thermo-Calc to analyze the top blown converter involving metal/gas/slag equilibria.

5.7. Physical property models for molten slag

5.7.1. Viscosity

Viscosity is one of the most important physical properties of molten slags in steelmaking. The viscosity of silicate melts is particularly complex and difficult to model due to the complex composition-dependent structure of silicate melts. The measurement of the viscosities of silicate melts is also very difficult, as was well illustrated by the recent "Round Robin Project" led by Mills et al. [197], which showed that viscosities of the same samples as measured by various groups in the world can easily differ by 20%, and often even by 50%, due to various sources of error such as incorrect calibration, interaction with containers and bobs, volatilization and interaction with the atmosphere.

Although the viscosity of slag is important in the steelmaking process, modeling the viscosity of silicate melts is particularly challenging as it increases by ten orders of magnitude with increasing SiO_2 content at constant temperature.

The temperature dependence of the liquid oxide viscosity at fixed composition can be described by the Arrhenius function:

$$\eta = A\exp(E/RT) \tag{46}$$

where A is the pre-exponential term and E the activation energy of viscous flow. In some cases, the pre-exponential term A is described by a temperature-dependent term, $A'T$.

Urbain [198] proposed a semi-empirical equation for the viscosity of multicomponent slag in which the activation energy varies with the composition of three categorized components in the slag: glass formers, modifier and amphoterics. However, the accuracy of calculation was quite low even just outside the assessed composition area. Lida et al. [199] modified Urbain's model using a so-called modified basicity index to describe the viscosity of multicomponent mold flux and slag (in particular, it is good for low-viscosity liquid). Du Sichen and Seetharaman [200–202] proposed a simple structural viscosity model in which the activation energy is calculated as a function of the interaction energies between simplified structural units in the molten slag. The model can readily explain the viscosity of multicomponent silicate slag, but has a limitation in describing the viscosity of aluminosilicate melts, which results from using oversimplified structural units in the model.

Recently, many studies [114–116,119–121,203–205] have been performed to develop structural viscosity models for multicomponent metallurgical slags based on the structural information

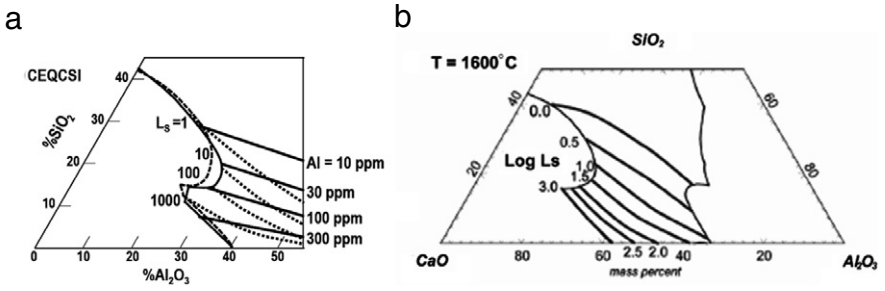

Fig. 23. Sulfur distribution ($L_S = (wt\%S)_{slag}/[wt\%S]_{steel}$) for a CaO–$SiO_2$–$Al_2O_3$ slag at 1600 °C in equilibrium with the Fe–0.1C–0.7Mn–0.1Si–0.05Al–0.0005O–0.003S (wt%) steel, calculated with (a) CEQCSI [150] and (b) FactSage [151].

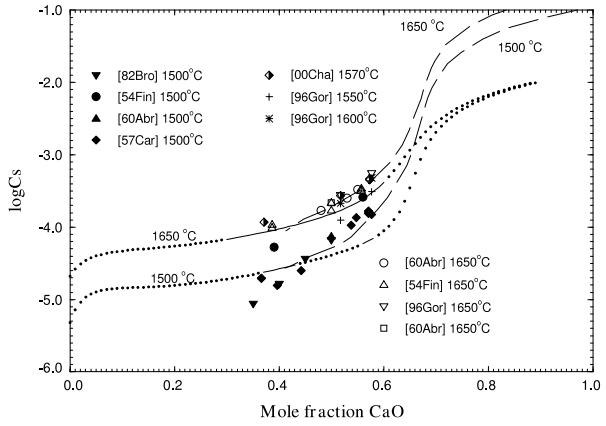

Fig. 24. Calculated sulfide capacities for the binary CaO–SiO_2 slags from FactSage [53] (solid and dotted lines) and MTDATA [67] (dashed lines) in comparison with experimental data [152–158].

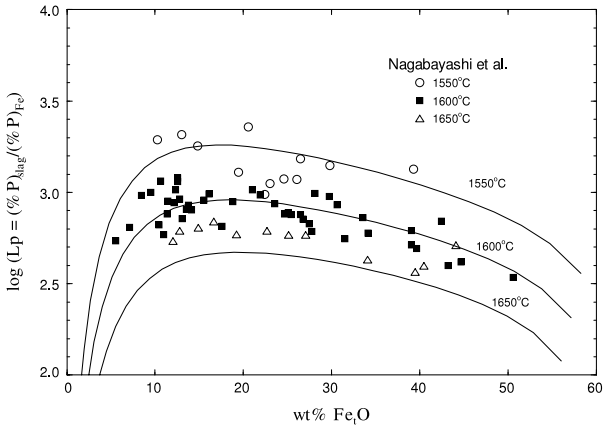

Fig. 25. The calculated phosphorus distribution ($L_P = (wt\%P)_{slag}/[wt\%P]_{steel}$) between the CaO-saturated CaO–Fe_tO–P_2O_5 slag and molten Fe–P steel [151] in comparison with experimental results [159].

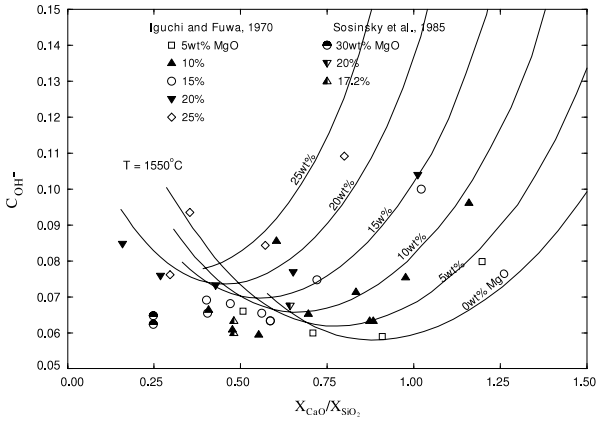

Fig. 26. Calculated water solubilities in CaO–MgO–SiO_2 slags at 1550 °C using the FactSage FToxid database [112] along with experimental data [160,161].

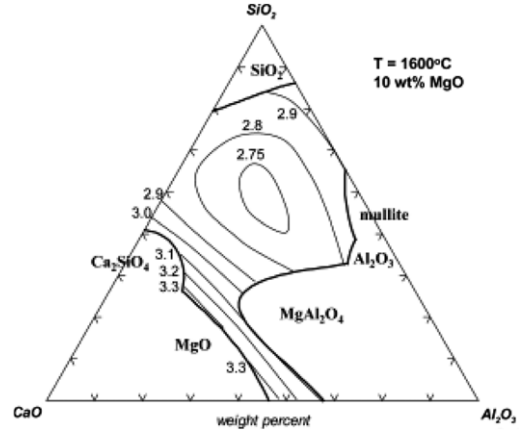

Fig. 27. Predicted iso-capacity lines of water for CaO–Al_2O_3–SiO_2–10 wt% MgO at 1600 °C [112]. Values are log ($C_{OH^-} \times 10^4$).

extracted from sophisticated thermodynamic models. Thermodynamic models which are constructed based on the molten slag structure, such as the Modified Quasichemical Model [16,17] or the Cell Model [55], can allow the calculation, from the optimized thermodynamic model parameters, of the silicate melt structure as a function of composition and temperature. For example, as seen in Fig. 39, the amounts of free oxygen, broken oxygen and bridged oxygen calculated from the Modified Quasichemical Model are in good agreement with the experimental data of Park and Rhee [206]. The calculated amounts of broken oxygen for various binary silicate systems are also quite reasonable from the viewpoint of the optical basicity. The same structural information can be calculated from the Cell Model. In the structural viscosity model, both *A* and *E* are model parameters, which can be expressed as functions of the concentrations of the structural units.

Zhang and Jahanshahi [119–121] correlated the activation energy, *E*, to the concentrations of bridged, broken and free oxygens in a silicate melt calculated from the Cell Model parameters stored in the MPE liquid oxide database. To obtain a better fit of the viscosity data, the model uses the square and the cube of the bridged oxygen concentration, multiplied by optimized viscosity parameters. It should be noted that their model for aluminosilicate systems considers the amphoteric behavior of Al_2O_3 using the so-called charge-compensation concept. The viscosity database of Zhang and Jahanshahi includes SiO_2, CaO,

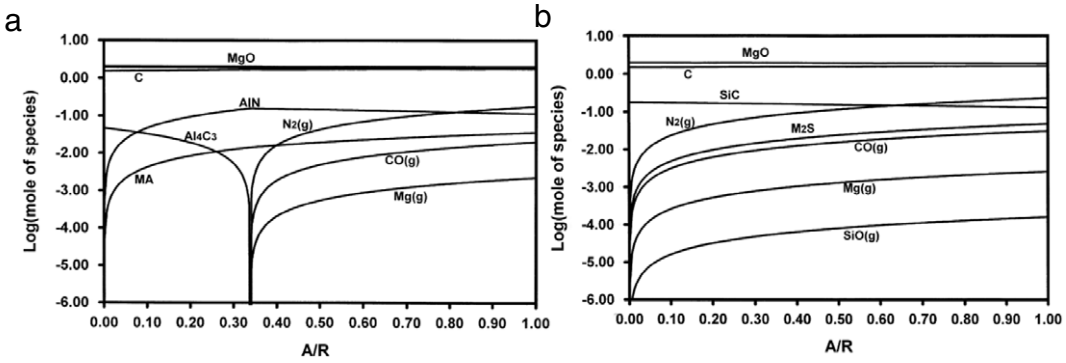

Fig. 28. Calculated phase changes in MgO–C refractory brick containing antioxidants (a) 5 wt% Al and (b) 5 wt% Si at 1500 °C [163]. A/R represents the atmosphere/refractories ratio, where the atmosphere is 35%CO + 65%N_2, and the refractories are composed of 40 wt% fused MgO, 40 wt% sintered MgO and 20 wt% graphite.

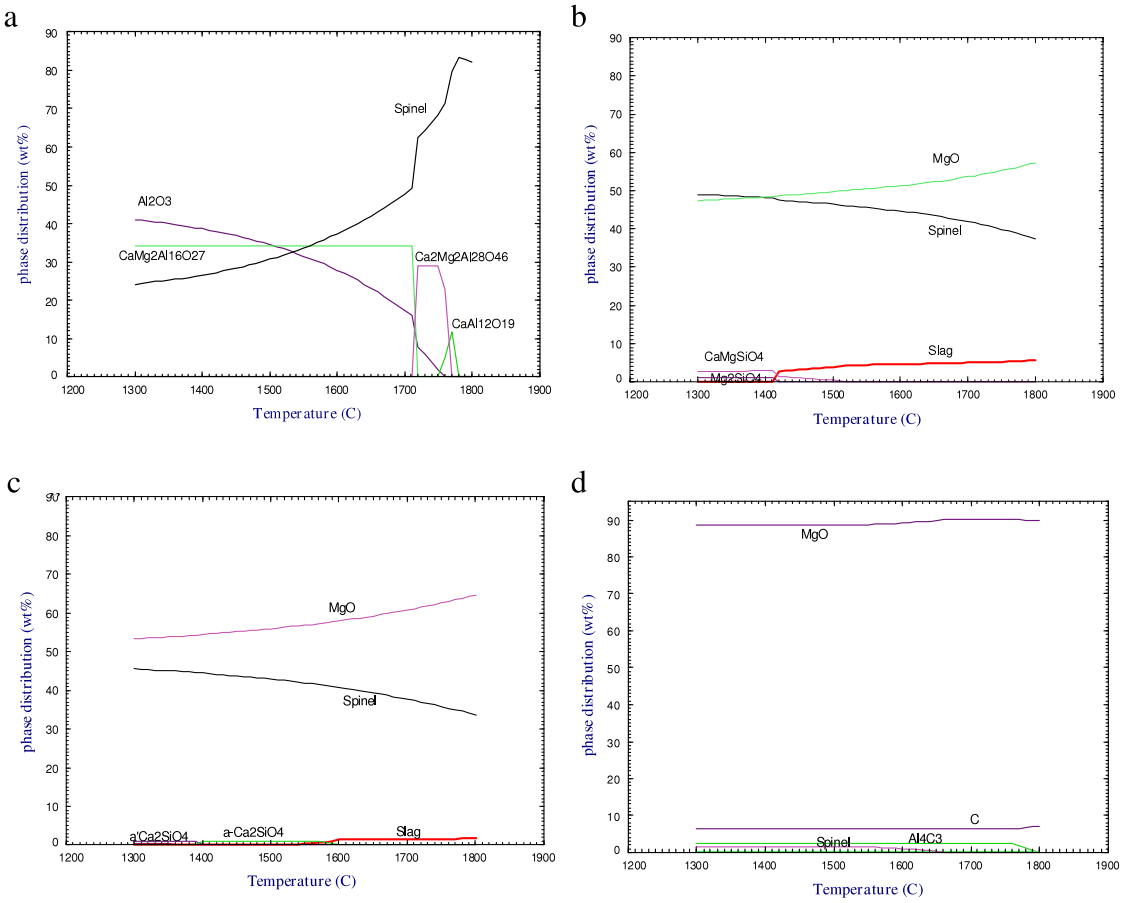

Fig. 29. Calculated thermal stability of various refractories [165]. (a) 88Al_2O_3–9MgO–3CaO, (b) 11Al_2O_3–58MgO–0.9CaO–20Cr_2O_3–8.8Fe_2O_3–1.6SiO_2, (c) 4Al_2O_3–61MgO–0.7CaO–29Cr_2O_3–4.8Fe_2O_3–0.4SiO_2 and (d) 0.5Al_2O_3–89MgO–0.5SiO_2–7C in wt%.

MgO, FeO, Fe_2O_3, Al_2O_3, MnO, Ti_2O_3, TiO_2, PbO, NiO, CoO, ZnO and Cu_2O. Unfortunately, the viscosities of binary MeO–Al_2O_3 (Me = divalent cation such as Ca, Mg, Mn, Fe, …) were somewhat compromised to describe ternary and multicomponent aluminosilicate systems more accurately. Fig. 40 shows the calculated iso-viscosity curves of the CaO–Al_2O_3–SiO_2 system at 1900 °C.

Nakamoto et al. [205] developed a model using the concentrations of bridged, non-bridged and free oxygen, which were calculated from the Cell Model [55]. Their model was based on the idea that viscous flow is caused by the motion of "cutting off" points, defined as the sum of broken and free oxygen through the network structure. The model was used to describe the viscosity of many ternary aluminosilicate systems containing CaO, MgO, FeO, Na_2O and K_2O. Although this model requires very few parameters, the agreement between calculated viscosities and experimental data is unsatisfactory. Kondratiev and Jak [203] and Jak [204] developed a viscosity model where the activation energy E is expressed as a complex function of bridged, non-bridged and free oxygen concentrations calculated from the Modified Quasichemical Model [16,17]. In order to reproduce the experimental viscosity data for the CaO–Al_2O_3–SiO_2–FeO–MgO–K_2O–Na_2O system, however, their model requires quite a large number of binary and ternary parameters.

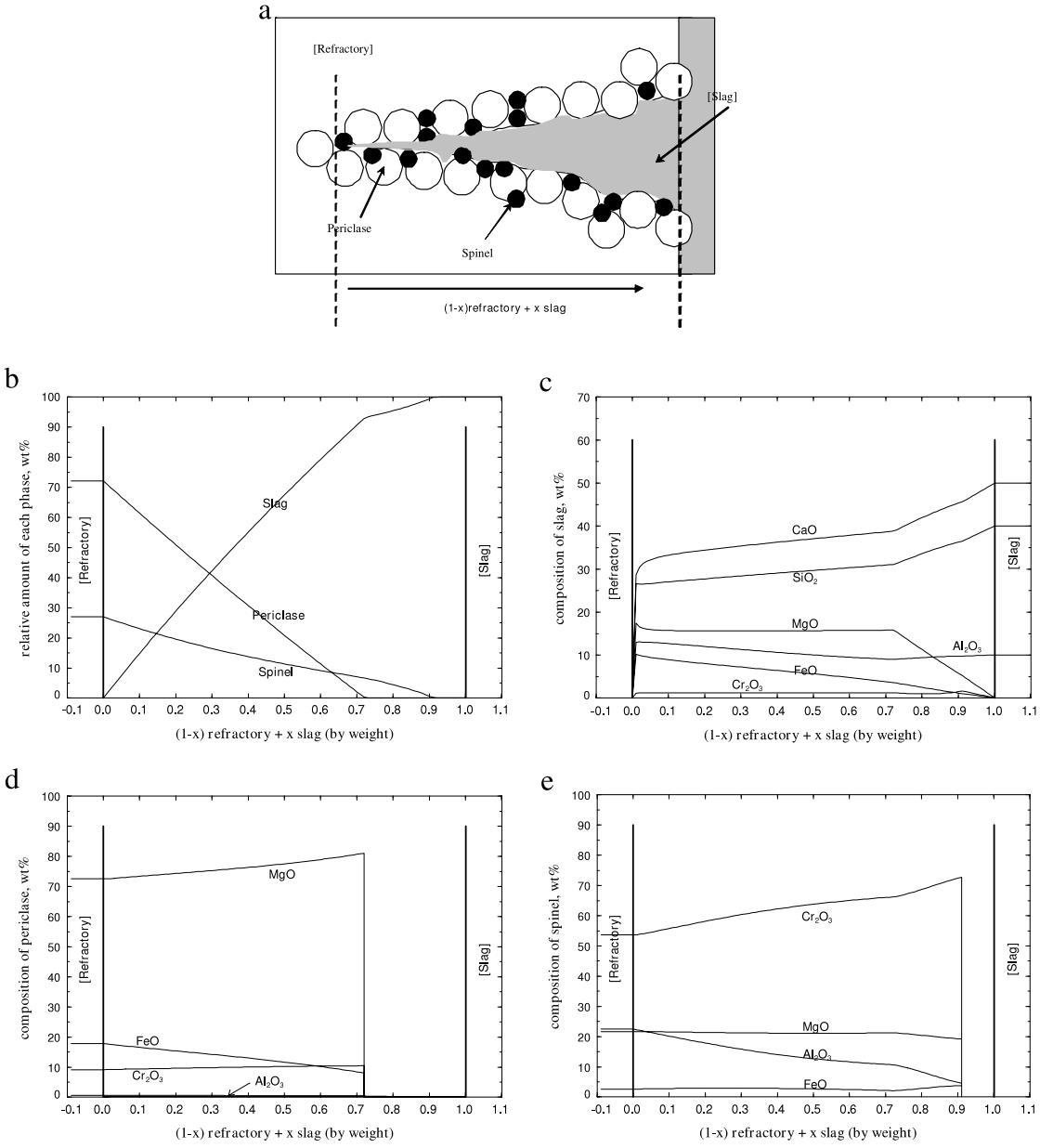

Fig. 30. Simulation of slag penetration into refractories for the VOD in stainless steelmaking [169]. Initial compositions: refractories: 58MgO–6.5Al_2O_3–21Cr_2O_3–13.5FeO and slag: 50CaO–40SiO_2–10Al_2O_3 in wt%. (a) Schematic of slag penetration, (b) relative amounts of slag, periclase and spinel phases with slag penetration, and their composition of (c) slag, (d) periclase and (e) spinel.

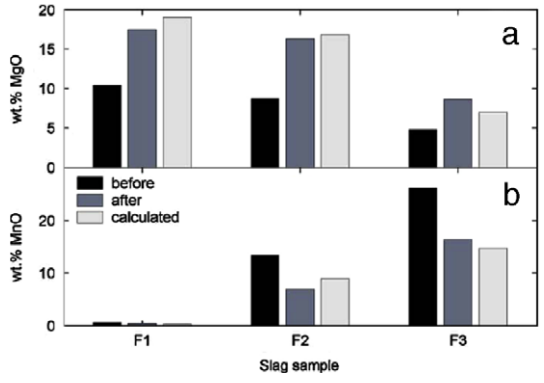

Fig. 31. The comparison of observed concentrations of (a) MgO and (b) MnO in molten slags after reaction with MgO–C refractory with thermodynamic calculations [178]. F1, F2 and F3 represent different slags used in the experiments.

Recently, Grundy et al. [114–116] developed a structural viscosity model based on the structural unit calculations from the Modified Quasichemical Model parameters optimized for the FACT oxide database [22] for silicate melts. The steep increase in viscosity at high SiO_2 contents is modeled by the formation of a structural unit containing 40 interconnected second-nearest-neighbor Si–O–Si pairs (i.e. bridged oxygen). In the case of ternary or multicomponent silicate melts without Al_2O_3, the structural model can predict viscosities very accurately, in good agreement with experimental data, using only binary model parameters without any additional ternary model parameters. It should be noted that the structural units calculated in a given ternary or multicomponent system already reflect the structural changes due to the chemical interactions between the components in the system. The viscosities of aluminosilicate slags show maximum peaks near the compositions where Σ (basic

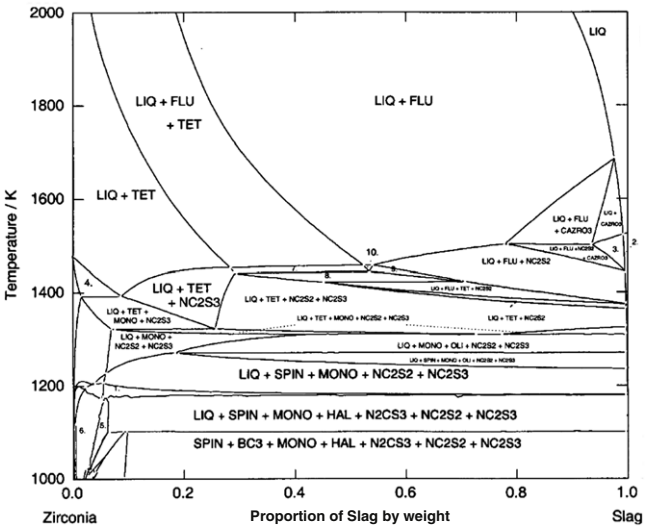

Fig. 32. Calculated phase diagram of the 'ZrO$_2$–slag' system [183]. The composition of the slag is 20CaO–9Al$_2$O$_3$–40SiO$_2$–9MgO–20Na$_2$O–0.5Li$_2$O–1.5B$_2$O$_3$ in wt%. FLU, TET and LIQ represent cubic ZrO$_2$ solution, tetragonal ZrO$_2$ solution and liquid, respectively.

oxide components)/Al$_2$O$_3$ $\approx$ 1.0 (molar ratio). This is modeled by one additional temperature-independent model parameter for the formation of an associated M$_{0.5}$AlO$_2$ or NAlO$_2$ structural unit for each MO–Al$_2$O$_3$–SiO$_2$ or N$_2$O–Al$_2$O$_3$–SiO$_2$ ternary system, where MO and N$_2$O are basic oxides. This is similar to the charge-compensation concept adopted in Zhang and Jahanshahi's model [121]. This additional model parameter is sufficient to describe the viscosity behavior of a given ternary system with good precision. Fig. 41 shows the calculated viscosities of CaO–Al$_2$O$_3$–SiO$_2$ and Na$_2$O–SiO$_2$–Al$_2$O$_3$ systems along with experimental data [207–217]. The viscosity database includes SiO$_2$, CaO, MgO, Na$_2$O, K$_2$O, Al$_2$O$_3$. FeO, Fe$_2$O$_3$, MnO, NiO, CoO, PbO, ZnO, TiO$_2$, Ti$_2$O$_3$ and CaF$_2$.

5.7.2. Surface tension

In order to couple the thermodynamic database with CFD modeling, the interfacial (surface) tensions between slag, molten steel, refractory and gases are of great importance. Tanaka et al. [218] successfully calculated the surface tensions of molten salts and metals by linking the modified Butler equation [219] and the thermodynamic database. Several studies [220–223] have been performed to calculate the surface tension of binary, ternary and multicomponent slags with the introduction of additional adjustable physical parameters such as the ionic radii of cations. However, no large database to properly calculate the surface tension of molten slag is available yet.

6. Future work

6.1. Thermodynamic database

Although the current thermodynamic databases for oxides, oxysulfides, oxyfluorides, and steel can already cover a wide range of steelmaking operations and applications, the thermodynamic databases constantly need to be improved with the advances in the steelmaking process and the development of new steel grades.

In order to optimize the conventional mould flux, an accurate database for the CaO–Al$_2$O$_3$–SiO$_2$–MgO–Na$_2$O–Li$_2$O–F system is necessary. The database for the CaO–Al$_2$O$_3$–SiO$_2$–MgO–Na$_2$O–Li$_2$O–B$_2$O$_3$ system can be very helpful for designing new F-free mould flux and refining slags. The CaO–FeO–Fe$_2$O$_3$–SiO$_2$–MgO–P$_2$O$_5$ system is of importance in understanding the behavior of BOF slag. The oxide metallurgy research for the active usage of non-metallic inclusions as a nucleation site for acicular ferrite or pinning actuator of grain growth requires accurate thermodynamic databases for oxysulfide systems containing rare-earth components and the corresponding liquid steel database. This is also important for the development of new free-cutting steels, high-alloyed steels and advanced high-strength steels, and for steel welding research. Oxide databases containing Ti oxide and V oxide should be improved. Recent research on the reduction of iron oxides by hydrogen gas to replace the conventional reduction

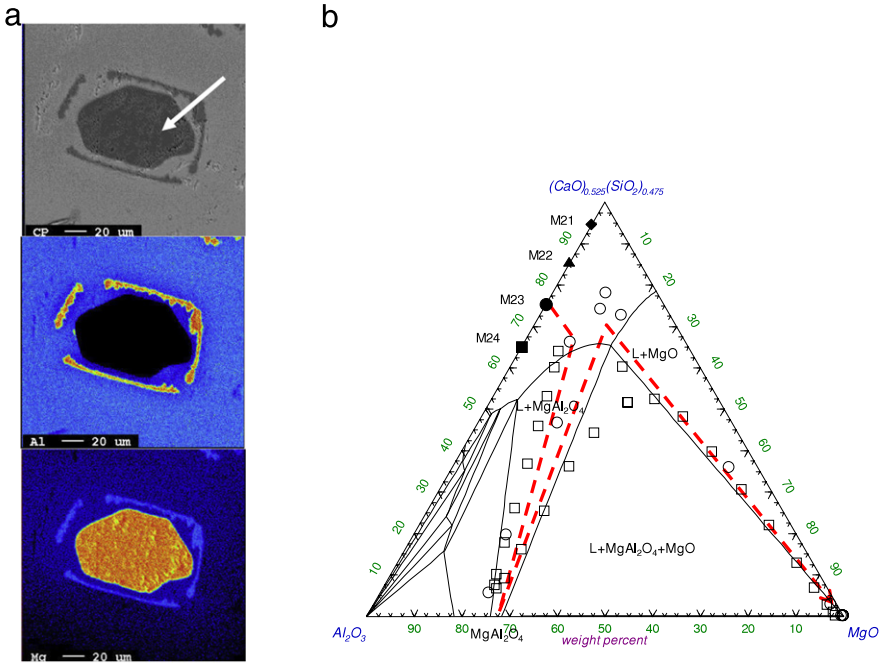

Fig. 33. Calculated phase diagram of 'MgO inclusion–slag' system at 1550 °C [184]. M21–M24 in the diagram represent different slag compositions used in the experiments. The results of the line-scanned composition in (a) for M23 slag are plotted in (b). The liquid composition between the original MgO inclusion and surrounding MgAl$_2$O$_4$ layer is corresponding to the liquid composition co-saturated with MgO and MgAl$_2$O$_4$ in the calculated diagram (b).

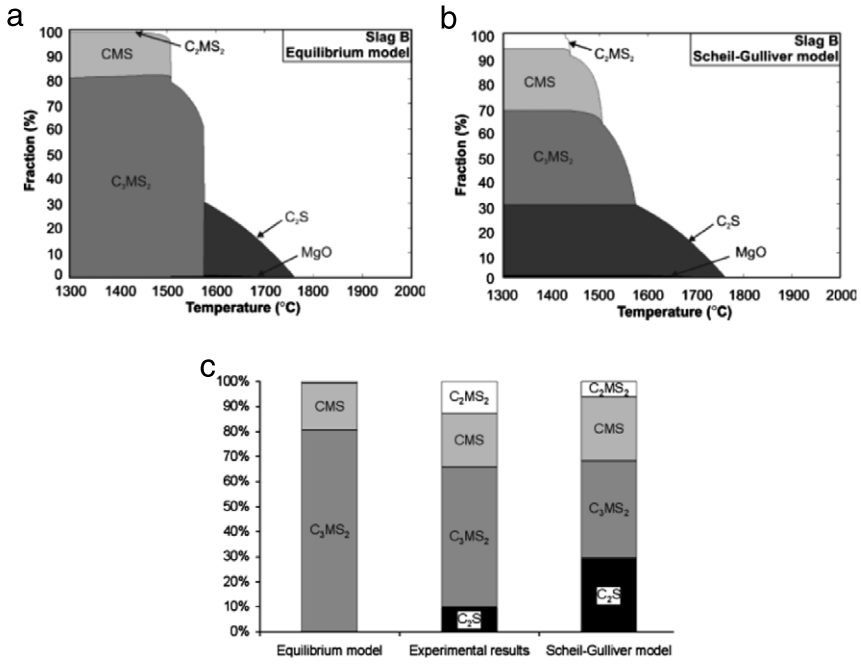

Fig. 34. Solidification simulation of 47CaO–15MgO–38SiO_2 (in wt%) slag using the Scheil–Gulliver cooling calculations [188]. Evolution of the phase fractions during the solidification with (a) the equilibrium model and (b) the Scheil–Gulliver model, and (c) the comparison with the experimentally observed mineralogy of the solidified slag.

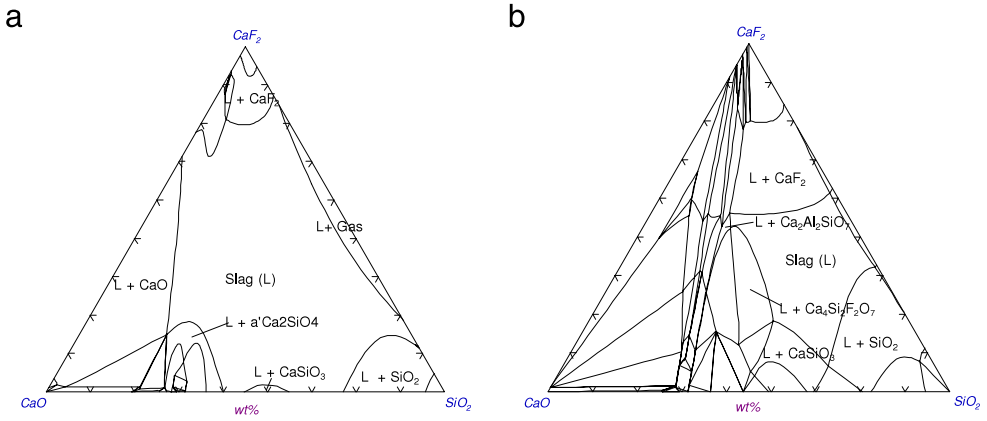

Fig. 35. Calculated isothermal phase diagrams for the CaO–SiO_2–CaF_2–10 wt%Al_2O_3 system at 1 bar [54]. (a) 1400 °C and (b) 1200 °C.

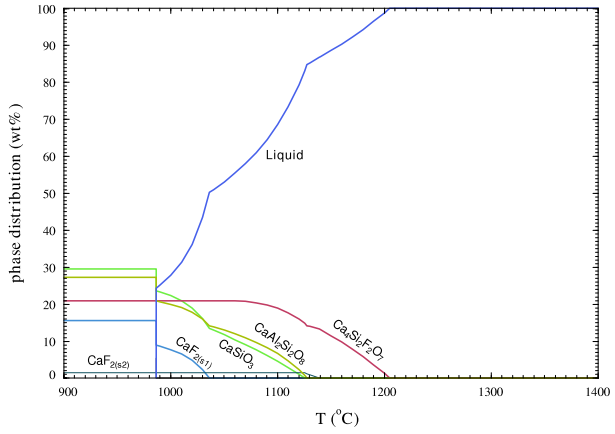

Fig. 36. Solidification simulation of the 30CaO–10Al_2O_3–40SiO_2–20CaF_2 (in wt%) mould flux using the Scheil cooling calculation [54].

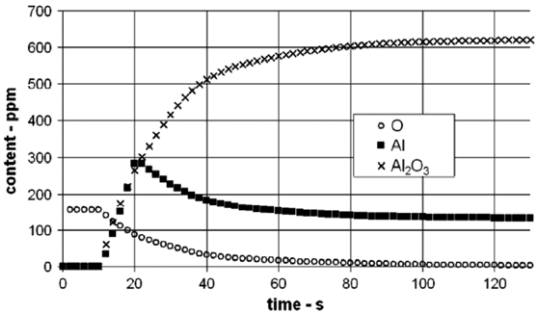

Fig. 37. Variation of soluble Al and O contents and Al_2O_3 inclusions in molten steel in a ladle during the RH process calculated from the coupling the CEQCSI and Fluent code [191].

process using carbon (cokes) will require a hydroxide database in the near future.

Many new steel grades are under development. For example, the improvement of the thermodynamic database for liquid and solid phases in the Fe–Mn–Al–Si–C–etc. system is required in order to understand solidification and segregation processes, and non-metallic inclusion formation in TWIP (Twinning Induced Plasticity) steels (containing 15.0 < wt%Mn < 30.0, 1.0 < wt%Al (or Si)

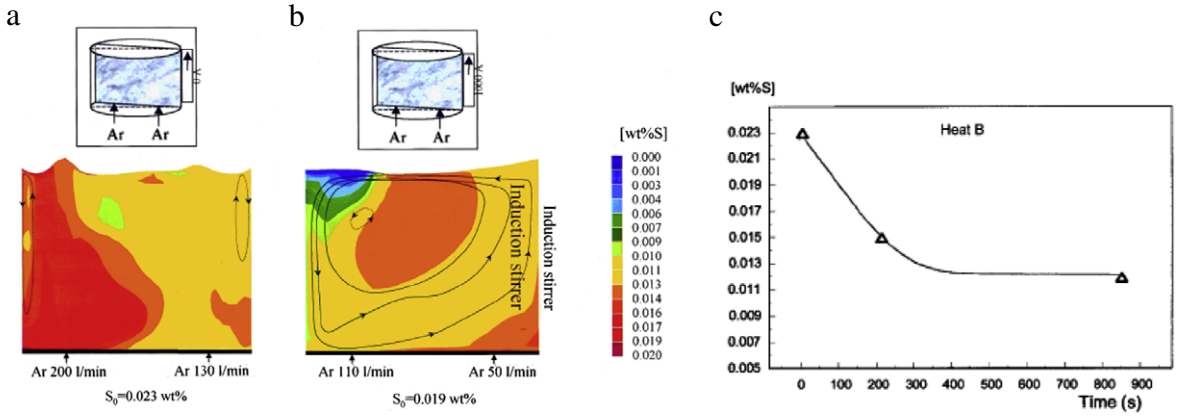

Fig. 38. Simulation of the sulfur refining process in a bottom gas-stirred ladle by coupling of ThermoCalc and CFD code [193]. Calculated concentration profiles of sulfur in steel after 3 min with (a) bottom bubbling only and (b) bottom bubbling and inductive stirring, and (c) predicted sulfur content in comparison with plant data during the process.

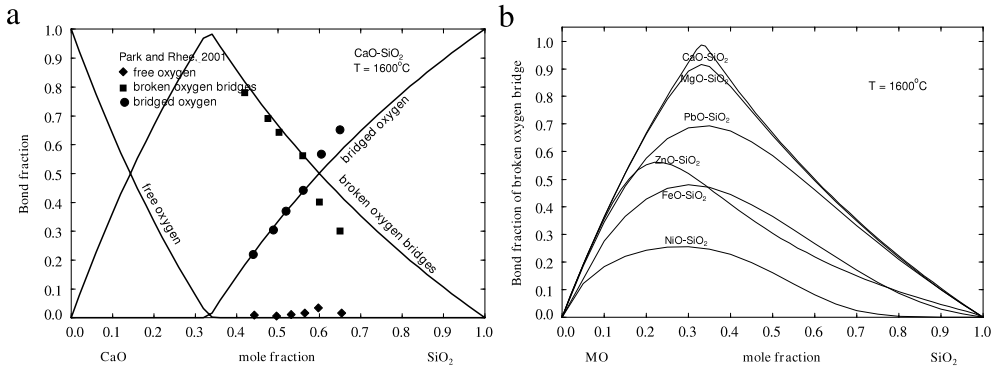

Fig. 39. Calculated silicate structure from Modified Quasichemical Model parameters. (a) Comparison of calculated bond fractions of O^{2-}, O^{-} and O^{0} for the CaO — —SiO_2 system with experimental data of Park and Rhee [206], and (b) calculated bond fractions of O^{-} for various binary silicate systems at 1600 °C.

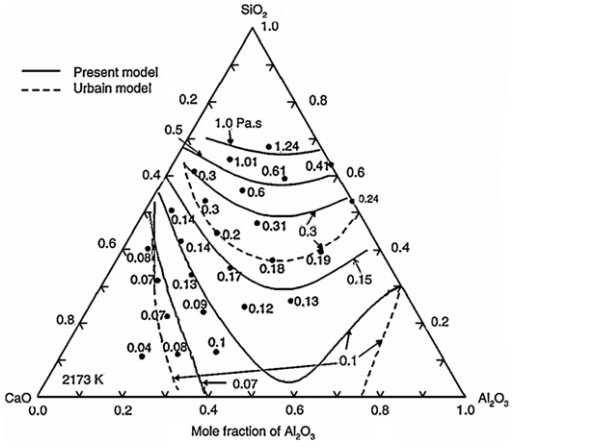

Fig. 40. Comparison between the iso-viscosity lines for $CaO–Al_2O_3–SiO_2$ slag at 1900 °C calculated from the MPE structural viscosity model [119–121] and experimental data [207].

< 3.0, 0.5 < wt%C < 1.0). The research on lightweight steels with high Al content (over 5 wt% Al) may require reinvestigation of the Fe–Al-based alloy database. The increasing usage of steel scraps can induce a substantial enrichment in tramp elements such as Cu and Sn in steels. In order to solve the problem, new ideas to remove or use tramp elements are necessary, which would require conducting thermodynamic assessments of systems with high contents of tramp elements. For example, thermodynamic data of the Cu–Fe–Al–Mn–O–S oxysulfide system can be important for the utilization of Cu as CuS precipitates.

6.2. Physical properties database

Viscosity models and databases for molten slags need to be expanded to cover a wider composition range. Viscosity calculations for 'liquid + solid' two-phase regions can be very helpful in understanding the solidification of molten slag and mould flux, which also requires accurate molar volume databases for oxide systems. The electrical conductivity of molten slag is important for optimizing the electrode consumption and electrical energy during EAF and LF operations. Thermal conductivity is also one of the key physical parameters for the mould flux design. Diffusivity modeling of oxide constituents in molten slags and interfacial energy (surface tension and interfacial tension) modeling between molten slag, molten steel, non-metallic inclusions and refractories are of importance in order to advance kinetic models for steelmaking reactions.

6.3. Coupled experiments and thermodynamic modeling

Most of the phase diagrams and thermodynamic properties of oxide systems related to the steelmaking process had been determined before 1990. Although the thermodynamic properties of molten steel and the thermodynamic reaction between molten steels and slag are still being investigated, the major metallic phase diagrams were also determined before 1990. Unfortunately, intensive research programs for the investigation of fundamental phase diagrams and thermodynamic properties of oxide and metallic systems have rarely been supported in the last two decades.

In order to improve the current processes or invent new processes in steelmaking, fundamental research should be

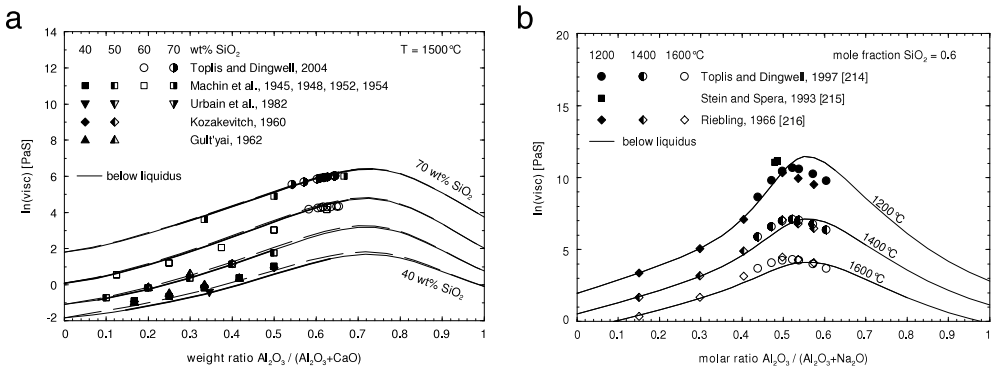

Fig. 41. Calculated viscosity lines of (a) the ternary $CaO–SiO_2–Al_2O_3$ slags and (b) the ternary $Na_2O–SiO_2–Al_2O_3$ slags from the FactSage structural viscosity model [114–116] along with experimental data [207–217].

continuously carried out along with thermodynamic modeling and calculations. In particular, the coupling of thermodynamic modeling (optimization) and experiments can overcome the problems of the classical time-consuming experimental procedure. Based on the preliminary thermodynamic modeling results, the key experimental conditions can be identified and the experimental results can subsequently be used for the improvement of thermodynamic modeling. In this way, the time and cost of the experiments can be significantly saved and the phase diagrams and thermodynamic property results can be obtained more rapidly to support the process improvement. The coupling technique can also minimize possible error in experiments. Since the phase diagram, thermodynamic properties, phase equilibria of gas/slag/refractory/liquid steel, etc. are thermodynamically correlated with each other in terms of the Gibbs energy, the results should be consistent with each other. As thermodynamic optimization takes care of all available phase diagram and thermodynamic data, the possible inconsistency between various types of experiment can be readily identified.

7. Summary

Extensive computerized thermodynamic databases have been prepared for solid and liquid steel, slags and solid oxide solutions over the last three decades by critical evaluation/optimization of all available phase equilibrium and thermodynamic data. Sophisticated thermochemical computing systems such as CEQCSI [1], FactSage [2], MPE [3], MTDATA [4] and Thermo-Calc [5] have been widely used to understand the complex steelmaking chemical reactions involving molten steel, slag, inclusion, refractory and gas phases and to develop new steel grades and process technologies. Recent developments in structural viscosity models for molten slags are also very important for steelmaking process simulations.

The thermodynamic databases for steel and non-metallic systems should be continuously expanded to keep pace with the advances in the steelmaking process and the development of new steel grades. There are increasing demands for the physical property models and databases to calculate the volume, thermal and electrical conductivities and interfacial energy related to molten slag and steel. The combination of thermodynamic calculations and process modeling will also advance the steelmaking process automation.

Acknowledgement

The author would like to thank to Dr. Marie-Aline Van Ende for her constructive discussions during the preparation of this article.

References

[1] CEQCSI: Maizières, France, www.arcelormittal.com.
[2] FactSage: Montreal, Canada, www.factsage.com.
[3] MPE: Clayton, Australia, www.csiro.au.
[4] MTDATA: Teddington, UK, www.npl.co.uk.
[5] Thermo-Calc: Stockholm, Sweden, www.thermocalc.com.
[6] G.W. Toop, C.S. Samis, Some new ionic concepts of silicate slags, Can. Metall. Quart. 1 (1962) 129–159.
[7] T. Yokokawa, K. Niwa, Free energy of solution in binary silicate melts, Trans. JIM 10 (1969) 3–7.
[8] T. Yokokawa, K. Niwa, Free energy and basicity of molten silicate solution, Trans. JIM 10 (1969) 81–84.
[9] M.L. Kapoor, M.G. Frohberg, Theoretical treatment of activities in silicate melts, Chemical Metallurgy of Iron and Steel, Iron and Steel Institute, London, 1973, pp. 17–22.
[10] C.R. Masson, I.B. Smith, S.G. Whiteway, Activities and ionic distributions in liquid silicates: application of polymer theory, Can. J. Chem. 48 (1970) 1456–1464.
[11] D.R. Gaskell, Activities and free energies of mixing in binary silicate melts, Metall. Trans. B 8B (1977) 131–145.
[12] P.L. Lin, A.D. Pelton, A structural model for binary silicate melts, Metall. Trans. B 10B (1979) 667–675.
[13] J.A. Romero-Serrano, A.D. Pelton, Extensions of a structural model for binary silicate systems, Metall. Mater. Trans. B 26B (1995) 305–315.
[14] J.A. Romero-Serrano, A.D. Pelton, Thermodynamic analysis of binary and ternary silicate systems by a structural model, ISIJ Inter. 39 (1999) 399–408.
[15] A.D. Pelton, Thermodynamic models and databases for slags, fluxes and salts. VII international conference on molten slags fluxes and salts, J. South African Inst. Min. Metall. (2004) 607–614.
[16] A.D. Pelton, M. Blander, Computer-assisted analysis of the thermodynamic properties and phase diagrams of slags, in: Proc. AIME Symposium on Metallurgical Slags and Fluxes, TMS-AIME, Warrendale, PA 1984, pp. 281–294.
[17] A.D. Pelton, M. Blander, Thermodynamic analysis of ordered liquid solutions by a modified quasichemical approach — application to silicate slags, Metall. Trans. B 17B (1986) 805–815.
[18] A.D. Pelton, S.A. Decterov, G. Eriksson, C. Robelin, Y. Dessureault, The modified quasichemical model — I binary solutions, Metall. Mater. Trans. B 31B (2000) 651–660.
[19] A.D. Pelton, P. Chartrand, The modified quasichemical model II — multicomponent solutions, Metall. Mater. Trans. A 32A (2001) 1355–1360.
[20] P. Chartrand, A.D. Pelton, The modified quasichemical model III — two sublattices, Metall. Mater. Trans. A 32A (2001) 1397–1408.
[21] A.D. Pelton, P. Chartrand, The modified quasichemical model IV — two sublattice quadruplet approximation, Metall. Mater. Trans. A 32A (2001) 1409–1416.
[22] C.W. Bale, E. Bélisle, P. Chartrand, S.A. Decterov, G. Eriksson, K. Hack, I.-H. Jung, Y.-B. Kang, J. Melançon, A.D. Pelton, C. Robelin, S. Petersen, FactSage thermochemical software and databases—recent developments, Calphad 33 (2009) 295–311.
[23] A.D. Pelton, A general 'geometric' thermodynamic model for multicomponent solutions, Calphad 25 (2001) 319–328.
[24] I.-H. Jung, S. Decterov, A.D. Pelton, Thermodynamic modeling of the $CaO–MgO–SiO_2$ system, J. Eur. Ceram. Soc. 25 (2005) 313–333.
[25] G. Eriksson, A.D. Pelton, Critical evaluation and optimization of the thermodynamic properties and phase diagrams of the $CaO–Al_2O_3$, $Al_2O_3–SiO_2$ and $CaO–Al_2O_3–SiO_2$ systems, Metall. Trans. B 24B (1993) 807–816.
[26] S.A. Decterov, I.-H. Jung, E. Jak, Y.-B. Kang, P. Hayes, A.D. Pelton, Thermodynamic modeling of the $Al_2O_3–CaO–CoO–CrO–Cr_2O_3–FeO–Fe_2O_3–MgO–MnO–NiO_2–SiO_2–S$ system and applications in ferrous process metallurgy, in: Proc. VII Int'l. Conference on Molten Slags, Fluxes and Salts, South African Inst. Mining & Metallurgy Johannesburg. 2004, pp. 839–849.

[27] I.-H. Jung, S. Decterov, A.D. Pelton, Critical thermodynamic evaluation and optimization of the MgO–Al_2O_3, CaO–MgO–Al_2O_3 and MgO-Al_2O_3–SiO_2 systems, J. Phase Equilib. 25 (2004) 329–345.
[28] I.-H. Jung, S. Decterov, A.D. Pelton, Thermodynamic modeling of the MgO–Al_2O_3–CrO–Cr_2O_3 system, J. Amer. Ceram. Soc. 88 (2005) 1921–1928.
[29] I.-H. Jung, S. Decterov, A.D. Pelton, Thermodynamic modeling of the Fe–Mg–O system, J. Phys. Chem. Solids 65 (2004) 1683–1695.
[30] S.A. Decterov, I.-H. Jung, A.D. Pelton, Thermodynamic modeling of the FeO–Fe_2O_3–MgO–SiO_2 system, J. Amer. Ceram. Soc. 85 (2002) 2903–2910.
[31] I.-H. Jung, S. Decterov, A.D. Pelton, H.-M. Kim, Y.-B. Kang, Thermodynamic evaluation and modeling of the Fe–Co–O system, Acta Mater. 52 (2004) 507–519.
[32] I.-H. Jung, Critical evaluation and thermodynamic modeling of the Mn–Cr–O system for the oxidation of SOFC interconnect, Solid State Ion. 177 (2006) 765–777.
[33] I.-H. Jung, S. Decterov, A.D. Pelton, Thermodynamic modeling of the FeO–Fe_2O_3–MgO–SiO_2 system, Metall. Mater. Trans. B. 35B (2004) 877–889.
[34] E. Jak, P. Hayes, A.D. Pelton, S.A. Decterov, Thermodynamic modeling of the Al_2O_3–CaO–FeO–Fe_2O_3–PbO–SiO_2–ZnO system with addition of K and Na with metallurgical applications, Molten 2009, Santiago, Chile, 2009, pp. 473–490.
[35] E. Jak, P. Hayes, A.D. Pelton, S. Decterov, Thermodynamic optimisation of the FeO–Fe_2O_3–SiO_2 (Fe–O–Si) system with FactSage, Inter. J. Mater. Res. 9 (2007) 847–854.
[36] P. Wu, G. Eriksson, A.D. Pelton, Critical evaluation and optimization of the thermodynamic properties and phase diagrams of the CaO–FeO, CaO–MgO, CaO–MnO, FeO–MgO, FeO–MnO and MgO–MnO systems, J. Amer. Ceram. Soc. 76 (1993) 2065–2075.
[37] P. Wu, G. Eriksson, A.D. Pelton, Critical evaluation and optimization of the thermodynamic properties and phase diagrams of the Na_2O–SiO_2 and K_2O–SiO_2 systems, J. Amer. Ceram. Soc. 76 (1993) 2059–2064.
[38] G. Eriksson, A.D. Pelton, Critical evaluation and optimization of the thermodynamic properties and phase diagrams of the MnO–TiO_2, MgO–TiO_2, FeO–TiO_2, Ti_2O_3–TiO_2, Na_2O–TiO_2 and K_2O–TiO_2 systems, Metall. Trans. B 24B (1993) 795–805.
[39] G. Eriksson, P. Wu, A.D. Pelton, Critical evaluation and optimization of the thermodynamic properties and phase diagrams of the MgO–Al_2O_3, MnO–Al_2O_3, FeO–Al_2O_3, Na_2O–Al_2O_3 and K_2O–Al_2O_3 systems, Calphad 17 (1993) 189–206.
[40] G. Eriksson, P. Wu, M. Blander, A.D. Pelton, Critical evaluation and optimization of the thermodynamic properties and phase diagrams of the MnO–SiO_2 and CaO–SiO_2 systems, Can. Metall. Quart. 33 (1994) 13–22.
[41] S. Decterov, A.D. Pelton, Critical evaluation and optimization of the thermodynamic properties and phase diagrams of the CrO–Cr_2O_3, CrO–Cr_2O_3–Al_2O_3 and CrO–Cr_2O_3–CaO systems, J. Phase Equilibr. 17 (1996) 476–487.
[42] S. Decterov, A.D. Pelton, Critical evaluation and optimization of the thermodynamic properties and phase diagrams of the CrO–Cr_2O_3–SiO_2, and CrO–Cr_2O_3–SiO_2–Al_2O_3 systems, J. Phase Equilibria 17 (1996) 488–494.
[43] S. Decterov, A.D. Pelton, Critical evaluation and optimization of the thermodynamic properties and phase diagrams of the CrO–Cr_2O_3–SiO_2–CaO system, Metall. Trans. B 28B (1997) 235–242.
[44] I.-H. Jung, Y.-B Kang, S.A. Decterov, A.D. Pelton, Thermodynamic evaluation and optimization of the MnO–Al_2O_3 and MnO–Al_2O_3–SiO_2 systems, Metall. Mater. Trans. B 35B (2004) 259–268.
[45] Y.-B. Kang, I.-H. Jung, S. Decterov, A.D. Pelton, H.-G. Lee, Phase equilibria and thermodynamic properties of the CaO–MnO–Al_2O_3–SiO_2 system by critical evaluation, modeling and experiment, ISIJ Inter. 44 (2004) 975–983.
[46] Y.-B. Kang, I.-H. Jung, S. Decterov, A.D. Pelton, H.-G. Lee, Thermodynamic evaluation and optimization of the CaO–MnO–SiO_2 and CaO–MnO–Al_2O_3 systems, ISIJ Inter. 44 (2004) 965–974.
[47] Y.-B. Kang, I.-H. Jung, Thermodynamic modeling of pyrometallurgical oxide systems containing Mn oxides, Molten 2009, Santiago, Chile, 2009, pp. 459–471.
[48] Y.-B. Kang, I.-H. Jung, H.-G. Lee, Critical thermodynamic evaluation and optimization of the MnO–"TiO_2"–"Ti_2O_3" system, Calphad 30 (2006) 235–247.
[49] Y.-B. Kang, I.-H. Jung, H.-G. Lee, Critical thermodynamic evaluation and optimization of the MnO–SiO_2 "TiO_2"–"Ti_2O_3" system, Calphad 30 (2006) 226–234.
[50] S.A. Decterov, V. Swamy, I.-H. Jung, Thermodynamic modeling of B_2O_3–SiO_2 and B_2O_3–Al_2O_3 systems, Inter. J. Mater. Res. 98 (2007) 987–994.
[51] S. Arnout, M. Guo, I.-H. Jung, B. Blanpain, P. Wollants, Experimental determination of CaO–CrO–Cr_2O_3–MgO–SiO_2 and thermodynamic modeling of the CrO–Cr_2O_3–MgO–SiO_2 system, J. Amer. Ceram. Soc. 92 (2009) 1831–1839.
[52] V. Swamy, I.-H. Jung, S. Decterov, Thermodynamic modeling of the Al_2O_3–B_2O_3–SiO_2 system, J. Non-Cryst. Solids 355 (2009) 1679–1686.
[53] Y.-B. Kang, A.D. Pelton, Thermodynamic model and database for sulfides dissolved in molten oxide slags, Metall. Mater. Trans. B 40B (2009) 979–994.
[54] I.-H. Jung, Thermodynamic modeling of the CaF_2 containing slags and its applications to steelmaking processes, in: Asia Steel Conf. 2009, Pusan Korea, paper S3–30.
[55] H. Gaye, J. Welfringer, Modelling of the thermodynamic properties of complex metallurgical slags, in: Proc. AIME Symposium on Metallurgical Slags and Fluxes, TMS-AIME, Warrendale, PA, 1984, pp. 357–379.
[56] H. Gaye, J. Lehmann, T. Matsumiya, W. Yamada, A statistical thermodynamics model of slags: applications to systems containing S, F, P_2O_5 and Cr oxides, in: 4th Inter. Conf. Molten Slags and Fluxes, Sendai, ISIJ, 1992, pp. 103–108.
[57] J. Lehmann, H. Gaye, Modeling of thermodynamic properties of sulphur bearing metallurgical slags, Rev. Int. Hautes. Tempér. Réfract., Fr. 28 (1992–1993) 81–90.
[58] J. Lehmann, H. Gaye, P. Rocabois, The IRSID slag model for steelmaking process control, in: 2nd Inter. Conf. Mathematical Modeling and Computer Simulation of Metal Technologies, MMT 2000, Ariel, Israel, 2000, pp. 89–96.
[59] J. Lehmann, N. Botems, M. Simonnet, P. Gardin, L. Zhang, Thermodynamics, precipitation kinetics, coupled models development: three main axes of research in physical chemistry at ArcelorMittal global R&D Maizières process, in: Gupta and Lollchund (Eds.), Advances in Theory of Ironmaking and Steelmaking, Bangalore, India, 2009, pp. 232–239.
[60] L. Zhang, S. Sun, S. Jahanshahi, An approach to modeling Al_2O_3 containing slags with cell model, J. Phase Equilib. Diff. 28 (2007) 121–129.
[61] J. Lehmann, F. Bonnet, M. Bobadilla, Thermodynamic description of liquid steel and metallurgical slags by the generalized central atom model, AIST Trans. 3 (2006) 114–123.
[62] L. Zhang, J. Lehmann, Application of the generalized central atom model to oxide slags, Molten 2009, Santiago, Chile, 2009, pp. 403–411.
[63] J. Lehmann, Application of ArcelorMittal Maizières thermodynamic models to liquid steel elaboration, Rev. Metall. 105 (2008) 539–550.
[64] R.H. Davies, A.T. Dinsdale, J.A. Gisby, J.A.J. Robinson, S.M. Martin, MTDATA — thermodynamic and phase equilibrium software from the national physical laboratory, Calphad 26 (2002) 229–271.
[65] J.R. Taylor, A.T. Dinsdale, Thermodynamic and phase diagram data for the CaO–SiO_2 system, Calphad 14 (1990) 71–88.
[66] T.I. Barry, A.T. Dinsdale, J.A. Gisby, Predictive thermochemistry and phase equilibria of slags, JOM 45 (1993) 32–38.
[67] A.T. Dinsdale, S.M. Hodson, T.I. Barry, J.R. Taylor, Computations using MTDATA of metal–matte–slag–gas equilibria, in: Proc. Conf. 27th Annual Conference of Metallurgists CIM, Montreal, 1988, pp. 11–59.
[68] K.E. Spear, T.M. Besmann, E.C. Beahm, Thermochemical modeling of glass: application to high-level nuclear waste glass, MRS Bull. (April) (1999) 37–44.
[69] T.M. Besmann, K.E. Spear, Thermochemical modeling of oxide glasses, J. Amer. Ceram. Soc. 85 (2002) 2887–2894.
[70] E. Yazhenskikh, K. Hack, M. Muller, Critical thermodynamic evaluation of oxide systems relevant to fuel ashes and slags. Part 4: sodium oxide–potassium oxide–silica, Calphad 32 (2008) 506–513.
[71] E. Yazhenskikh, Development of a new database for thermodynamic modelling of the system Na_2O–K_2O–Al_2O_3–SiO_2. Ph.D. Thesis, RWTH Aachen, Germany, 2005.
[72] M. Hillert, B. Jansson, B. Sundman, J. Agren, A two-sublattice model for molten solutions with different tendency of ionization, Metall. Trans. A 16A (1985) 261–266.
[73] J.-O. Andersson, T. Helander, L. Höglund, P. Shi, B. Sundman, Thermo-Calc & DICTRA, computational tools for materials science, Calphad 26 (2002) 273–312.
[74] W. Huang, M. Hillert, X. Wang, Thermodynamic assessment of the CaO–MgO–SiO_2 system, Metall. Mater. Trans. A 26A (1995) 2293–2310.
[75] H. Mao, M. Hillert, M. Selleby, B. Sundman, Thermodynamic assessment of the CaO–Al_2O_3–SiO_2 system, J. Amer. Ceram. Soc. 89 (2006) 298–308.
[76] H. Mao, O. Fabrichnaya, M. Selleby, B. Sundman, Thermodynamic assessment of the MgO–Al_2O_3–SiO_2 system, J. Mater. Res. 20 (2005) 975–986.
[77] M. Selleby, An assessment of the Ca–Fe–O–Si system, Metall. Mater. Trans. B 28B (1997) 577–596.
[78] B. Hallstedt, Thermodynamic assessment of the CaO–MgO–Al_2O_3 system, J. Amer. Ceram. Soc. 78 (1995) 193–198.
[79] M. Hillert, B. Sundman, X. Wang, An assessment of the CaO–SiO_2 system, Metall. Trans. B 21B (1990) 303–312.
[80] M. Hillert, M. Selleby, B. Sundman, An assessment of the Ca–Fe–O system, Metall. Trans. A 21A (1990) 2759–2776.
[81] B. Hallstedt, Assessment of the CaO–Al_2O_3 system, J. Amer. Ceram. Soc. 73 (1990) 15–23.
[82] B. Hallstedt, Thermodynamic assessment of the system MgO–Al_2O_3, J. Amer. Ceram. Soc. 75 (1992) 1497–1507.
[83] B. Hallstedt, Thermodynamic calculation of some subsystems of the Al–Ca–Mg–Si–O system, J. Phase Equilib. 14 (1993) 662–675.
[84] M. Hillert, The compound energy formalism, J. Alloy Compd. 320 (2001) 161–176.
[85] I.-H. Jung, Critical evaluation and thermodynamic modeling of phase equilibria in multicomponent oxide systems, Ph.D. Thesis, Ecole Polytechnique, Montreal, Canada, 2004.
[86] H.S.C. O'Neill, A. Navrotsky, Cation distributions and thermodynamic properties of binary spinel solid solutions, Amer. Mineral. 69 (1984) 733–753.
[87] J.R. Taylor, A.T. Dinsdale, A thermodynamic assessment of the Cr–Fe–O system, Z. Metallkd. 84 (1993) 335–345.
[88] J.R. Taylor, A.T. Dinsdale, A thermodynamic assessment of the Ni–O, Cr–O and Cr–Ni–O systems using the ionic liquid and compound energy models, Z. Metallkd. 81 (1990) 354–366.
[89] B. Sundman, An assessment of the Fe–O system, J. Phase Equilib. 12 (1991) 127–140.
[90] C. Wagner, Thermodynamics of Alloys, Addison-Wesley, Reading, MA, 1962, 51.

[91] G.K. Sigworth, J.F. Elliott, Thermodynamics of liquid dilute iron alloys, Met. Sci. 8 (1974) 298–310.
[92] Steelmaking Data Sourcebook, JSPS, 19th Committee on Steelmaking, Gordon & Breach Science, New York, NY, 1988.
[93] A.D. Pelton, C.W. Bale, A modified interaction parameter formalism for non-dilute solutions, Metall. Trans. A 17A (1986) 1211–1215.
[94] C.W. Bale, A.D. Pelton, The unified interaction parameter formalism: thermodynamic consistency and applications, Metall. Trans. A 21A (1990) 1997–2002.
[95] A.D. Pelton, The polynomial representation of thermodynamic properties in dilute solutions, Metall. Mater. Trans. B 28B (1997) 869–876.
[96] Y.E. Lee, Thermodynamic assessment of liquid Mn–Fe–C system by unified interaction parameter model, ISIJ Inter. 43 (2003) 144–152.
[97] H. Li, A. Morris, Evaluation of unified interaction parameter model parameters for calculating activities of ferromanganese alloys: Mn–Fe–C, Mn–Fe–Si, and Mn–Fe–C–Si systems, Metall. Mater. Trans. B 28B (1997) 553–562.
[98] M.C. Heuzey, A.D. Pelton, Critical evaluation and optimization of the thermodynamic properties of liquid tin solutions, Metall. Mater. Trans. B 27B (1996) 810–828.
[99] M. Hillert, A modified regular-solution model for terminal solutions, Metall. Trans. A 17A (1986) 1878–1879.
[100] L.S. Darken, Thermodynamics of binary metallic solutions, Metall. Soc. AIME Trans. 239 (1967) 80–89.
[101] T. Miki, M. Hino, Numerical analysis on Si deoxidation of molten Fe, Ni, Fe–Ni, Fe–Cr, Fe–Cr–Ni, Ni–Cu and Ni–Co alloys by quadratic formalism, ISIJ Inter. 45 (2005) 1848–1855.
[102] A. Hayashi, T. Uenishi, H. Kandori, T. Miki, M. Hino, Aluminum deoxidation equilibrium of molten Fe–Ni alloy coexisting with alumina or hercynite, ISIJ Inter. 48 (2008) 1533–1541.
[103] S.H. Seok, T. Miki, M. Hino, Ti deoxidation equilibrium in molten Fe–Ni alloys at temperatures between 1823 and 1923 K, ISIJ Inter. 49 (2009) 804–808.
[104] I.-H. Jung, S.A. Decterov, A.D. Pelton, A thermodynamic model for deoxidation equilibria in steel, Metall. Mater. Trans. B 35B (2004) 493–507.
[105] I.-H. Jung, Thermodynamic assessment of liquid Fe–M–S system (unpublished work).
[106] P. Rocabois, J. Lehmann, H. Gaye, M. Wintz, Kinetics of precipitation of non-metallic inclusions during solidification of steel, J. Crystal Growth 198/199 (1999) 838–843.
[107] H. Gaye, P. Rocabois, P. Lehmann, M. Bobadilla, Kinetics of inclusion precipitation during steel solidification, Steel Res. 70 (1999) 356–361.
[108] J. Lehmann, P. Rocabois, H.J. Gaye, Kinetic model of non-metallic inclusions' precipitation during steel solidification, J. Non-Crystalline Solids 282 (2001) 61–71.
[109] A.D. Pelton, G. Eriksson, J.A. Romero-Serrano, Calculation of sulfide capacities of multicomponent slags, Metall. Trans. B 24B (1993) 817–825.
[110] A.D. Pelton, Thermodynamic calculation of gas solubilities in oxide melts and glasses, Glastech. Ber. 72 (1999) 214–226.
[111] I.-H. Jung, Thermodynamic modeling of gas solubility in molten slags (I) — carbon and nitrogen, ISIJ Inter. 46 (2006) 1577–1586.
[112] I.-H. Jung, Thermodynamic modeling of gas solubility in molten slags (II) — water, ISIJ Inter. 46 (2006) 1587–1593.
[113] SGTE database, www.sgte.org.
[114] A.N. Grundy, H. Liu, I.-H. Jung, S. Decterov, A.D. Pelton, A model to calculate the viscosity of silicate melts, part I: viscosity of binary SiO_2–MeO_x systems (Me = Na, K, Ca, Mg, Al), Inter. J. Mater. Res. 99 (2008) 1185–1194.
[115] A.N. Grundy, I.-H. Jung, S. Decterov, A.D. Pelton, A model to calculate the viscosity of silicate melts, part II: the $NaO_{0.5}$–MgO–CaO–$AlO_{1.5}$–SiO_2 system, Inter. J. Mater. Res. 99 (2008) 1195–1209.
[116] S.A. Decterov, A.N. Grundy, A.D. Pelton, A model and database for the viscosity of molten slags, Molten 2009, Santiago, Chile, 2009, pp. 423–431.
[117] L. Zhang, S. Jahanshahi, S. Sun, C. Chen, B. Bourke, S. Wright, M. Somerville, CSIRO's multiphase reaction models and their industrial applications, JOM (2002) 51–56.
[118] S. Jahanshahi, S. Sun, L. Zhang, Recent developments in physico-chemical characterization and modelling of ferroalloy slag systems, J. South Afr. Inst. Min. Metall. (2004) 529–540.
[119] L. Zhang, S. Jahanshahi, Review and modeling of viscosity of silicate melts: part I. Viscosity of binary and ternary silicates containing CaO, MgO, and MnO, Metall. Mater. Trans. B 29B (1998) 177–186.
[120] L. Zhang, S. Jahanshahi, Review and modeling of viscosity of silicate melts: part II. viscosity of melts containing iron oxide in the CaO–MgO–MnO–FeO–Fe_2O_3–SiO_2 system, Metall. Mater. Trans. B 29B (1998) 187–195.
[121] L. Zhang, S. Jahanshahi, Modelling viscosity of alumina-containing silicate melts, Scand. J. Metall. 30 (2001) 364–369.
[122] J.A.J. Robinson, A.T. Dinsdale, P.N. Quested, The prediction of thermophysical properties of steels and slags, 2nd Inter. Cong. Sci. Tech. Steelmaking, U. Wales, Swansea, 2001.
[123] I.-H. Jung, S. Decterov, A.D. Pelton, Computer applications of thermodynamic databases to inclusion engineering, ISIJ. Inter. 44 (2004) 527–536.
[124] Y.-B. Kang, H.-G. Lee, Inclusions chemistry for Mn/Si deoxidized steels. Thermodynamic predictions and experimental confirmations, ISIJ. Inter. 44 (2004) 1006–1015.
[125] H. Gaye, M. Faral, J. Lehmann, Computational thermodynamics applied to steel elaboration, Rev. Métallurgie 100 (2003) 125–134.
[126] I.-H. Jung, S. Decterov, A.D. Pelton, Y.-B. Kang, H.-G. Lee, Critical thermodynamic evaluation and optimization of the CaO–MnO–Al_2O_3–SiO_2 system and application to inclusion control, in: K.S. Coley, G. Brooks (Eds.), Proc. CIM Symposium, Ladle and Tundish Technology, Canadian Institute of Metallurgy, Montreal, 2002, pp. 131–147.
[127] D.-H. Woo, Ph.D. Thesis, Postech, Pohang Korea, 2010.
[128] A. Hasegawa, K. Morita, N. Sano, Phase equilibria for the MnO–SiO2–MnS slag system, Tetsu to Hagane 81 (1995) 1109–1113.
[129] H. Gaye, J. Lehmann, P. Rocabois, F. Ruby-Meyer, Computational thermodynamics and slag modeling applied to steel elaboration, Steel Res. 72 (2001) 446–451.
[130] F. Ruby-Meyer, J. Lehmann, H. Gaye, Thermodynamic analysis of inclusions in Ti-deoxidized steels, Scand. J. Metall. 29 (2000) 206.
[131] H. Matsuura, C. Wang, G. Wen, S. Sridhar, The transient stages of inclusion evolution during Al and/or Ti additions to molten iron, ISIJ Inter. 47 (2007) 1265–1274.
[132] D.-C. Park, I.-H. Jung, P.C.H. Rhee, H.-G. Lee, Reoxidation of Al–Ti containing steels by CaO–Al_2O_3–MgO–SiO_2 slag, ISIJ Inter. 44 (2004) 1669–1678.
[133] S. Basu, S.K. Choudhary, N.U. Girase, Nozzle clogging behaviour of Ti-bearing Al-killed ultralow carbon steel, ISIJ Inter. 44 (2004) 1653–1660.
[134] I.-H. Jung, G. Eriksson, P. Wu, A.D. Pelton, Thermodynamic modeling of the Al_2O_3–Ti_2O_3–TiO_2 system and its applications to the Fe–Al–Ti–O inclusion diagram, ISIJ Inter. (2009) 1290–1297.
[135] M.-A. Van Ende, M. Guo, R. Dekkers, M. Burty, J. Van Dyck, P.T. Jones, B. Blanpain, P. Wollants, Formation and evolution of Al–Ti oxide inclusions during secondary steel refining, ISIJ Inter. 49 (2009) 1133–1140.
[136] D.S. Sarma, A.V. Karasev, P.G. Jönsson, On the role of non-metallic inclusions in the nucleation of acicular ferrite in steels, ISIJ Inter. 49 (2009) 1063–1074.
[137] H.S. Kim, H.-G. Lee, K.-S. Oh, MnS precipitation in association with manganese silicate inclusions in Si/Mn deoxidized steel, Metall. Mater. Trans. A 32A (2001) 1519–1525.
[138] C.-H. Chang, I.-H. Jung, S.-C. Park, H.S. Kim, H.-G. Lee, Effect of Mg on the evolution of non-metallic inclusions in Mn–Si–Ti deoxidized steel during solidification: experiments and thermo-dynamic calculations, Ironmaking Steelmaking 32 (2005) 251–257.
[139] S.-C. Park, I.-H. Jung, K.-S. Oh, H.-G. Lee, Effect of Al on the evolution of non-metallic inclusions in Mn–Si–Ti–Mg deoxidized steel during solidification: experiments and thermodynamic calculations, ISIJ Inter. 44 (2004) 1016–1023.
[140] Y.-B. Kang, C.-H. Chang, S.-C. Park, H.S. Kim, I.-H. Jung, H.-G. Lee, Thermodynamic of inclusion engineering in steelmaking and refining, Iron Steel Technol. 10 (2006) 154–162.
[141] Y.-B. Kang, H.-G. Lee, Thermodynamic analysis of Mn-depleted-zone near Ti oxide inclusions for intragranular nucleation of ferrite in steel, ISIJ Inter. 50 (2010) 501–508.
[142] J.H. Shim, J.S. Byun, Y.W. Cho, Y.J. Oh, J.D. Shim, D.N. Lee, Mn absorption characteristics of Ti_2O_3 inclusions in low carbon steels, Scr. Mater. 44 (2001) 49.
[143] J.H. Shim, Y.J. Oh, J.Y. Suh, Y.W. Cho, J.D. Shim, J.S. Byun, D.N. Lee, Ferrite nucleation potency of non-metallic inclusions in medium carbon steels, Acta. Mater. 49 (2001) 2115.
[144] J.S. Byun, J.H. Shim, Y.W. Cho, D.N. Lee, Non-metallic inclusion and intragranular nucleation of ferrite in Ti-killed C–Mn steel, Acta Mater. 51 (2003) 1593.
[145] C. Van Der Eijk, O. Grong, J. Walmsley, Mechanisms of inclusion formation in low alloy steels deoxidized with titanium, Mater. Sci. Tech. 16 (2000) 55–64.
[146] C. Van Der Eijk, Ph.D. Dissertation, NTNU, Trondheim, Norway, 1999.
[147] H.H. Visser, W.K. Tiekink, M. Koolwijk, R.A.L. Kooter, F. Mensonides, JPTM. Brockhoff, Solid inclusions in calcium treated aluminium-killed steel, Inter. Conf. Clean Steel 7, Balatonfured, Hungary, 2007, paper no. 10.
[148] L. Holappa, M. Hämäläinen, M. Liukkonen, M. Lind, Thermodynamic examination of inclusion modification and precipitation from calcium treatment to solidified steel, Ironmaking Steelmaking 30 (2003) 111–115.
[149] D.J. Sosinsky, I.D. Sommerville, The composition and temperature dependence of the sulfide capacity of metallurgical slags, Metall. Trans. B 17B (1986) 331–337.
[150] H. Gaye, J. Lehmann, Modelling and prediction of reactions involving metals, slags and fluxes, J. South Afr. Inst. Min. Metall. (2004) 619–624.
[151] S. Decterov, Y.-B. Kang, I.-H. Jung, Thermodynamic database for the Al–Ca–Co–Cr–Fe–Mg–Mn–Ni–Si–O–P–S system and applications in ferrous process metallurgy, J. Phase Equilib. Diff. 30 (2009) 443–461.
[152] C.J.B. Fincham, F.D. Richardson, Sulfur in silicate and aluminate slags, J. Iron Steel Inst. 178 (1954) 4–15.
[153] K.P. Abraham, M.W. Davies, F.D. Richardson, Sulfide capacities of silicate melts, J. Iron Steel Inst. 196 (1960) 309–312.
[154] P.T. Carter, T.G. MacFarlane, J. Iron Steel Inst. 185 (1957) 62–66.
[155] S.D. Brown, R.J. Roxburgh, I. Ghita, H.B. Bell, Ironmaking Steelmaking 9 (1982) 163–167.
[156] M. Gornerup, O. Wijk, Sulfide capacities of CaO–Al_2O_3–SiO_2 slags at 1550, 1600 and 1650°C, Scand. J. Metall. 25 (1996) 103–107.
[157] M. Chapman, O. Ostrovski, G. Tranell, S. Jahanshahi, Sulfide capacity of titania-containing slags, Elektrometallurgiya 3 (2000) 34–39.
[158] K.P. Abraham, F.D. Richardson, Sulfide capacities of silicate melts I, J. Iron Steel Inst. 196 (1960) 313–317.
[159] R. Nagabayashi, M. Hino, S. Banya, Distribution of phosphorus between liquid iron and Fe_tO–(CaO + MgO)–(SiO_2 + P_2O_5) phosphate slags, Tetsu to Hagane 74 (1988) 1770–1777.

[160] Y. Iguchi, T. Fuwa, Trans. Solubility of water in liquid calcium oxide–silicon dioxide–magnesium oxide with and without iron (II) oxide at 1550°C, Iron Steel Inst. Japan 10 (1970) 29–35.
[161] D.J. Sosinsky, M. Maeda, A. McLean, Determination and prediction of water vapor solubilities in calcium oxide–magnesium oxide–silicon dioxide slags, Metall. Trans. B 16B (1985) 61–66.
[162] S. Zhang, N.J. Marriott, W.E. Lee, Thermochemistry and microstructure of MgO–C refractories containing various antioxidants, J. Eur. Ceram. Soc. 21 (2001) 1037–1047.
[163] C.F. Chan, B.B. Argent, W.E. Lee, Influence of additives on slag resistance of Al_2O_3–SiO_2–SiC–C refractory bond phases under reducing atmosphere, J. Amer. Ceram. Soc. 81 (1998) 3177–3188.
[164] C.F. Chan, B.B. Argent, W.E. Lee, Prediction of the effect of additives on slag resistance of Al_2O_3–SiO_2–SiC–C bond phases in air, Calphad 27 (2003) 115–125.
[165] M.K. Cho, I.H. Jung, Thermodynamic modeling and its applications to refractory design for steelmaking process. Symposium on Steelmaking Technologies — Refractories in steelmaking, KIMM, Pohang, Korea, May 2009.
[166] S. Zhang, W.E. Lee, Use of phase diagrams in studies of refractories corrosion, Inter. Mater. Rev. 45 (2000) 41–58.
[167] W.E. Lee, S. Zhang, Refractories: controlled microstructure composites for extreme environments, J. Mater. Sci. 39 (2004) 6675–6685.
[168] W.E. Lee, B.B. Argent, S. Zhang, Complex phase equilibria in refractories design and use, J. Amer. Ceram. Soc. 85 (2002) 2911–2918.
[169] I.H. Jung, S. Decterov, A.D. Pelton, Computer application of thermodynamic databases to corrosion of refractories, Taikabutsu 56 (2004) 382–386.
[170] K. Goto, B.B. Argent, W.E. Lee, Corrosion of MgO–$MgAl_2O_4$ spinel refractory bricks by calcium aluminosilicate slag, J. Amer. Ceram. Soc. 80 (1997) 461–471.
[171] F. Melcher, V. Reiter, H. Harmuth, Investigations of corrosion of different alumina spinel castables by ladle slags, UNITECR (2007) 230–233.
[172] S.A. Nightingale, G.A. Brooks, B.J. Monaghan, Degradation of MgO refractory in CaO–SiO_2–MgO–FeO_X and CaO–SiO_2–Al_2O_3–MgO–FeO_X slags under forced convection, Metall. Mater. Trans. B 36B (2005) 453–461.
[173] V. Reiter, F. Melcher, H. Harmuth, Thermochemical modeling of EAF slags and refractory/slag equilibria, UNITECR (2007) 170–173.
[174] J.H. Park, Formation of $CaZrO_3$ at the interface between CaO–SiO_2–MgO–CaF_2(–ZrO_2) slags and magnesia refractories: computational and experimental study, Calphad 31 (2007) 149–154.
[175] A. Kaiser, R. Telle, M. Lobert, Thermodynamics and kinetics of the zircon($ZrSiO_4$) decomposition and the effect of alkaline – and alkaline earth – oxides, UNITECR (2007) 272–275.
[176] R. Artir, W.E. Lee, B.B. Argent, P.H. Larsen, Reactions of aluminium and silicon in MgO–graphite composites Al prediction of phase constitution using MTDATA, High Temp. Mater. Sci. 34 (1995) 69–103.
[177] W.E. Lee, S. Zhang, Melt corrosion of oxide and oxide–carbon refractories, Int. Mater. Rev. 44 (1999) 77–104.
[178] M.A. Van Ende, M. Guo, P.T. Jones, B. Blanpain, P. Wollants, Degradation of MgO–C refractories by MnO-rich stainless steel slags, Ceram. Int. 35 (2009) 2203–2212.
[179] K. Beskow, J. Jia, C.H.P. Lupis, D. Sichen, Chemical characteristics of inclusions formed at various stages during the ladle treatment of steel, Ironmaking Steelmaking 29 (2002) 427.
[180] K. Beskow, D. Sichen, Ladle glaze: major source of oxide inclusions during ladle treatment of steel, Ironmaking Steelmaking 31 (2004) 393.
[181] K. Beskow, D. Sichen, N. Sano, Thermodynamic analysis on the formation and chemical development of nonmetallic inclusions in ladle treatment of tool steels, Iron Steel Technol. 3 (2006) 103.
[182] J.H. Son, I.H. Jung, S.M. Jung, H. Gaye, H.G. Lee, Chemical reaction of glazed refractory with Al-deoxidized molten steel, ISIJ Inter. 48 (2008) 1542–1551.
[183] A.B. Fox, M.E. Valdez, J. Gisby, R.C. Atwood, P.D. Lee, S. Sridhar, Dissolution of ZrO_2, Al_2O_3, MgO and $MgAl_2O_4$ particles in a B_2O_3 containing commercial fluoride-free mould slag, ISIJ Inter. 44 (2004) 836–845.
[184] J.-H. Park, I.-H. Jung, H.G. Lee, Dissolution of Al_2O_3 and MgO in molten slag, ISIJ Inter. 46 (2006) 1626–1634.
[185] S.A. Nightingale, B.J. Monaghan, Kinetics of spinel formation and growth during dissolution of MgO in CaO–Al_2O_3–SiO_2slag, Metall. Mater. Trans. B 39B (2008) 643–648.
[186] B.J. Monaghan, L. Chen, J. Sorbe, Comparative study of oxide inclusion dissolution in CaO–SiO_2–Al_2O_3 slag, Ironmaking Steelmaking 32 (2005) 258–264.
[187] J. Liu, M. Guo, P.T. Jones, F. Verhaeghe, B. Blanpain, P. Wollants, In situ observation of the direct and indirect dissolution of MgO particles in CaO–Al2O3–SiO2-based slags, J. Eur. Ceram. Soc. 27 (2007) 1961–1972.
[188] D. Durinck, P.T. Jones, B. Blanpain, P. Wollants, Slag solidification modeling using the Scheil–Gulliver assumptions, J. Amer. Ceram. Soc. 90 (2007) 1177–1185.
[189] J-H. Park, Solidification structure of CaO–SiO_2–MgO–Al_2O_3(–CaF_2) systems and computational phase equilibria: crystallization of $MgAl_2O_4$ spinel, Calphad 31 (2007) 428–437.
[190] D. Durinck, P.T. Jones, B. Blanpain, P. Wollants, Air-cooling of metallurgical slags containing multivalent oxides, J. Amer. Ceram. Soc. 91 (2008) 3342–3348.
[191] M. Simonnet, J.F. Domgin, J. Lehmann, P. Gardin, Numerical tool coupling fluid dynamics and thermochemistry to predict and to optimize deoxidation processes, BHM Berg-und Hüttenmännische Monatshefte 152 (2007) 350–354.
[192] P. Gardin, J.F. Somgin, M. Simonnet, J. Lehmann, Modelling of inclusion evolution in a steel ladle or in RH degasser, Rev. Métallurgie 105 (2008) 84–91.
[193] L. Jonsson, D. Sichen, P. Jönsson, A new approach to model sulphur refining in a gas-stirred ladle—a coupled CFD and thermodynamic model, ISIJ Inter. 38 (1998) 260–267.
[194] M. Andersson, M. Hallberg, L. Jonsson, P. Jönsson, Slag–metal reactions during ladle treatment with focus on desulphurisation, Ironmaking and Steelmaking 29 (2002) 224–232.
[195] G.J. Hassall, K.G. Bain, R.W. Young, M.S. Millman, Studies in development of clean steels part 1 modelling aspects, Ironmaking Steelmaking 25 (1998) 273–278.
[196] M. Ersson, L. Höglund, A. Tilliander, L. Jonsson, P. Jönsson, Dynamic coupling of computational fluid dynamics and thermodynamic software: applied on a top blown converter, ISIJ Inter. 48 (2008) 147–153.
[197] K.C. Mills, A.B. Fox, L. Chapman, S. Sridhar, Round robin program for slag viscosity estimation, Scand J. Metall. 30 (2001) 396–404.
[198] G. Urbain, Viscosity estimation of slags, Steel Res. 58 (1987) 111–116.
[199] T. Iida, H. Sakal, Y. Klta, K. Shigeno, An equation for accurate prediction of the viscosities of blast Furnace type slags from chemical composition, ISIJ Inter. 40 (2000) S110–S114.
[200] D. Schen, J. Bygd'en, S. Seetharaman, A model for estimation of viscosities of complex metallic and ionic melts, Metall. Mater. Trans. B 25 (1994) 519–525.
[201] S. Seetharaman, D. Sichen, Viscosities of high temperature systems—a modeling approach, ISIJ Inter. 37 (1997) 109–118.
[202] S. Seetharaman, D. Sichen, Y.J. Zhang, The computer-based study of multicomponent slag viscosities, JOM (Aug) (1999) 33–40.
[203] A. Kondratiev, E. Jak, A quasi-chemical viscosity model for fully liquid slags in the Al_2O_3–CaO–'FeO'–SiO_2 system, Metall. Mater. Trans. B 36B (2005) 623–638.
[204] E. Jak, Viscosity model for slags in the Al_2O_3–CaO–'FeO'–K_2O–Na_2O–MgO–SiO_2 system. Molten 2009, Santiago, Chile, 2009, pp. 433–448.
[205] M. Nakamoto, Y. Miyabayashi, L. holappa, T. Tanaka, A model for estimating viscosities of aluminosilicate melts containing alkali oxides, ISIJ Inter. 47 (2007) 1409–1414.
[206] J.H. Park, P.C.H. Rhee, Ionic properties of oxygen in slag, J. Non-Crystalline Solids 282 (2001) 7–14.
[207] P. Kozakevitch, Viscosité et éléments structuraux des aluminosilicates fondus: laitiers CaO–Al_2O_3–SiO_2 entre 1600 et 2100C, Rév. Métall. 57 (1960) 149–160.
[208] J.S. Machin, D.L. Hanna, Viscosity studies of system CaO–MgO–Al_2O_3–SiO_2: I, 40% SiO_2, J. Amer. Ceram. Soc. 28 (1945) 310–316.
[209] J.S. Machin, T.B. Yee, Viscosity studies of system CaO–MgO–Al_2O_3–SiO_2: II, CaO–Al_2O_3–SiO_2, J. Amer. Ceram. Soc. 31 (1948) 200–204.
[210] J.S. Machin, T.B. Yee, D.L. Hanna, Viscosity studies of system CaO–MgO–Al_2O_3–SiO_2: III, 35%, 45%, and 50% SiO_2, J. Amer. Ceram. Soc. 35 (1952) 322–325.
[211] J.S. Machin, T.B. Yee, Viscosity studies of system CaO–MgO–Al_2O_3–SiO_2: IV, 60% and 65% SiO_2, J. Amer. Ceram. Soc. 37 (1954) 177–185.
[212] Gul'tyai II, Effect of Al_2O_3 on the viscosity of slags of the system CaO–MgO–SiO_2, Izv. Akad. Nauk SSSR, Otd. Tekhn. Nauk, Metall. Toplivo 5 (1962) 52–65.
[213] M.J. Toplis, D.B. Dingwell, Shear viscosities of CaO–Al_2O_3–SiO_2 and MgO–Al_2O_3–SiO_2 liquids: implications for the structural role of aluminium and the degree of polymerisation of aluminosilicate melts, Geochim. Cosmochim. Acta 68 (2004) 5169–5188.
[214] G. Urbain, Y. Bottinga, P. Richet, Viscosity of liquid silica, silicates and alumosilicates, Geochim. Cosmochim. Acta 46 (1982) 1061–1072.
[215] M.J. Toplis, D.B. Dingwell, Peraluminous viscosity maxima in Na_2O–Al_2O_3–SiO_2 liquids: the role of triclusters in tectosilicate melts, Geochim. Cosmochim. Acta 61 (1997) 2605–2612.
[216] D.J. Stein, F.J. Spera, Experimental rheometry of melts and supercooled liquids in the system $NaAlSiO_4$–SiO_2: implications for structure and dynamics, Amer. Min. 78 (1993) 710–723.
[217] E.F. Riebling, Structure of sodium aluminosilicate melts containing at least 50 mole% SiO_2 at 1500°C, J. Chem. Phys. 44 (1966) 2857–2865.
[218] T. Tanaka, K. Hack, T. Iida, S. Hara, Application of thermodynamic databases to the evaluation of surface tensions of molten alloys, salt mixtures and oxide mixtures, Z. Met.kd. 87 (1996) 380–389.
[219] J.A.V. Butler, Thermodynamics of the surfaces of solutions, Proc. R. Soc. 135 (1932) 348–375.
[220] T. Tanaka, S. Hara, Application of thermodynamic databases to evaluation of interfacial tension between liquid steels and molten slags, Z. Met.kd. 90 (1999) 348–354.
[221] J.-Y. Choi, H.-G. Lee, Thermodynamic evaluation of the surface tension of molten CaO–SiO_2–Al_2O_3 ternary slag, ISIJ Inter. 42 (2002) 221–228.
[222] M. Nakamoto, A. Kiyose, T. Tanaka, L. Holappa, M. Hämäläinen, Evaluation of the surface tension of ternary silicate melts containing Al_2O_3, CaO, FeO, MgO or MnO, ISIJ Inter. 47 (2007) 38–43.
[223] K. Tang, J. Olsen, S. Johansen, Modeling of the surface/interfacial tension for the ladle refining of silicon metal process. Molten 2009, Santiago, Chile, pp. 715–725.